MAX PLANCK INSTITUTE
FOR HEART AND LUNG RESEARCH
W. G. KERCKHOFF INSTITUTE

Role of FoxO3 transcription factor in right ventricular remodeling and failure

Inaugural Dissertation submitted to the

Faculty of Medicine

In partial fulfillment of the requirements for the degree of

Doctor of Human Biology (**Dr. biol. hom.**)

of the Justus Liebig University Giessen

Germany

by

Sreenath Reddy Nayakanti

from *Kurnool, India*

Giessen, 2022

Faculty for Medicine, Justus Liebig University Giessen

From the Max-Planck-Institute for Heart and Lung Research

Department of Lung Development and Remodeling

Gutachterin: **Prof. Dr. Soni Savai Pullamsetti**

Gutachter: **Prof. Dr. Saverio Bellusci**

Disputation date: **27th September 2023**

TABLE OF CONTENTS

LIST OF FIGURES

LIST of TABLES

LIST OF ABBREVIATIONS

-/-	Homozygous knockout of the indicated gene
-/+	Heterozygous knockout of the indicated gene
+/+	Wildtype mice
ACTB	β-actin
aSMA	alpha Smooth Muscle Actin
BSA	Bovine Serum Albumin
CA9	Carbonic Anhydrase 9
CaM	Calmodulin
CFs	Cardiac Fibroblasts
CI	Cardiac Index
CO	Cardiac Output
cRV	compensated Right Ventricle
CSA	Cross-sectional area
Ctrl	Control
DAPI	4',6-Diamidino-2-Phenylindole
DBD	DNA-binding domain
dcRV	decompensated Right Ventricle
DEGs	Differentially Expressed Genes
ECM	Extracellular matrix
EDP	End-diastolic pressure
EDV	End-diastolic volume
EF	Ejection Fraction
ESP	End-systolic pressure
ESV	End-systolic volume
FB/fb	Fibroblast
FOXO	Forkhead Box O
GAPDH	Glyceraldehyde 3-Phosphate Dehydrogenase
GF	Growth Factor
GO	Gene Ontology
GSEA	Gene Set Enrichment Analysis
HCFs	Human Cardiac Fibroblasts
HIF1-α	Hypoxia Inducible Factor 1α
HOX	Hypoxia
HPRT1	Hypoxanthine Phosphoribosyl Transferase 1
hRV	healthy Right Ventricle
IB4	Isolectin B4

IPAH	Idiopathic Pulmonary Arterial Hypertension
KO	Knockout
LV	Left Ventricle
LVSP	Left ventricle systolic pressure
MCT	Monocrotaline
mPAP	mean pulmonary artery pressure
MRI	Magnetic Resonance Imaging
mRNA	messenger RNA
NOX	Normoxia
PAB	Pulmonary Artery Banding
PAH	Pulmonary Arterial Hypertension
PH	Pulmonary Hypertension
POSTN	Periostin
PTMs	Post-translational modifications
PVR	Pulmonary Vascular Resistance
RHC	Right Heart Catheterization
RHF	Right Heart Failure
RNA	Ribonucleic Acid
RT-PCR	Real-time Polymerase Chain Reaction
RV	Right Ventricle
RVH	RV Hypertrophy
RVSP	Right Ventricle Systolic Pressure
SEM	Standard Error of the Mean
Su/Hx	Sugen5416/Hypoxia
SV	Stroke Volume
SVI	Stroke Volume Index
TAC	Transverse Aortic Constriction
TFP	Trifluoperazine
TFs	Transcription Factors
WGA	Wheat Germ Agglutinin
WT	Wildtype
Col1a1	Collagen type 1 alpha 1
ANG II	Angiotensin 2
IVS	Interventricular septum
FDR	False Discovery Rate

1. INTRODUCTION

1.1 Pulmonary Circulation and right ventricle

1.1.1 Pulmonary Vasculature and physiology

The pulmonary vascular system is unusual for both its size and function. For gas exchange in the alveoli, mixed venous blood is delivered through the pulmonary circulation, a low-pressure circulatory bed capable of transporting the whole cardiac output. Alveolar capillaries, where blood flow swiftly equilibrates with alveolar air, are where gas exchange happens in normal circumstances. Blood cells travel through the capillary network at an average speed of 0.5–1 second. Due to the capillary bed's volume being normally equal to the stroke volume, each pulse exchanges the whole capillary volume. Since each pulse exchanges the entire volume of the capillary bed, each heartbeat is equivalent to a stroke.

The pulmonary vasculature is a one-of-a-kind structure in terms of volume and function. The pulmonary circulation is a low-flow, high-resistance circuit throughout fetal life. The pulmonary vasculature dilates throughout postnatal life, accommodating the whole cardiac output (CO) while maintaining a high blood flow at a low intravascular pulmonary arterial pressure (PAP). In comparison to the systemic circulation, pulmonary arteries have thinner walls with significantly less vascular smooth muscle and a relative lack of basal tone, most likely due to increased endogenous vasodilators and decreased endogenous vasoconstrictors, resulting in a normal pulmonary vascular resistance (PVR) of about one-tenth that of the systemic circulation. In addition, the adult lung's vascular anatomy, gravity, the mechanical consequences of breathing, and neuronal and humoral variables influence pulmonary blood flow (1).

In addition to exchanging gases, the lungs filter the blood, which helps to keep thrombi and other micro emboli from entering the bloodstream. Pulmonary circulation is also essential to metabolic activity since the whole circulating blood flow flows through the lungs. In humans, endothelium-bound angiotensin-converting is responsible for the alteration of angiotensin I to angiotensin II (ANG II) and the deactivation of bradykinin of regulating the blood pressure. As a blood reserve, it provides nutrients to the alveoli and temporarily supports the left ventricle's (LV) output when the right ventricle's (RV) production is limited (2).

1.1.2 Anatomy of Right Ventricle and physiology

In mammals and birds, the RV is a thin-walled crescent-shaped structure connected to systemic venous return on one side and pulmonary circulation on the other. It has a 10% to 15% larger volume than the left ventricle (LV), a thinner free wall (3 to 5 mm in adults), and a one-third to one-sixth smaller mass (3, 4). For example, during imaging, it is possible to

partition RV into the anterior and posterior walls and the basic to middle and apex portions (5). There are three major components of the RV anatomically, 1) Three or more papillary muscles, 2) the tricuspid valve that makes up the intake, and 3) The apical trabeculation, which may be pretty thin. The infundibulum holds the pulmonary valve's leaflets in place, a tubular muscular tissue. The dimension of the infundibulum does not depend on how big the RV is as a whole. It makes up about 20% of the RV's end-diastolic volume (EDV). It is called the supraventricular crest, or ventriculoinfundibular fold. It separates the RV's input (tricuspid) and output (pulmonary valve) parts. Two bands form when the crest gets shorter. The first band is called a "parietal band" on the RV free wall. The second band is called "septo marginal," on the inside of the tricuspid annulus or septum (6). When the septo marginal band is too big or does not work well, it looks like a Y-shaped muscular strap that can make the RV into two separate chambers (double-chambered RV) (7). A part of the septal band called the inferior limb attaches to the moderator band, where the anterior papillary muscle attaches to it. A peristalsis-like motion is produced by the RV contracting in a highly coordinated way, 20 to 50 ms former in the sinus and apex than in the conus. The conus might operate as a barrier adjacent to high systolic pressures being communicated to the pulmonary artery because of its delayed contractions, greater curvature, and most likely more significant tropic response. Because of its unusual shape and low-pressure levels, the outflow of the RV is more stable than systemic circulation, which means less assistance is required in rerouting the flow.

1.2 Pulmonary hypertension and Right ventricular failure

1.2.1 Pulmonary hypertension

Pulmonary hypertension (PH) is characterized by substantial remodeling of the pulmonary vasculature and a gradual increase in the pulmonary vascular load, resulting in RV hypertrophy. Currently, PH is characterized hemodynamically by a resting mean pulmonary arterial pressure (mPAP) greater than 20 mm Hg, as measured by catheterization of the right heart. An increase in pulmonary vascular resistance (PVR) further characterizes precapillary PH resulting from pulmonary vascular disease. Resistance of at least three Wood units (WU), as opposed to isolated post-capillary resistance PH with decreased PVR. 3 WU and the increase in mean pulmonary arterial pressure are attributable to increased filling pressures on the left side of the heart (8).

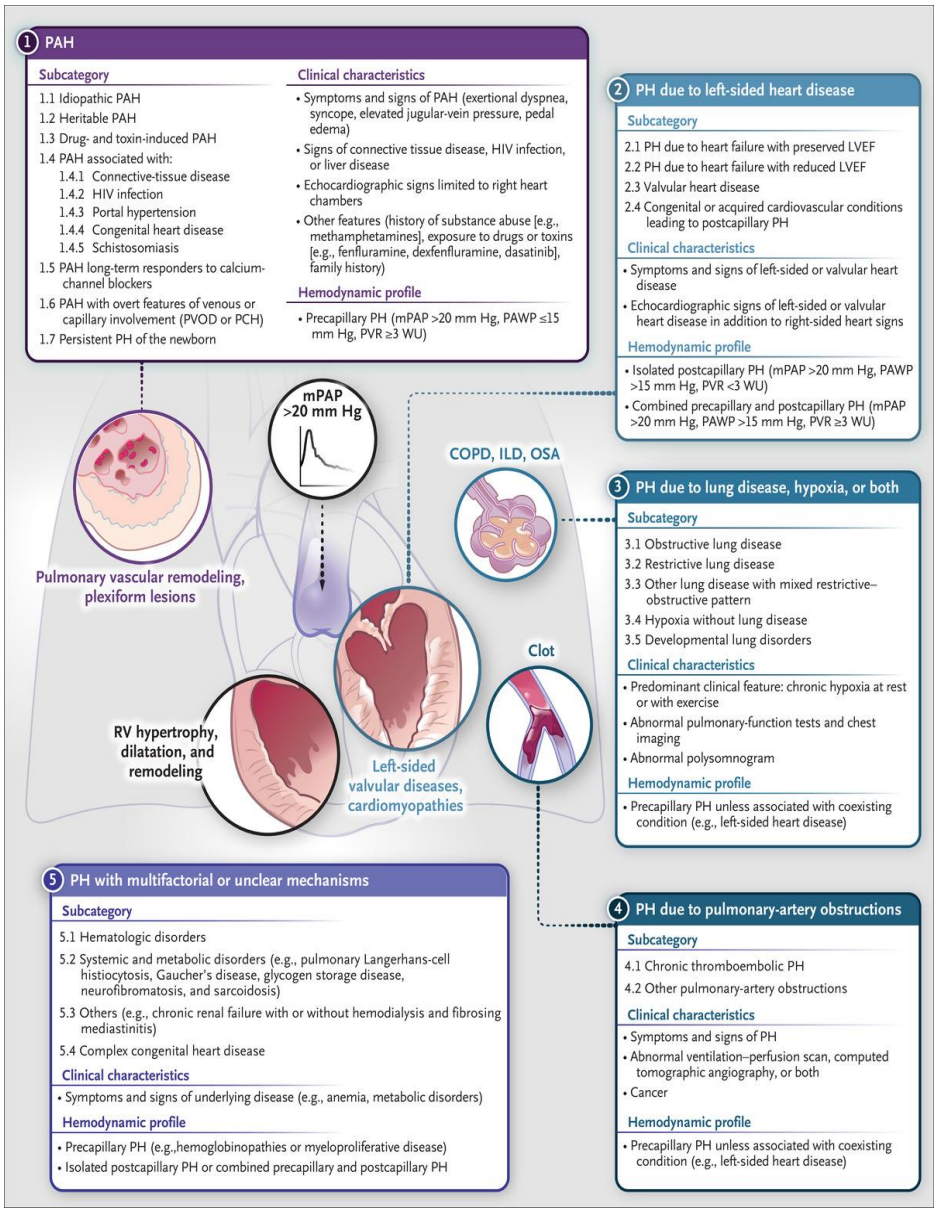

Figure 1. Clinical Classification of Pulmonary Hypertension (PH). The PH classification based on the 2018 World Symposium on Pulmonary Hypertension meeting is shown, along with each group's clinical characteristics and hemodynamic profile.1 COPD: chronic obstructive pulmonary disease, HIV: human immunodeficiency virus, ILD: interstitial lung disease, LVEF: left ventricular ejection fraction, mPAP mean pulmonary arterial pressure, OSA: obstructive sleep apnea, PAH: pulmonary arterial hypertension, PAWP: pulmonary arterial wedge pressure, PCH: pulmonary capillary hemangiomatosis, PVOD: pulmonary veno-occlusive disease, PVR: pulmonary vascular resistance, RV: right ventricular, and WU: Wood units *Reproduced with permission from (8), Copyright Massachusetts Medical Society.*

PH is classified into five groups based on different etiologies (**Figure 1**). The primary cause of mortality in people with PH is right heart malfunction, cardiac collapse, and respiratory failure. Exertional dyspnea, which indicates an inability to elevate cardiac output (CO), is prevalent in PH patients. Other symptoms mentioned include low energy or tiredness, hypotension, and angina pectoris, all indications of right heart failure (9). The predicted median survival period following diagnosis for patients is around 2.8 and 4 years.

1.2.2 Anatomical and Physiological differences between the RV and LV

The RV and LV have distinct developmental origins (10). The LV arises from the first heart field, whereas the RV originates from the second heart field. Consequently, it is highly likely that distinct gene sets control RV and LV formation. The RV functions as a systemic ventricle during gestation. In addition to providing little pulmonary blood flow throughout fetal life, the RV pumps blood to the inferior body and placenta and delivers more than half of the total CO (11). With the shift from fetal to postnatal physiology and the decrease in PVR, the sub pulmonary RV changes its shape and geometry, becoming a thin-walled chamber to acquire its postnatal physiologic features (12). Due to the low resistance nature of the pulmonary circulation, the normal postnatal RV preserves the same CO as the LV at a fraction of the energy expenditure. This contrast is reflected in the quadrilateral RV pressure-volume loop, which has few, if any, isovolumic intervals.

Consequently, RV output begins early during pressure formation and is later sustained by a "hangout phase" during which antegrade flow into the pulmonary artery persists despite the commencement of RV relaxation. On the contrary, the rectangular LV pressure-volume loops depict the LV square-wave pump function with well-defined contraction and relaxation intervals. Similarly, RV myocytes have quicker stroke speeds than LV (13). The anatomical distinctions between the ventricles correlate with the physiological variances (**Table 1**). The low-pressure RV is three-sided in the sagittal section and crescent-shaped cross-section due to the concave RV free wall and convex interventricular septum that wrap around the high-pressured, thick-walled, bullet-shaped LV. Consequently, although the standard RV has a lower ratio of volume to surface area and a thinner wall than the LV, the RV's ratio of volume to surface area and wall thickness are comparable (14), and the decreased cavity pressure results in reduced wall stress and oxygen requirements. The architecture of the myocardium also reveals anatomical distinctions. LV epicardial and endocardial fibers are oblique and helical, whereas the myocardial myocytes are oriented primarily in the short-axis plane (15). Consequently, the contraction of the LV is largely circumferential and radial, with a supplementary rotational and twisting motion. RV myocytes are mostly longitudinal, causing peristaltic contraction from inflow to outflow and bellows-like movement of the free wall toward the septum (16). Beyond that, the ventricles diverge in their anatomy and physiology is overwhelming, but these distinct features are also intimately linked to the pathophysiology and disease (17).

	Left ventricle	Right ventricle
Evolutionary development	Early	Late
Embryological origin	First heart field	Second heart field
Morphological characteristics	Bullet shape	Crescentic
Myocardial characteristics	Thick, fine trabeculated walls	Thin, heavily trabeculated walls
Myocardial architecture	Predominant radial myocyte orientation in the mid layers; endocardial myocytes follow right-hand helix configuration; epicardial myocytes form the left-hand helix	Predominant longitudinal myocyte orientation; the angulated intrusion of superficial myocytes toward the endocardium
Physiological pump conditions	High-resistance, high-pressure pump; dominant radial thickening and contraction during ejection	Low-resistance, low-capacitance pump; peristaltic-like motion from inflow to outflow during ejection
Flow characteristics	Well-defined isovolumic contraction and relaxation; no hangout period	No or minimal isovolumic periods; hangout period

Table 1. Differences between the right and left ventricles under normal conditions. (Modified table from reference (17)).

1.2.3 Pathophysiology of right heart remodeling and dysfunction

In patients with PH, RV function is a significant determinant of survival. RV remodeling is a response that occurs due to both intrinsic and extrinsic stimuli. RV remodeling is a complex reorganization of the myocardial micro- and macro-structure, established as a result of the myocardial accumulation of extracellular matrix (ECM) (myocardial fibrosis), capillary loss, inflammatory/immune cell infiltration and cardiomyocyte hypertrophy, in response to pressure

overload, which leads to detrimental alterations in the myocardial performance, ultimately resulting in right heart failure and premature death (18) (**Figure 2**). The mechanisms behind RV remodeling produced by pressure stress are complicated and incompletely understood. On the other hand, the molecular mechanisms identified to play a role in LV remodeling may not necessarily contribute to the RV remodeling due to structural and functional variations between the two chambers (19). Recent studies have shown that several pathological processes may contribute to the development and pathobiology of RV remodeling, including increased myocardial fibrosis (20), inflammation (21), impaired myocardial capillarization (22), dysregulated neurohormonal homeostasis (23), altered metabolism (24), mitochondrial dysfunction (25), and increased reactive oxygen species (ROS) production (26).

Although an acute rise in afterload is less tolerated in the RV than in the LV, in the setting of PH, RV afterload increases gradually over time, allowing the RV sufficient time to adjust (27, 28). RV wall thickening (RV hypertrophy), which develops in the early (adaptive) phase of RV remodeling, permits the production of tremendous pressure to counteract increasing afterload. RV hypertrophy primarily results from the increased synthesis of new sarcomeres and other contractile proteins, allowing RV cardiomyocytes to grow in length and diameter with the primary aim of enhancing cardiomyocyte contractility. Moreover, RV adaptation to pressure overload is associated with the development of myocardial fibrosis (20), which provides a framework for cardiomyocytes to relate their contractility to the increasing RV wall stress (29). Similarly, RV adaptation is related to an increase in myocardial capillary density in the pressure-overloaded RV to provide adequate food and oxygen delivery to the cardiomyocytes (22). As major components of RV remodeling, the development of myocardial fibrosis, cardiomyocyte hypertrophy, and changes in myocardial capillarization occur sequentially and involve intricate overlapping signaling pathways in the myocardial cells, including cardiomyocytes, fibroblasts, resident/infiltrated immune cells, and coronary artery endothelial cells, mediated by diverse growth factors, cytokines, and chemokines.

Initial RV structural modifications following progressive pressure overload induction aim to sustain RV operation against the growing RV afterload at the price of structural alterations (adaptive RV remodeling). Nonetheless, as the disease progresses, the RV loses its capacity to withstand persistent infection pressure overload due to inadequate/excessive myocardial fibrosis, impaired myocardial capillarization, and cardiomyocyte apoptosis (transition to maladaptive RV remodeling), resulting in right heart failure.

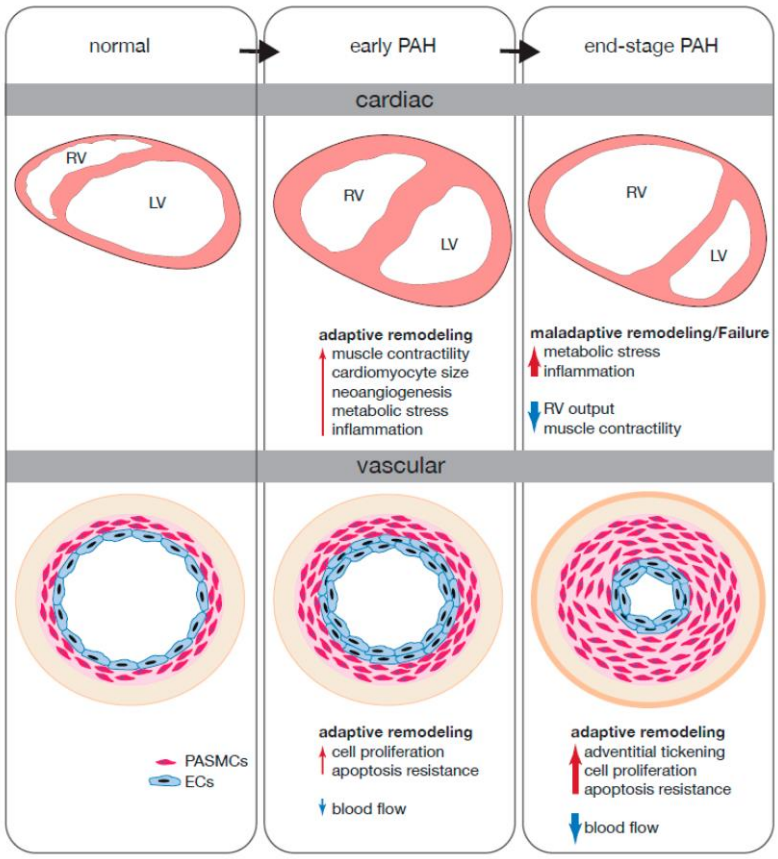

Figure 2. Pathophysiology of PAH-induced right heart failure. Reused under Creative Common CC BY license from reference (30).

1.3 Transcription factors

Transcription factors (TFs) are the first step in decoding the DNA sequence by directly interpreting the genome. Many acts as "master regulators" and "selector genes," directing mechanisms such as cell type specification and chronological sequencing (31) as well as specialized pathways like immunological responses (32). Compared to other sequences, TFs can have a thousand folds or more significant affinity for specific binding sequences (33). Since TFs can regulate transcription by blocking other proteins' DNA-binding sites (e.g., the classic lambda, lac, and trp repressors), the capacity to attach to a specific DNA sequence is frequently used as a criterion (34).

To activate TFs, various intracellular signaling pathways or specific molecules that bind, known as ligands, can be involved (35). Target genes' upstream, intron, or downstream regions contain cis-regulatory elements (CREs) to which TFs bind to modulate gene activity. Besides directly interacting with the core DNA sequence, they can also interact with distant genomic regions (36). Transcriptional activation CREs include promoters and enhancers, while transcriptional repression CREs are known as silencers (37). It is common for TFs to recognize their target sequences using a wide range of DNA-binding domains (DBD), including

homeodomain (HD), helix–turn–helix (HTH), and high-mobility group (HMG). Many other aspects are involved in TFs binding to DNA beyond the structural and sequence level. These include cofactors, epigenetic changes, and co-operation amongst other TFs (38).

Recognizing and binding to DNA sequences within regulatory regions that engage in transcriptional control are two critical aspects of TF activity (39). The present TF evolution literature covers a wide range of topics. To begin with, gene duplication and loss, key evolutionary factors (40), are also important drivers of TF evolution. They exist in all domains of life, regardless of organism complexity. By increasing or decreasing the number of TFs within specific binding regions, duplication and deletion of TFs can affect transcriptional regulatory networks (41). The two gene copies that come from the duplication of a TF gene are most frequently identical. They bind to the same target genes because they have the same sequence, including the DBD sequence. Alterations in the DBD sequence can cause one of the TF copies to regulate a different target gene due to the mutations.

1.3.1 Role of Transcription factors in PH and RV failure

Several TFs and transcriptional coactivators (proteins that do not contain DNA binding domain in their structure but can bind to other transcription factors to express or repress the ability of transcription factors to activate gene expression) have been associated with PH and RV dysfunction. Some of the key TFs include PPAR-γ, STAT3, myocyte enhancer factor 2 (MEF2), FOXO1, TP53, KLF4, HIF1A, HIF2A, CCAAT-enhancer binding proteins (CEBPs), Runt-related transcription factor 2 (RUNX2), FOSL1, FOSL2 CtBP1, FoxM1, PKM2, NF-κB, CTNNB1 (**Figure 3**) (42-48). FOXO1 inactivation is implicated in the pro-proliferative and apoptosis-resistant phenotype of pulmonary artery smooth muscle cells (PA-SMCs), and is a known downstream mediator of various growth factors and inflammatory signaling cascades (48). Likewise, the transcription factor FOXM1 belonging to the same forkhead family promotes PA-SMC proliferation in PH (42), suggesting that targeting the Forkhead box transcription factors could be a potential strategy for treating PH. Moreover, recent findings from our lab also delineated the role of FOSL transcription factors in driving RV dysfunction. Recently, TF co-activators have been implicated in the pathogenesis of PH (49, 50). Importantly, restoring metabolic activity using metabolic inhibitors like 2-deoxyglucose or directly lowering CtBP1 expression reduces adventitial fibroblast proliferation and apoptotic resistance (50).

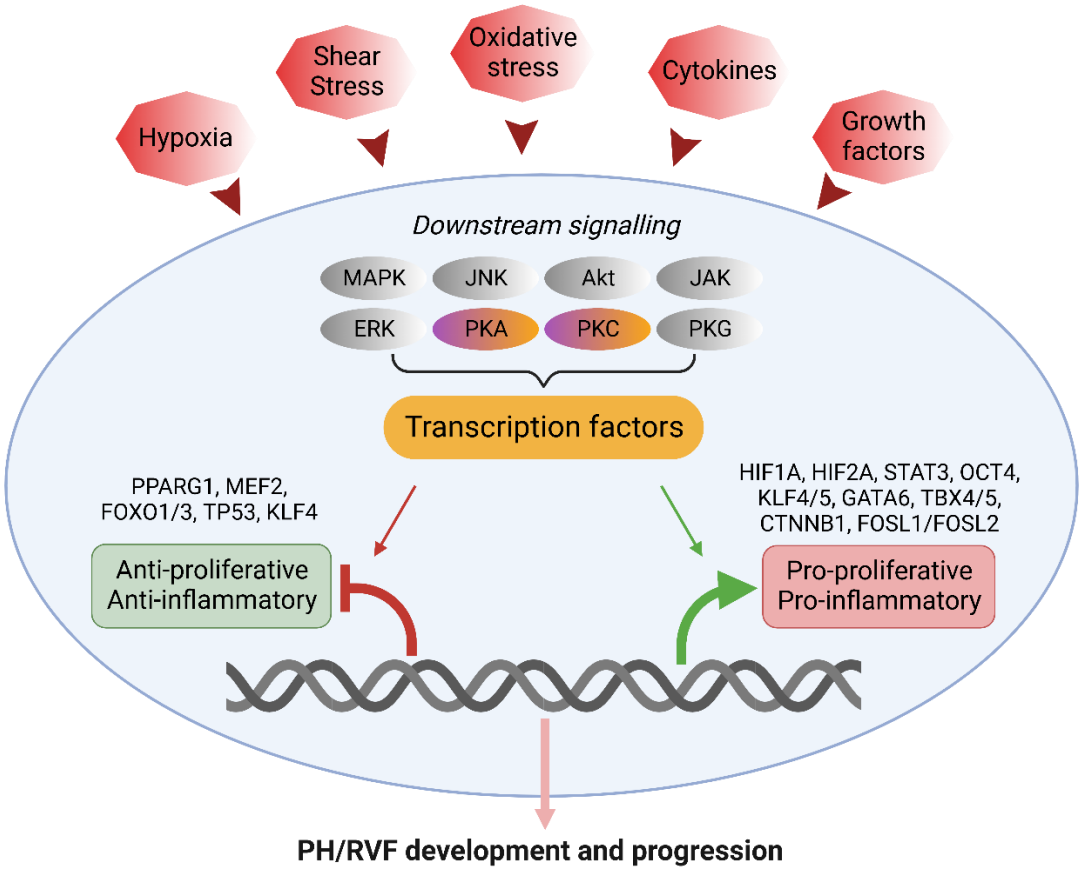

Figure 3. Transcription factors and transcriptional co-regulators in pulmonary hypertension (PH) pathogenesis induced RV failure. *"Created with BioRender.com."*

In PAH (Group 1 PH), phenotypic alterations in pulmonary vascular cells are caused by abnormalities in other TFs, such as NOTCH3, STAT3 and central mediator of HIPPO signaling, large tumor suppressor 1 (LATS1) (51), and in different growth factors. Loss of PPAR-ɣ in pulmonary endothelial cells, for instance, results in a defective complex formation with beta-catenin and a decrease in apelin impairs pulmonary endothelial cell survival and angiogenesis (52). Likewise, Yes-associated protein (YAP)/translational coactivator with PDZ-binding motif (TAZ) are emerging as essential regulators of cell growth and migration in PAH and associate mechanical stimulation with dysregulated vascular metabolism (53). A study in two rat strains, F344 and WKY, whose responses to chronic hypoxia differ, revealed that the gene Slc39a12 encoding the zinc transporter ZIP12 is an important additional regulator of hypoxia-induced pulmonary vascular remodeling (54). Although a more comprehensive knowledge of the overall risk-benefit ratio of targeting these TFs is still required, all these studies demonstrate the potential therapeutic value of targeting certain TFs and/or TF coactivators in PAH (55). Increasing evidence reveals that FOXOs are linked with several biological processes connected with the onset and progression of PH) and right ventricle failure (RVF).

1.4 The History of FOXOs

In the 1990s, chromosomal translocations detected in human cancers led to the discovery of FOXO genes (56). Furthermore, when insulin-like growth factor 1(IGF-1) triggered the PI3K/AKT pathway, DAF16, the nematode homolog of mammalian FOXO proteins, its function was reduced in Caenorhabditis worms and shown to be associated with longevity. All FOXO proteins in the mammalian FOXO family are phosphorylated at three specific AKT sites (Thr32, Ser253, and Ser315). It was discovered in 1999 that AKT had phosphorylated FOXO3a, leading to its nuclear accumulation (57). The studies of the FOXO1, 3a, and 4 full-body knock-out mice show that FOXOs play distinct and redundant roles. FOXO1 and FOXO3a, and FOXO4 deficiency led to a significant advance in our understanding of the function of FOXOs in oncology and regenerative cell biology. FOXO factors were long-established as tumor suppressors in these animals, and their involvement in stem cell compartment maintenance and integrity was shown (58).

In the vast Forkhead protein family, transcriptional controllers with a common DNA-binding area known as the "Forkhead box" includes FOXO transcription factors (59). Human FOXO genes encode proteins of similar length and predicted molecular mass of 54 to 72 kDa. FOXO proteins are composed of four domains: a 100-AA-residue forkhead DNA-binding domain (DBD), a nuclear localization signal (NLS) positioned downstream of the DNA-binding area, and a nuclear export sequences (NES) and a transactivation domain (TAD) at the N terminus **(Figure 4).** A member of the Forkhead group is found in every eukaryotic cell. Subgroups A to S of the Forkhead family (FOX stands for "Forkhead Box" A to S) have 39 members in humans. Organogenesis (FOXC) and language acquisition (FOXP) are two examples of FOX transcriptional regulators' involvement in a variety of developmental processes (60). Four members are in the Forkhead family subgroup FOXO (FOXO1, FOXO3, FOXO4, and FOXO6). FOXO1/FKHR, FOXO3/FKHRL1, and FOXO4/AFX were identified as genetic alterations in human tumors, and this led to the identification of the FOXO family in human beings in the first place (61).

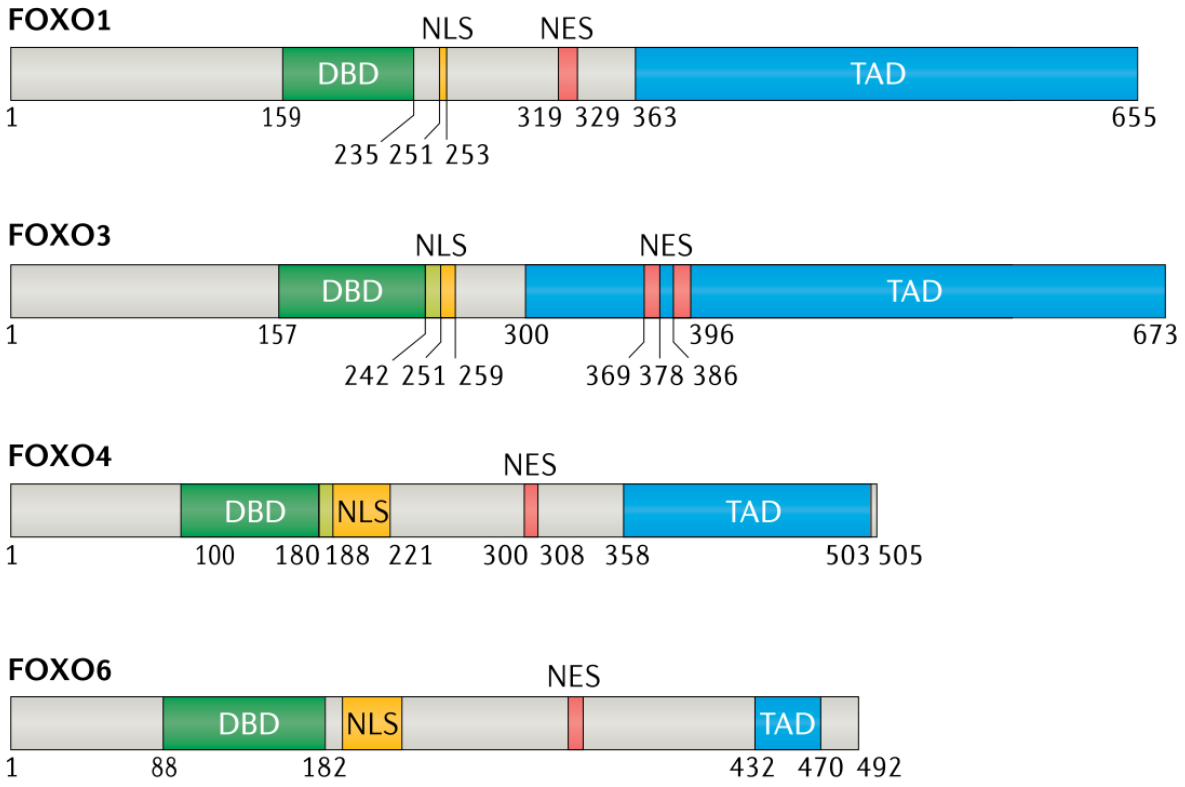

Figure 4. **The members of FOXO family transcription factors in humans**. FOXO1, FOXO3, FOXO4 and FOXO6. DBD: DNA binding domain, NLS: Nuclear localization signal, NES: Nuclear export signal, TAD: Transactivation domain. *Adapted with permission from Springer Nature, Calissi, G., et al. (2021). Nat Rev; Therapeutic strategies targeting FOXO transcription factors. License Number: 5307020874330* (62).

FOXO transcription factors may have a role in tumor growth, according to these preliminary findings. FOXO1 mRNA, FOXO3 mRNA, and FOXO4 mRNA are expressed in varying degrees in all organs in mammals (63). All three FOXO mRNAs in the brain and heart are found in fatty tissues, whereas only one of them, FOXO1 mRNA, may be found in the brain. This suggests that FOXO6 may play an important role in developing the nervous system (64).

1.4.1 Regulation of FOXO activity

The FOXOs are controlled by biosynthesis, phosphorylation, acetylation, and ubiquitination at three separate tiers: intracellular positioning, durability, and expression levels. Post-translational alterations of FOXO proteins form a molecular code that determines the transcriptional programs regulated by these transcriptional regulators (65) (**Figure 5**). FOXOs activity is regulated by growth factor-dependent stimulation of the PI3K/AKT pathways and oxidative signaling. In the lack of development or existence cues, FOXO proteins are present in the nucleus, where they may perform their transcriptional functions. FOXO transcription factors in the nucleus are phosphorylated by AKT in growth factors or cancerous cells when

the PI3K/AKT pathway is persistently stimulated, resulting in a binding domain for 14-3-3 protein which facilitates the transport of FOXO protein molecules to the cytoplasm and inhibits them. Regarding FOXO6 subcellular localization, PI3K/AKT signaling has little influence (64).

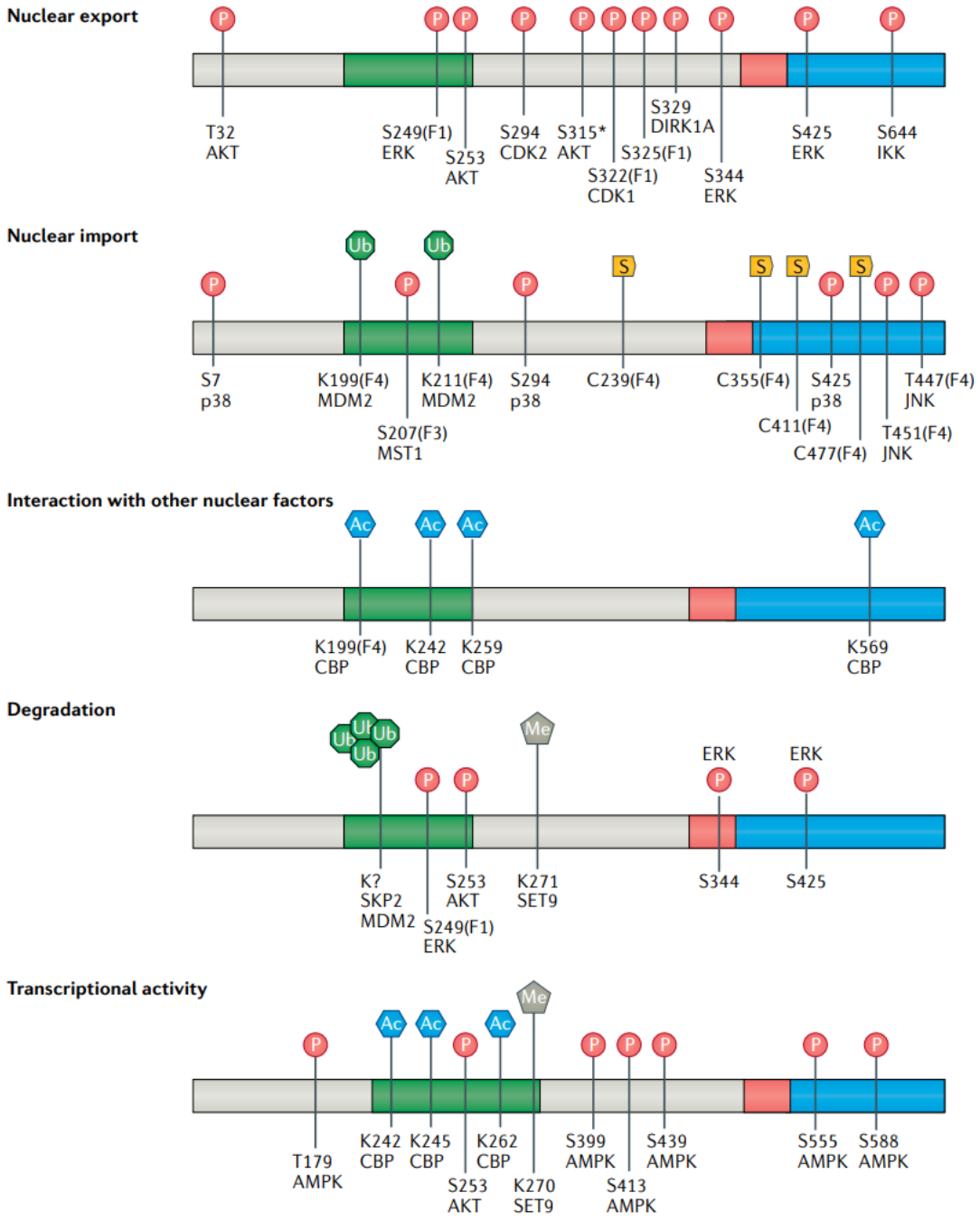

Figure 5. Outline of FOXO post-translational modifications. The major domains of FOXO and the modifications, including phosphorylation (P), ubiquitination (Ub), acetylation (Ac), formation of the intermolecular disulfide bonds (S), and methylation (Me), directly responsible for the listed effects are highlighted. Positions refer to FOXO3 if not stated otherwise (F1 for FOXO1, F4 for FOXO4, F6 for FOXO6). The asterisk indicates post-translational modifications not present in FOXO6. *Adapted with permission from Springer Nature, Calissi, G., et al. (2021). Nat Rev; Therapeutic strategies targeting FOXO transcription factors. License Number: 5307020874330* (62)

1.4.2 Phosphorylation of FOXO proteins

The kinase AKT phosphorylates FOXO proteins at three evolutionarily complementary sequences that are part of a pattern targeted by this kinase. Even though AKT phosphorylation is the most well-known FOXO-PTM, FOXO components are phosphorylated by a wide range of kinases (66). Both DNA binding affinity and 14-3-3 interaction can be reduced by AKT/SGK1 phosphorylation. Because S253 is concealed within the NLS of FOXO, phosphorylation of T32 and S253 makes it easier for 14-3-3 to connect with FOXO, which changes and may hide the NLS sequence (67). Because FOXO1 is excluded from the nucleus by IGFR1, at least one other mechanism must exist to shuttle the protein into the cytoplasm (68). It appears that Melted, another scaffold protein in Drosophila, is responsible for modulating the phosphorylation of AKT-phosphorylated drosophila FOXO (dFOXO), which in turn allows dFOXO and AKT to be near to each other under active insulin/IGF-1 signaling (IIS) (69). The ubiquitination of phosphorylated FOXO in the cytoplasm can lead to its proteasomal degradation (70). However, the phosphorylation of these proteins can induce the nuclear localization and activation of FOXO proteins. When Cdk1 is phosphorylated, it aids FOXO1-dependent transcription and induces apoptosis in the brain (71). dFOXO transcriptional activity was modulated by several kinases in Drosophila cell culture (72).

1.4.3 Acetylation, Ubiquitination and Methylation of FOXO proteins

In response to oxidative stress, FOXO proteins are acetylated by histone acetyltransferases (HATs), such as CBP and p300 (73, 74), and de-acetylated by histone deacetylases (HDACs), such as members of the sirtuin family of proteins (SIRT1, SIRT2, and SIRT3) (75). Target-specific acetylation of FOXO proteins boosts or lowers their transcriptional activity (75, 76). The majority of acetylation sites are in the DNA-binding domain (DBD) of FOXO proteins, and the acetylation of many lysine residues in FOXO1 and FOXO3 decreases their DNA-binding capacity (77). FOXO3 acetylation has also been demonstrated to enhance its transcriptional and tumor suppressive activities (78-80). Moreover, it has been demonstrated that acetylation of FOXO factors increases their susceptibility to phosphorylation and cytoplasmic localization (81). FOXO acetylation and deacetylation are thought to control FOXO activity, as opposed to operating as on/off switches like FOXO phosphorylation by kinases (62, 82).

In human primary tumors and cancer cell lines, activation of many protein kinases, including Akt, IB kinase (IKK), and ERK, results in phosphorylation of FOXO proteins and their ubiquitination mediated by E3 ligases such as SKP2 and MDM2. Due to their ubiquitination and proteasome degradation, the tumor suppressor activities of FOXO proteins are either decreased or eliminated, encouraging cell transformation, proliferation, and survival (83).

FOXO proteins are also well-known targets of methyltransferases, and Lysine methylation negatively regulates FOXO3-mediated transcription and neuronal apoptosis (84). Arginine methylation of FOXO transcription factors inhibits their phosphorylation by Akt (85). Notably, acetylation, ubiquitination, and methylation compete for the same lysine residues in FOXO proteins, and the effect of one PTM can influence another PTM; for instance, lysine residues in FOXO3 that are de-acetylated by SIRT1 can then be ubiquitylated, leading to FOXO3 degradation via the proteasomal system (86).

1.4.4 FOXO proteins and signaling pathway

FOXO1, 3, and 4 isoforms of the FOXO family exhibit overlapping and isoform-specific upstream regulatory systems and different target gene preferences (87). FOXO proteins are involved in various cellular physiological processes such as apoptosis, cell-cycle regulation, glucose metabolism, immune regulation, oxidative stress resistance, and longevity (**Figure 6**).

Numerous FOXO isoforms are being discovered to play non-redundant functions in various tissues. FOXO1, 3, and 4 are present in almost all tissues. FOXO6 expression is restricted to the CNS, and PI3K/AKT activation does not influence its subcellular localization. The prolonged activation of FOXO upregulates the synthesis of p27, p130, and cyclin G2 in the absence of growth factor-induced PI3K-Akt signaling, hence preserving the quiescent state. Stimulation of cells with growth factors and subsequent activation of the PI3K-Akt signaling pathway leads to the phosphorylation, nuclear exclusion, and inhibition of FOXO, as well as the reentry of cells into the cell cycle as a result of the loss of FOXO's effects on the expression of these target genes. FOXO is also involved in the cell cycle phase G2. In addition to inducing G1arrest, ectopic or conditional production of a constitutively active form of FOXO increases G2 delay or G2arrest. DNA microarray analysis suggests that GADD45a (growth arrest and DNA damage-inducible protein of 45 kDa) is a potential mediator of FOXO-induced G2 arrest. Purified recombinant GADD45a inhibits the histone H1 kinase activity associated with the cyclin B–Cdc2 complex by encouraging the complex's separation, which is important for G2 transition. FOXO directly binds and activates the GADD45a gene promoter, boosting the GADD45a protein level (88-90). Among the genes controlled by FOXO, GADD45a is triggered by a range of stressors, including ionizing radiation, ultraviolet light, and reactive oxygen species such as H_2O_2, indicating that FOXO may also be activated by cellular stress. DAF-16 translocates from the cytoplasm to the nucleus in C*. elegans* in response to specific forms of oxidative stress (91). FOXOs promote apoptosis in a mitochondria-independent and -dependent way by stimulating the production of death receptor ligands, such as Fas ligand, tumor necrosis factor-associated cell cycle arrest ligand, and Bcl-2 family members, including Bim, bNIP3, and Bcl-XL, respectively (57, 92). FOXO signaling is essential for physiological

muscle atrophy and is directly repressed by Hsp70 (93). Foxo1 loss led to a significant impairment in interleukin 7 receptor alpha-chain (IL-7R alpha) expression, correlated with its capacity to bind an Il7r enhancer. Furthermore, growth factor removal caused an elevation in Sell, Klf2, and Il7r expression in FOXO dependent manner (94). Considering the importance of insulin signaling on Akt-mediated phosphorylation of FOXO and the relatively hyper activation of FOXO signaling in insulin-responsive tissues, this transcription factor is very well known to modulate energy metabolism (95).

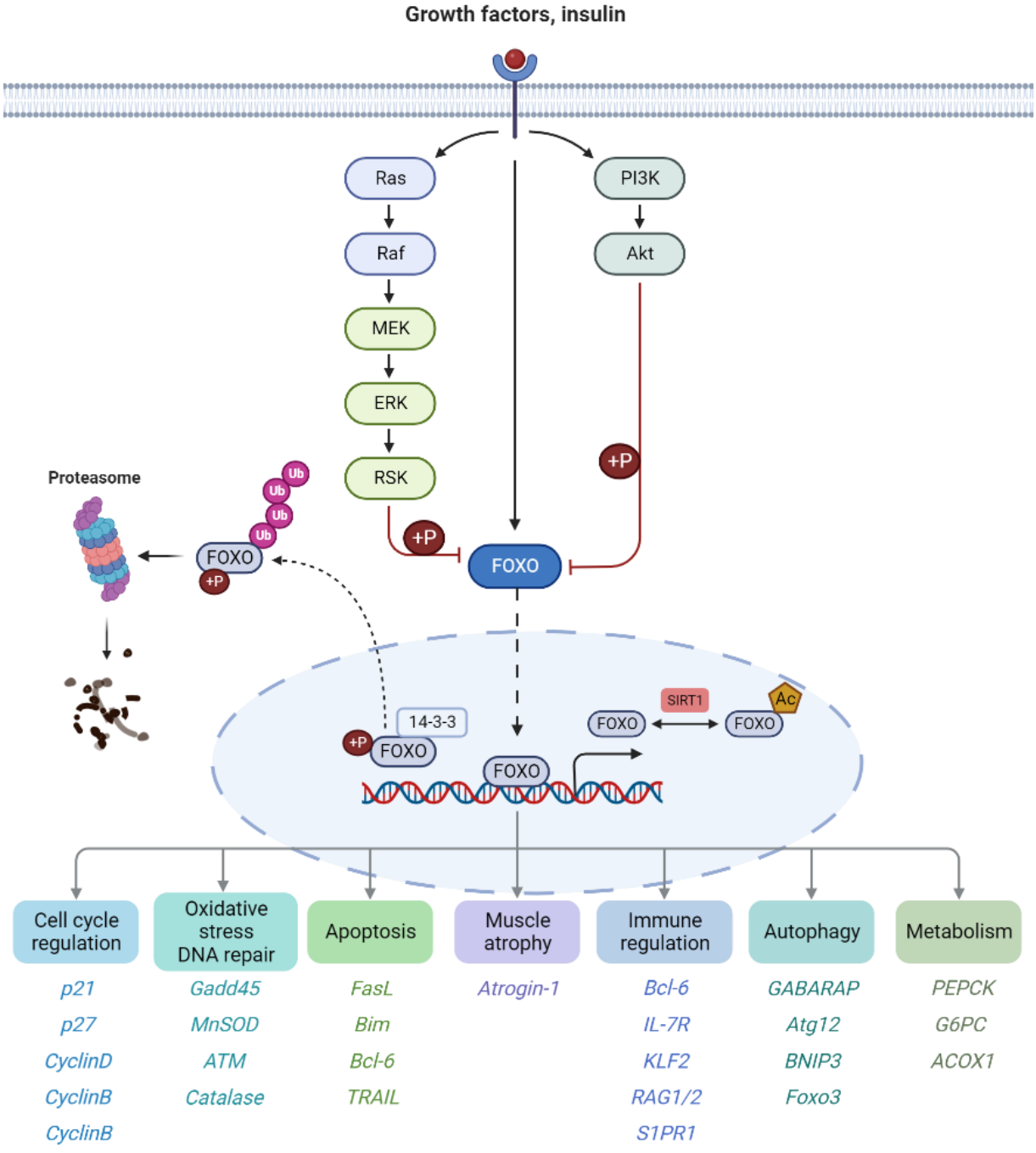

Figure 6. **FOXO signaling pathway and its downstream targets.** *"Created with BioRender.com."*

1.4.5 FOXO target genes

FOXOs are involved in a wide range of cellular processes, such as proliferation, cell death, autophagy, metabolic activity, infection, differentiation, and stress tolerance, according to a flood of studies published in the previous decade (**Table 2**). In many cases, the characterization of FOXO target genes coincided with or enabled the determination of the biological roles of these transcription factors, as mentioned above. The various cellular functions of FOXO factors and known FOXO target genes, which regulate these activities, are discussed below.

Target genes	FOXO	Pathway
BIM-1	FOXO3	Apoptosis
bNIP3	FOXO3	Muscle atrophy
Bcl-6	FOXO3, FOXO4	Apoptosis
FasL	FOXO1, FOXO3	Apoptosis
Trail	FOXO3	Apoptosis
atrogin-1	FOXO3	Muscle atrophy
G6Pase	FOXO1, FOXO3	Metabolism
PEPCK	FOXO1	Metabolism
p21CIP1	FOXO1, FOXO3, FOXO4	Cell cycle
p27KIP1	FOXO1, FOXO3, FOXO4	Cell cycle
p130	FOXO1, FOXO3, FOXO4	Cell cycle
GADD45	FOXO3, FOXO4	DNA repair
Cyclin G2	FOXO1, FOXO3, FOXO4	Cell cycle
GADD45	FOXO3, FOXO4	Cell cycle
DDB1	FOXO1	DNA repair
MnSOD	FOXO3	Stress resistance
catalase	FOXO3	Stress resistance
p21CIP1	FOXO3	Differentiation
BTG1	FOXO3	Differentiation

Table 2. FOXO target genes and their pathways. Modified from reference (96)**.**

1.5 FOXOs and human diseases

Due to their critical involvement in a wide range of cellular processes, FOXO proteins have been implicated in several human diseases, such as carcinoma, hyperglycemia, fertility problems, neurodegeneration, and immune response failure. According to recent research, the

deregulation of FOXO factors may also play a role in the link between insulin resistance, metabolic diseases, and cancer. Post-translational changes and miRNA-mediated inhibition inactivate FOXO proteins in various human malignancies (97). Many cancerous cells have an increased amount of reactive oxygen species (ROS), which activates FOXO factors and promotes stress tolerance in dormant cells while suppressing proliferation and causing death in growth factor-treated cells. When FOXO proteins are deactivated in cancerous cells, transcriptional pathways controlling cell development and defense systems are reduced. As an outcome, triple conditional knockout of FOXO1, 3, and 4 developed cancer in mice. FOXO proteins function as the last effectors in the insulin signaling cascade, promoting gluconeogenesis in the liver, inhibiting adipocyte and myocyte differentiation, and changing muscle fuel consumption from glucose to lipids in response to nutrient deficiency (98). As a result, diabetes has been linked to FOXO protein dysregulation.

1.5.1 Role of FOXOs in cancerogenesis

FOXO3, FOXO1, and FOXO4 are detected at chromosomal translocation breakdown sites in rhabdomyosarcoma and severe myeloid leukemia cells. FOXO3 is a part of the FOXO family linked to Invasive ductal carcinoma, epithelial cancer, glioblastoma, and leukemia. As an outcome, FOXO3 is being investigated as a possible therapy for several cancers. Akt, IKK, and ERK are three carcinogenic kinases that are commonly active in human malignancies, and all three kinases inhibit FOXO3a's tumor suppressor action in the same way (99). All three kinase-mediated phosphorylation increase FOXO3a ubiquitination, which leads to proteasomal degradation. As a result, researchers are working on a FOXO3a targeting technique based on controlling the kinases mentioned above. By blocking Akt activity, the chemotherapeutic drugs paclitaxel and KP372-1 (a multiple kinase inhibitor) used to treat breast cancer enhance FOXO3a (100). In K562 doxorubicin-sensitive leukemic cells, doxorubicin activates FOXO3a, which leads to the activation of the multidrug resistance gene ABCB1 (MDR1). Through suppression of BCR-ABL, imatinib activates FOXO3a and promotes Bim-dependent apoptosis in chronic myeloid leukemia. Imatinib also causes erythroid differentiation by activating FoxO3a and suppressing ID1 gene transcription (101). In T-cell acute lymphoblastic leukemia (T-ALL) cell lines, BMS-345541, a selective IKK inhibitor, increases apoptosis. FOXO3 targeting approaches may also help treat various types of human disorders, according to several publications from recent years. FoxO3a, for example, upregulates PUMA, which triggers apoptosis in prostate cancer cells. FoxO3a deficiency has been linked to chemotherapy resistance in liver cancer, and FoxO3a has anti-cancer characteristics in hepatocellular carcinoma (102). Through Akt, FoxO3a contributes to the neuroprotective action of erythropoietin (EPO) in Parkinson's disease. These results suggest

that as our understanding of FoxO3a targeting techniques improves, therapeutic use of FoxO3 may be a viable way to slow the course of cancerogenesis in the future.

1.5.2 Role of FoxOs in myocardial fibrosis

The three major cell types in cardiac tissue are cardiomyocytes, vascular endothelial cells, and fibroblasts. Fibroblasts comprise approximately 30% of the overall heart cell population. Fibroblasts are mesenchymal cells with a flat spindle structure that govern the extracellular matrix's equilibrium (103) (**Figure 7**). Collagen and elastic fibers are embedded in a viscous gel composed of glycosaminoglycan, hyaluronic acid, and other glycoproteins. These molecules interact via entangled, cross-linking, and charge-dependent connections to form bioactive polymers that partly influence tissues' biomechanical properties and biological phenotypes. The proportionate contributions of different ECM molecules vary according to tissue type, leading to mechanical and biological properties tailored to the environment. This study will address the role of specific profibrotic extracellular matrix in the cellular activities that result in tissue fibrosis. Any modification in the equilibrium of different ECM components alters the architecture of the tissue. Changes in structure typically affect the mechanical properties of tissues, which are then sensed by cells, resulting in altered cellular activity (104).

Because fibroblasts lack a specific cell marker, their identification is based on morphological, proliferative, and phenotypic properties. There is not yet a protein that is only found in fibroblasts. However, fibroblasts can be found in human and mouse heart tissues because of the expression of the elastin protein tyrosine kinase discoidin domain receptor 2 (DDR2) and intermediate filament-associated calcium-binding protein S100A4 (or fibroblast-specific protein 1 (105)). High voltage coupling, intercellular signaling, and tissue repair after damage are some of the most well-known roles of cardiac fibroblasts and other cells in the heart (106).

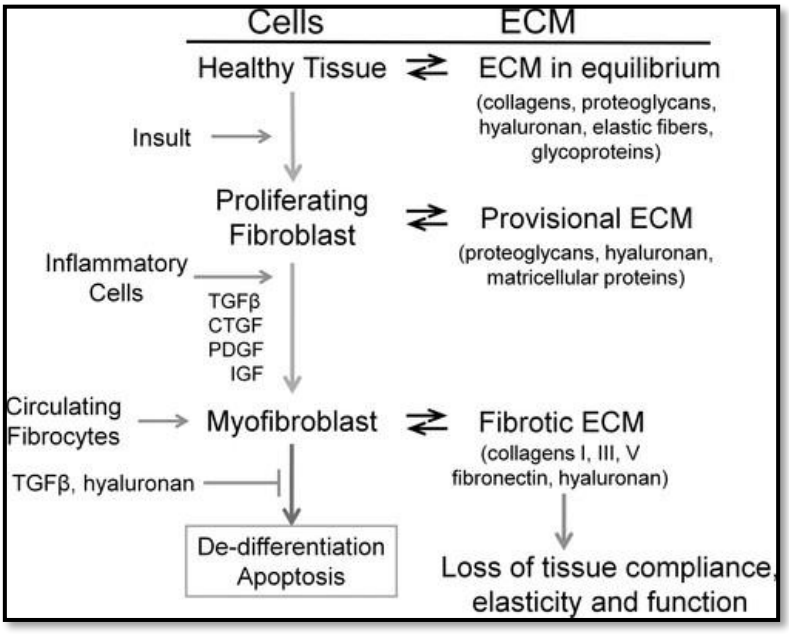

Figure 7. A postulated sequence of events illustrates a progressive remodeling of the ECM, which includes changes in the ECM's composition and impacts on cell phenotypic, finally leading to tissue fibrosis. Modified from reference (107).

FoxO3a controls cell cycle progression in adult rat cardiac fibroblasts by upregulating p27kip1, a cyclin-dependent kinase inhibitor, via an ERK1/2-dependent signaling mechanism. Increased collagen levels in the heart of diabetic mice are linked to reduced FoxO3 levels. Resveratrol also reduces the fibrosis caused by exercise by inactivating FoxO3. Exercise-induced fibrosis, on the other hand, is unrelated to FoxO3 phosphorylation in this paradigm. These findings point to FoxO3 inactivation as a factor in fibrosis reduction, most likely through regulation of proliferation and apoptosis sensitivity (108).

Collagen deposition and higher expression of aSMA are linked to FoxO3 inactivation in a unilateral ureteral obstruction-induced kidney fibrosis model. A distinguishing feature is the capacity of primary fibroblasts derived from patients with idiopathic pulmonary fibrosis (IPF) to avoid the proliferation-suppressive characteristics of polymerized type I collagen (109). This capacity is based on the abnormal stimulation of the PI3K/Akt signaling pathway, which inactivates FoxO3a and causes p27kip1 downregulation and reduced apoptosis sensitivity. FoxO3a is also suppressed by microRNA-96 in IPF fibroblasts. Caveolin 1 downregulation, which lowers Fas levels, causes decreased sensitivity to apoptosis. Reduced FoxO3 expression, on the other hand, is enough to cause IPF fibroblasts to become hyperproliferative (110). These data indicate that FoxO3 inhibition contributes to developing renal or pulmonary fibrosis by maintaining the proliferative pathogenic fibroblast phenotype. FoxO3 is also involved in the regulation of hepatic stellate cell proliferation and death in the liver. In the LX-2 cell line, immortalized human hepatic stellate cells, TRAIL, a member of the TNF family, promotes FoxO3 nuclear translocation and thereby increases apoptosis.

Furthermore, FoxO3 activation causes a rise in p27kip1 expression, which causes LX-2 proliferation to decrease (111). As a result, the evidence suggests that FoxO3 controls proliferation and apoptosis sensitivity rather than myofibroblast differentiation in hepatic stellate cells. FoxO3a siRNA can make human dermal fibroblasts more senescent when grown in the lab for the first time. Dermal fibroblasts exposed to UV light become more senescent in the same way that FoxO3 is phosphorylated. The senescent block phenotype caused by UV exposure is hampered when FoxO3 phosphorylation is inhibited. Activating p53 makes FoxO3a less active by phosphorylating it and moving it to different parts of the cell in a model of aging caused by Cell injury in mouse embryonic fibroblast cells.

1.5.3 Role of FOXOs in myocardial hypertrophy and dysfunction

Heart failure (HF) is a complicated clinical illness in which the heart cannot pump enough blood to support the body's basic metabolic requirements. It is a substantial public health issue that affects more than 23 million people globally, putting a strain on the healthcare system. HF remains one of the primary causes of disease and mortality, despite progress in evidence-based medicines and care quality. Between April 2013 and March 2014, the overall 1-year death rate in the UK was 27 percent, and the 5-year mortality rate was 45.5 percent, according to the National Institute for Cardiovascular Outcomes Research's national heart failure audit. We need to gain better knowledge of the molecular processes underlying the development and progression of heart failure in order to design viable treatment methods (112).

FOXO1, FOXO3, and FOXO4 are members of the FOXO subfamily that are expressed in the heart and localized in the nucleus, where they interact with coactivators and control multiple signals transduction pathways. The effects of the FOXO family on cardiac function and remodeling have been studied. The FOXO proteins are thought to be involved in oxidative stress, metabolic control, cell cycle, and cell death in the context of cardiac function.

FOXO1 - Cardiac hypertrophy

In the heart, FOXO1 is thought to serve an anti-hypertrophic function. Hypertrophy occurs in the heart due to mechanical strain, and hypertrophy can retreat when the heart is unloaded. FOXO1 activation was found responsible for left ventricular shrinkage after unloading in research by Hari Haran and colleagues. Furthermore, phosphorylation of FOXO1 inhibits left ventricular shrinkage during unloading (113).

The function of FOXO1 in diabetic cardiomyopathy is a highly debated topic. SY Chan et al. have reported that FOXO1 activation exacerbates metabolic abnormalities, causes cardiac cell death, and hinders angiogenesis, making it a critical pathogenic component in diabetic cardiomyopathy (114). On the contrary, some studies also show that metabolic stress-induced activation of FoxO1 triggers diabetic cardiomyopathy in mice (115). According to Y Qi et al., activation of Foxo1 by insulin resistance promotes cardiac dysfunction and β–Myosin heavy chain gene expression (116).

In ischemic heart disease, FOXO1 is a double-edged sword. Activation of FOXO1 causes endoplasmic reticulum (ER) stress and the stimulation of inducible NOS (iNOS) expression after ischemia. FOXO1 has also been demonstrated to boost the expression of antioxidants, therefore protecting the myocardium from ischemia damage.

FOXO3 – Cardiac hypertrophy

Myocardial hypertrophy has been demonstrated to be inhibited or reversed by FOXO3. On the other hand, its suppression causes pathological cardiac hypertrophy, heart failure, and mortality in mice (117). An increase in the size of individual cardiomyocytes characterizes the pathogenic alteration seen in cardiac hypertrophy. By limiting cardiomyocyte development and encouraging autophagy, FOXO3 preserves the size of cardiomyocytes. Under hyperglycemic circumstances, the activities of FOXO3 vary in various cardiac cell types. In diabetic rat cardiomyocytes, FOXO3 phosphorylation is reduced, whereas nuclear translocation is increased (118). As previously stated, FOXO1/3 plays a vital role in suppressing cardiac hypertrophy; nevertheless, FOXO1/3 activation is elevated under diabetes circumstances, and myocardial hypertrophy is the most common symptom of diabetic cardiomyopathy.

Ischemia-related cardiac damage is exacerbated by mitochondrial dysfunction. Myocardial infarction causes an overproduction of ROS in the mitochondria, aggravating mitochondrial dysfunction and ischemia damage. Through its intricately coordinated control, FOXO3 preserves healthy mitochondrial function and reduces ischemia damage. FOXO3 regulates cytoplasmic and mitochondrial calcium homeostasis by promoting the expression of the downstream protein ARC, which reduces calcium release from the sarcoplasmic reticulum and prevents oxidative stress-induced calcium elevations in cardiomyocytes' cytoplasm and mitochondria (119). As a result, FOXO3 knockout animals had larger myocardial infarct sizes after ischemia/reperfusion, suggesting that FOXO3 plays an important and beneficial function in calcium homeostasis following myocardial infarction.

FOXO4 – Cardiac hypertrophy

Endothelial NO is produced by up-regulation of endothelial NOS (eNOS), a critical enzyme in cardiovascular homeostasis. Endothelial NO reduces leukocyte attachment to the endothelium and migration into the vascular system by decreasing the synthesis of pro-inflammatory factors and a variety of membrane adhesion molecules (120). FOXO4 has been demonstrated to adhere to the regulator of arginase 1, a NOS inhibitor that increases arginase 1 expression while lowering NO production. FOXO4 silencing enhances NO production during ischemia while reducing neutrophil aggregation and cytokine activation, resulting in a reduced infarct and enhanced cardiac function following myocardial infarction.

1.5.4 FOXOs in pulmonary hypertension and RV dysfunction

In Pulmonary hypertension, FOXO1 has been shown as a critical integrator of pro-proliferative and proinflammatory signaling cascades. Savai et al. have nicely shown that FoxO and FoxO target genes are dysregulated in PAH vessels and targeted ablation of FoxO1 in SMCs resulted in exacerbated PH. Furthermore, they have convincingly shown that activation of FoxO1 using a genetic or pharmacological approach reverses established PH (48). Awad et al. reported hypoxia and ROS downregulate cellular antioxidant defenses and activate survival factors like Akt, which inactivated FoxO1 in PASMCs (121). In another study by Kudryashova et al., MST kinases promoted the proliferation of pulmonary artery adventitial fibroblasts (PAAF) and survival via PSMC6-dependent inhibition of FOXO3 (122). Inflammation is becoming increasingly prevalent in patients with pulmonary arterial hypertension. The inflammatory milieu in PAH is composed of indigenous and recruited phagocytic cells, dendrite, T cells, B cells, and mastocyte cells. FOXO1 is abundant in the immune system and serves a critical function in keeping T cells quiet and the body more receptive (123). FOXO1 is localized to the nucleus of dormant T lymphocytes. When triggered, the T-cell receptor migrates to the cytosol. FOXO1 deficiency can result in spontaneous T cell activation, B cell proliferation, and the generation of auto antibodies. Consequently, inhibiting FOXO1 consistently stimulates the immune cells involved in PAH. On the other hand, stimulating FOXO1 may aid in regulating inflammatory processes by decreasing both T- and B-cell function (124).

FOXO1 promotes macrophage activation in mature macrophages by increasing interleukin-1 and toll-like receptor 4 signaling. Thus, stimulation of FOXO1 may promote macrophage activation in the pulmonary circulation, favoring PAH. Paclitaxel, for example, enhances the expression of several circulating inflammatory mediators in vitro and in vivo, indicating that paclitaxel stimulates FoxO1 nuclear persistence in macrophages, at least in cancer patients (125). Although FoxO1 integrates receiving inflammatory signals in PASMCs, the result in PAH is variable, with some aspects helpful and others deleterious. Although tailored administration of such medicines (e.g., inhaled approach) may minimize some harmful effects on circulating cells, the impact on immune cells within and around the pulmonary arteries will continue to be a concern.

FOXO1 is inactivated in cardiomyocytes under hypertrophic stimuli. Overexpression of FOXO1 suppresses cardiac development in part by inhibiting the calcineurin/NFATc2 pathway (126). NFATc2 suppresses mitochondrial-dependent apoptosis in PAH by decreasing the transcription of several mitochondrial proteins and promoting the expression of an antiproliferative member of the BCL2 (B-cell CLL/lymphoma 2) family. In PAH rats' hypertrophied RV cardiomyocytes, phospho-FOXO1 (Thr24) is suppressed, resulting in a rise

in pyruvate dehydrogenase kinase 4 activity and eventual mitochondrial repression via pyruvate dehydrogenase inhibitory activity (127). This could be in contrast to the information that in RV hypertrophy, Akt and NFATc2 are active. This apparent disagreement could be since the RVs evaluated in these papers were not always classified as compensating or decompensating (128). FOXO1 could have contradictory effects on RV hypertrophy and, for example, play a role in the transformation from balanced to decompensated RV function. The impact of FOXO1-activating therapies on RV cardiomyocyte metabolism, hypertrophy, and failure must be examined (129).

FOXO1 stimulates the production of antioxidant genes, such as MnSOD, that are epigenetically reduced in pulmonary arterial hypertension. Additionally, FOXO1 regulates insulin's influence on the peroxisome proliferator-activated receptors gamma, coactivator 1 (PGC-1) promoter activity. PGC-1 enhances mitochondrial biogenesis and function in part by inducing the mitochondrial deacetylase sirtuin 3, which activates several mitochondrial enzymes. PGC-1 and SIRT3 are downregulated in PAH, implying that medications that activate FOXO1 may increase their synthesis (130).

Most of the studies focused on understanding the role of FoxOs in cardiac remodeling in the view of LV, and little is known about their role in the context of isolated RV dysfunction. Moreover, several studies primarily described the role of the FoxO1 isoform but did not address the role of the FoxO3 isoform in RV dysfunction. In the current thesis work, we would like to shed some light on the functional role of the FoxO3 transcription factor and associated signaling pathways in RV failure induced by chronic pressure overload.

2. AIMS OF THE STUDY

The functional state of the right ventricle (RV) is the primary determinant of prognosis in patients with pulmonary hypertension (PH). RV hypertrophy (RVH) triggered by pressure overload is initially compensatory but often leads to RV failure. The Forkhead family of transcription factors plays an essential role in cell signaling mechanisms that mediates various physiological and molecular aspects of RV function, including cell cycle regulation, metabolism, ECM organization and muscle atrophy. Although there is substantial evidence about the effects of FoxO3 in cultured cardiac cells, thus far, the elucidation of fibroblast-specific FoxO3 function on the RV function is still mostly unknown. However, insights of relevance for RV compensation and decompensation can likely be gained under these conditions.

The work presented in this thesis aims to elucidate the role of the FoxO3 transcription factor in RV remodeling and failure. Specifically, we aimed to:

1. Determine the regulation of FoxOs during compensation and decompensation states of RV
2. Investigate the role of FoxO3 corresponding to RV function in pressure overload induced animal models
3. Investigate if FoxO3 is dysregulated in various pathophysiological processes involved in maladaptive remodeling of RV
4. Decipher the FoxO3-dependent transcriptomic changes upon pressure overload in mice
5. Understand the functional outcomes of pharmacological modulation of FoxO signaling in pathological states of RV in the context of PAH.

3. MATERIALS AND METHODS

3.1 Materials

3.1.1 Chemicals and Reagents

Reagent	Company
4′,6-Diamidin-2-phenylindol (DAPI)	Invitrogen, USA
Acetic acid, glacial	Sigma, USA
Acetone	Carl Roth, Germany
Acrylamide solution (30%)	Sigma Aldrich, USA
Agarose, low gelling temperature, Type VII	Sigma Aldrich, USA
Ammonium Persulfate (APS)	Sigma Aldrich, USA
Bovine serum albumin (BSA)	Carl Roth, Germany
Bromophenol blue	Roche, Germany
BSA solution (2mg/ml)	BioRad, USA
Chloroform	Carl Roth, Germany
Citrate buffer	Life technologies, USA
Dako Fluorescence Mounting Media	Dako, Denmark
Dimethyl sulfoxide	Sigma Aldrich, USA
Diphenylacetohydroxamic acid	Sigma Aldrich, USA
DirectPCR® lysis reagent	Peqlab, Germany
Di-sodium hydrogen phosphate	Carl Roth, Germany
DNA ladder	Fermentas, USA
Ethanol absolute	Carl Roth, Germany
Ethidium Bromide	Carl Roth, Germany
Ethylenediamine-Tetraceticacid (EDTA)	Carl Roth, Germany
Ferric-hematoxylin A	Waldeck, Germany
Ferric-hematoxylin B	Waldeck, Germany
Fluorescence mounting medium	Dako, USA
Halt™ protease and phosphatase inhibitor cocktail	Thermo Fisher Scientific, USA
Hanks' Balanced Salt solution	Thermo Fisher Scientific, USA
Hematoxylin Solution	Life technologies, USA
Hydrochloric acid	Carl Roth, Germany
Hydrogen peroxide	Merck, Germany
Isopropanol	Carl Roth, Germany

iTaq™ Universal SYBR® Green Supermix	BioRad, USA
Mayer's Hematoxylin Solution	Sigma Aldrich, USA
Methanol	Carl Roth, Germany
Methyl-green	Vector, USA
Milk powder	Carl Roth, Germany
N,N,N´,N´-Tetramethyl-1,2-diaminomethane (TEMED)	Sigma Aldrich, USA
Page Ruler Prestained Protein Ladder	Thermo Scientific, USA
Paraformaldehyde	Carl Roth, Germany
Pertex Mounting Medium	Medite, Germany
Picric acid	AppliChem, Germany
Ponceau S Solution	Sigma Aldrich, USA
Potassium chloride	Carl Roth, Germany
Potassium dihydrogen phosphate	Carl Roth, Germany
Proteinase K	Peqlab, Germany
Proteinase K 40x	Dako, Denmark
Proteinase K Diluent	Dako, Denmark
Rainbow protein molecular weight marker	AmershamBiosciences, USA
RNase Away	Invitrogen, USA
Scott's Tap Water Substitute Concentrate 10X	Sigma Aldrich, USA
Sodium bicarbonate	Carl Roth, Germany
Sodium chloride	Carl Roth, Germany
Sodium dodecylsulfate (20% w/v)	Carl Roth, Germany
Sodium hydroxide	Carl Roth, Germany
Stripping Buffer	Thermo Scientific, USA
Tetramethylrhodamine methyl ester (TMRM)	Invitrogen, USA
Tris 0.5 M (pH 6.8)	Amresco, Germany
Tris 1.5M (pH 8.9)	Amresco, Germany
Tris base	Sigma Aldrich, USA
Triton X-100	Carl Roth, Germany
TRIzol™	Thermo Fisher Scientific, USA
Trypsin Concentrate and Diluent	Life technologies, USA
Tween 20	Sigma, USA
Xylol	Carl Roth, Germany
β mercaptoethanol	Sigma Aldrich, USA

3.1.2 List of Equipment used

Name of the Equipment	Company
Agarose electrophoresis chambers	BioRad, USA
Cell culture incubator, Hera cell	Heraus, Germany
Centrifuge	Thermo Scientific, USA
StepOnePlus™ Real-Time PCR System	Thermo Scientific, USA
Whitley H35 Hypoxystation	Don Whitley Scientific Ltd, UK
All-in-One Fluorescence Microscope (BZ-X series)	Keyence Corporation, USA
Fluorescence microscope Leica DM 2500	Leica, Germany
ImageQuant LAS 4000	GE Healthcare, UK
Leica DM 6000B	Leica, Germany
Microplate reader Infinite 200	TECAN, Germany
NanoDrop2000 Spectrophotometer	Thermo Scientific, USA
PCR thermocycler T3000	Biometra, Germany
Power supply	BioRad, USA
PowerLab	AD Instruments, Australia
Precellys Homogenizer	PeQLab, Germany
Nanozoomer 2.0 HT	Hamamatsu, Japan
Leica VT1200 S	Leica, Germany
Water bath (cell culture)	Heraeus, Germany
Western blot chambers	BioRad, USA
Cryostar NX50	Thermo Scientific, USA
Leica RM2255 Rotary Microtome	Leica, Germany
Leica EG1160 Tissue Embedding Station	Leica, Germany
ASP200S Advanced Smart VacuumTissue Processor	Leica, Germany
VisualSonics VEVO 1100	FujiFilm, Canada
MPVS Ultra Pressure-Volume Unit from Millar	AD Instruments, New Zealand
7.05 T Bruker PharmaScan MRI Imaging	Bruker, USA
Q Exactive Orbitrap Mass Spectrometer	Thermo Scientific, USA

3.1.3 List of Kits used

Name of the Kit	Company
DC Protein assay kit	BioRad, USA
High Capacity cDNA synthesis kit	Applied Biosystems, USA
Picro-Sirius red Stain kit	Abcam, UK
RNeasy Micro kit	Qiagen, USA
RNeasy Plus Micro kit	Qiagen, USA
Supersignal West Femto maximum sensitivity substrate kit	Thermo Scientific, USA

3.1.4 List of Primary Antibodies

Antibody	Host	Cross-reactivity	Company	Reference
FOXO3	Rabbit	HMR	Cell signaling	12829S
FOXO3	Rabbit	HMR	Novus	NBP2-16521
FOXO1	Rabbit	HMR	Cell signaling	2880S
TBP	Rabbit	HMR	cell signaling	44089S
pFOXO3 (S253)	Rabbit	HMR	Cell signaling	9466S
pFOXO1 (T24)/FOXO3(T32)	Rabbit	HMR	Cell signaling	9464S
CA9	Rabbit	HMR	Novus	NB100-417
pFOXO1 (s256)	Rabbit	HMR	Cell signaling	84192S
CTGF	Mouse	HMR	Santa Cruz	sc365970
Periostin	Mouse	HMR	Santa Cruz	sc398631
alpha SMA	Rabbit	H	Sigma	SAB5500002
GAPDH	Mouse	H	Invitrogen	MA5-15738
Beta-actin	Mouse	H	Sigma	A2228
Anti Vimentin-Cy3	Mouse	H	Sigma	C9080

3.1.5 List of Secondary Antibodies

Antibody	Host	Cross-reactivity	Company	Reference
Anti-Mouse IgG-Peroxidase conjugated	Rabbit	HM	Sigma	A9044

Anti-Rabbit IgG-Peroxidase conjugated	Goat	HM	Sigma	A0545
anti-Rabbit IgG, Alexa Fluor™ 488	Goat	HMR	Invitrogen	A-11008
anti-Rabbit IgG Alexa Fluor™ 594	Goat	HMR	Invitrogen	A-11037

3.1.6 List of Lectins used

Type of Lectin	Cross-reactivity	Company	Reference
Wheat Germ Agglutinin, Alexa Fluor™ 488 Conjugate	Plasma Membrane Labeling across species	Invitrogen	A-11037
Isolectin GS-IB4 From Griffonia simplicifolia, Alexa Fluor™ 594 Conjugate	Plasma Membrane Labeling across species	Invitrogen	I21413

3.1.7 List of Primers used for real-time PCR

Gene	Forward Primer	Reverse Primer
Hu FOXO1	ACGAGTGGATGGTCAAGAGC	TCTTGCCACCCTCTGGATTG
Hu FOXO3	TGTTGGTTTGAACGTGGGGA	TGTCCACTTGCTGAGAGCAG
Hu CCND1	TGACCCCGCACGATTTCATT	CATGGAGGGCGGATTGGAAA
Hu POSTN	TGATGGAGTGCCTGTGGAAA	CTTCCTCACGGGTGTGTCTC
Hu CTGF	GGTGTGGCTTTAGGAGCAGT	TGATGGCTGGAGAATGCACA
Hu COL3A1	TGGGAGAAATGGTGACCCTGG	CCAGGATAGCCTGCGAGTCCT
Hu TGFB1	GCAGCACGTGGAGCTGTA	CAGCCGGTTGCTGAGGTA
Hu TGFBR2	ATGACATCTCGCTGTAATGC	GGATGCCCTGGTGGTTGA
Hu ACTA1	ATGTGCGACGAAGACGAGAC	CAGTTGGTGATGATGCCGTG
Hu ACTA2	TGAGCTTCGTGTTGCCCCTG	CTCCCACAGGCCTCACCAGTA
Hu GAPDH	TTTTGCGTCGCCAGCCGAG	TGACCAGGCGCCCAATACGA
Hu HPRT1	TGACACTGGCAAAACAATGCA	GGTCCTTTTCACCAGCAAGCT
Hu PBGD	CAGGAGTCAGACTGTAGGACGAC	ACTCTCATCTTTGGGCTGTTTTC
Ms Hprt1	GCTGACCTGCTGGATTACAT	TTGGGGCTGTACTGCTTAAC

Ms Pbgd	AGAAGAGCCTGTTTACCAAGGAG	TTTCTCTGTAGCTGAGCCACTCT
Ms Foxo1	AGTGGATGGTGAAGAGCGTG	GAAGGGACAGATTGTGGCGA
Ms Foxo3	GAGGAAAGGGGAAATGGGCA	ACTGTCCACTTGCTGAGAGC
Rat Hprt1	GACTTTGCTTTCCTTGGTCA	AGTCAAGGGCATATCCAACA
Rat Pbgd	ATGTCCGGTAACGGCGGC	CAAGGTTTTCAGCATCGCTAC
Rat Foxo1	ACGAGTGGATGGTGAAGAGTG	CCTCCCTCTGGATTGAGCATC
Rat Foxo3	AAAGGGGAAATGGGCAAAGC	GGCTGAGAGCAGATTTGGCA

3.1.8 Equipment required for PAB surgery

Company	**Article Number**	**Article name**
FST	11050-10	Graefe Forceps - 0.8mm Tips Straight
FST	11052-10	Graefe Forceps - 0.8mm Tips Curved
FST	11009-13	Semken Forceps: curved, tipps serrated 1.3mmx1mm
FST	11370-31	Moria MC31 Forceps - Serrated Curved
FST	14106-09	Fine Iris Scissors - Large Loops Straight Sharp 9.5cm
FST	12060-01	Castroviejo Micro Needle Holder -Straight w/Lock 9cm
FST	15003-08	Vannas-Tübingen spring scissors, Effective Cutting Edge: 5mm
FST	15024-10	Spring Scissors - 8mm Blades Straight Sharp, **Länge: 10cm, Durchmesser der Spitzen: 0.2mm**
Edward Weck	REF 523735	Weck Hemoclip® small ligating clips
Edward Weck	523140 S	Weck Hemoclip® clip applier small

Handmade tools

Intubation cannula
Retractor consisting of 3 needles (20G)
L-shape needle G26

Devices required for PAB surgery

Company	Article Number	Article name
Leica	Leica M50 with small boom stand	Microscope for surgery, catheterization. Objective should have x0.5 (NOT x1.0)
Schott	KL-200	Cold light source
Hugo Sachs Electronics	73-0044	MiniVent Type 845
VetEquip	901806	Table Top Laboratory Animal Anesthesia System
AD Instruments	ML295/M-220	The ML295/M Homeothermic Controller and Plate provides temperature feedback control for controlling small animal (mouse) temperature through a heating plate. Heating Plate Size: 111 mm x 217 mm. The system includes the controller, heating plate and MLT1404 Mouse Rectal Probe.
Harvard Apparatus	720127	Germinator 500 Glass Bead Sterilizer (CellPoint Scientific)

Surgical sutures

Company	Article Number	Article name
Ethicon	EH7228	Ethicon Prolene 6-0 USP, C1 (13 mm 3/8c)

Analgesic buprenorphine hydrochloride (Temgesic®, 0.1 mg/kg, Sigma-Aldrich, Germany)

Braunoderm® (Braun, Melsungen, Germany)

3.2 METHODS

3.2.1 Human Tissue samples

Donor RVs (CTRL) tissues were obtained from patients with normal RV function who underwent cardiac surgery or early autopsy patients who did not have any cardiac or respiratory diseases. Idiopathic PAH (IPAH) RVs were obtained from an early autopsy of patients with end-stage PAH. Experimental procedures using human tissues obeyed the principles summarised in the Declaration of Helsinki and were performed with the approval of animal authorities at the Laval University and the IUCPQ Biosafety and Ethics Committees (CER#20773, CER#20735 and CER#21747). All the experiments were performed in accordance with the most recent preclinical PAH research guidelines. Clinical characteristics are described in (Table.1)(131).

3.2.2 Animals

Mice with the null (-) and floxed allele (L) for *Foxo3* were kindly provided by Prof. Ronald A. Depinho (Harvard Medical School, Boston, USA). To specifically delete Foxo3 in fibroblasts (Fb-Foxo3$^{-/-}$), homozygous floxed mice for the *Foxo3* allele (*Foxo3 L/L*) were crossed with transgenic mice expressing Cre under the control of collagen type 1A1 promoter (Col1a1-Cre). Fb-Foxo3$^{+/-}$ mice were intercrossed, and animals homozygous for Foxo3 deletion in fibroblasts (Fb-Foxo3$^{-/-}$) were obtained. Mice littermates were used as WT control. Col1a1-Cre transgenic mice were purchased from Mutant Mouse Regional Resource Centers (MMRRC; stock ID: 000208-UCD)(132).

Mice were given free access to water and food and housed under a controlled temperature (22°C) and standard light-dark cycle (12 hrs. each) throughout the experimental period. The experiments were performed as per NIH, USA Guidelines on the Use of Laboratory Animals. German federal authorities for animal research of the Regierungspräsidium Darmstadt (Hessen, Germany) approved the study protocol (approval numbers B2/1215).

3.2.3 Experimental groups

In total, 40 mice were included in the study; 20 for sham surgery and 20 for PAB surgery. Among these 40 mice, 20 were Fb-FoxO3-/- KOs, and 20 were WT. Schematic overview of experimental design as shown in (**figure 8**).

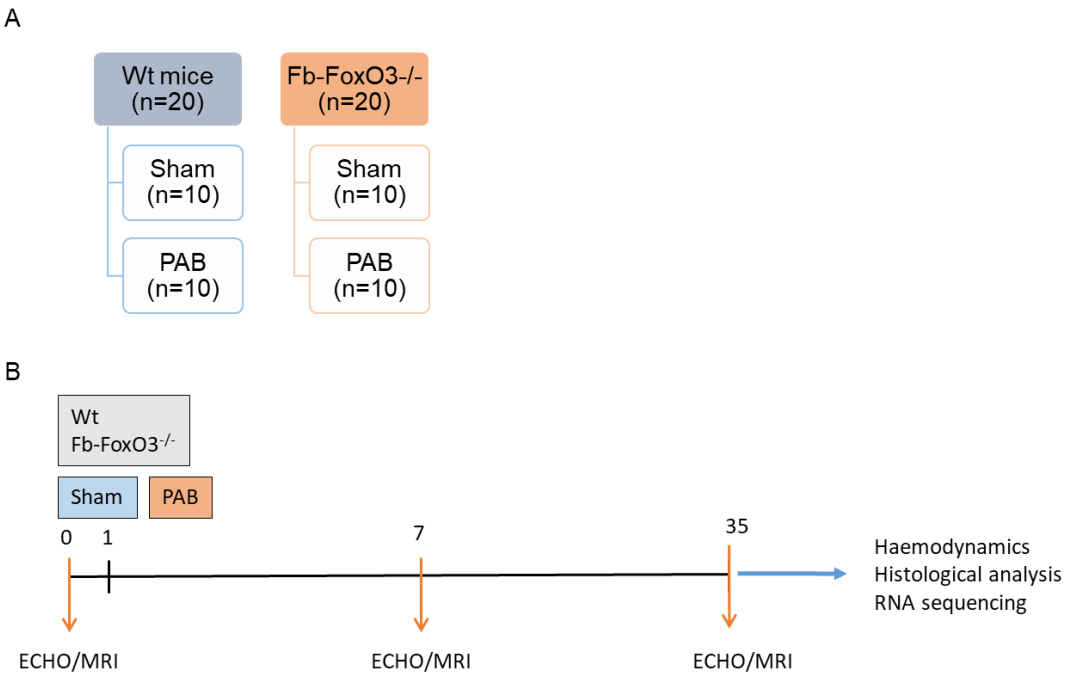

Figure 8. A. Randomization of Wildtype (Wt) and Fibroblast specific Foxo3 Knockout (Fb-Foxo3-/-) to Sham and PAB group. **B.** Schematic overview of experimental design

3.2.4 Mouse orotracheal intubation and ventilation

The intubation and surgical procedures were performed with a surgical microscope (Leica Microsystems, Wetzlar, Germany) at 8x magnification. An intravenous 22G x 1 in. catheter (Terumow Surflo, Emergency Medical Products Inc, Waukesha, WI, USA) serving as an endotracheal tube, appropriate stiff guide (e.g., Seldicath 2F, Laboratoire Plastimed, Saint-Leu-La-Foreˆt Cedex, France) to facilitate the introduction of a cannula as well as a pair of curved forceps (FST) were prepared. A drop of 1% lidocaine is put on the tip of the tube to numb the throat and reduce the gag reflex. A blunted needle attached to a 50-ml syringe, which was held on a retort stand, allowed the mouse to be fixed in a hanging position for the intubation procedure. As intubation requires both hands, the microscope was prefocused approximately 15 mm below the needle to the vocal cords' putative working field.

For induction of general anesthesia (Table Top Laboratory Animal Anesthesia System, VetEquip Inc, Pleasanton, USA), the animal was placed into a transparent Chamber induction chamber. 5% isoflurane (Forene® Abbott, Weisbach, Germany) in 100% oxygen (Air Liquid, Siegen, Germany) at a flow rate of 2 L/min was used until the animal lost its righting reflex. After that, the mouse was taken out and suspended by the superior incisors on a blunted needle attached to a 50-ml syringe, which was held on a retort stand. A power light with flexible horns (KL-200, Fiber Optics Schott, Mainz, Germany) was focused on the ventral neck to

transilluminate the trachea. The tongue of the mouse, held with the curved forceps held in the operator's right hand, was moved to the left. The left hand's forceps are put under the tongue to hold it firmly to the lower jaw. The vocal cords and trachea were then visualized. With the operator's free right hand, the intubation tube was gently inserted into the trachea for 6 mm starting from the vocal cords. Then the guide was removed, and the mouse was placed supine on a thermally controlled surgical table and connected to a small animal ventilator MiniVent type 845 (130 breaths/min, 225 µL stroke volume, and a positive-end expiratory pressure of 1 cm H2O, Hugo Sachs Elektronik, March-Hugstetten, Germany), with the exhaust tube immersed in water to confirm the flow of air. The success of the intubation was evaluated by the visual observation of the rhythmic expansion of the thorax synchronous with the ventilator. Maintenance of anesthesia was provided by continuous inhalation of 2% isoflurane mixed with oxygen (133).

3.2.5 Pulmonary artery banding model

Thirty minutes before surgery, an analgesic buprenorphine hydrochloride (Temgesic®, 0.1 mg/kg, Sigma-Aldrich, Germany) is given subcutaneously. The induction of anesthesia with the gaseous isoflurane is started by placing the animal in a box filled with 3-4% isoflurane mixed with oxygen. After induction, mice are intubated with a 20-gauge atraumatic cannula and placed supine on a thermally controlled surgical table. Mice are ventilated (130 breaths/min, 225 µL stroke volume, and a positive-end expiratory pressure of 1 cm H2O) using a mouse ventilator MiniVent type 845 (Hugo Sachs Elektronik, March-Hugstetten, Germany). Maintenance of anesthesia is provided by continuous inhalation of 2% isoflurane mixed with oxygen.

The left thoracic wall is shaved and cleaned with Braunoderm® (Braun, Melsungen, Germany). A transverse 5-mm incision of the skin is made with scissors 2 mm away from the left sternal border, 2 mm lower than the level of the armpit. Both layers of thoracic muscles are gently pulled apart. The chest cavity is opened with scissors by a small incision at the level of the second intercostal space 2–3 mm from the left sternal border. The chest retractor is gently inserted to spread the wound 4–5 mm in width, taking care to avoid the lungs getting caught in the teeth of the retractor. The thymus and fat are pulled away with forceps to the left arm of the retractor. With two forceps, the pericardial sac is gently pulled apart and attached to both arms of the retractor. After mobilization of the pericardium, the pulmonary trunk is visualized. The pulmonary trunk is bluntly dissected with curved forceps from the aorta and left atrium. To create a tunnel underneath the pulmonary trunk, an L-shaped 26-gauge blunted needle is used. The needle is placed from the side of the pulmonary trunk closest to the left atrium and

gently pushed underneath the pulmonary trunk so that the end of the needle appears between the pulmonary trunk and the aortic trunk.

Small titanium ligating clip (Hemoclip®, Edward Weck, and Research Triangle Park, NC, USA) is placed around the pulmonary trunk with specially adapted appliers set to width to produce 65-70% constriction. The chest retractor is removed, and the thymus is moved back to its physiological position. The lungs are then reinflated by shutting off the outflow on the ventilator for 1–2 s using a finger. The chest cavity is closed by combining the second and third ribs with two 6–0 prolene sutures. While making a knot, slight pressure is applied to the chest with the needle holder to reduce the free air volume in the chest cavity. All layers of muscle are moved back to their physiological position. Then, the skin is closed with a 6-0 prolene suture, and the wound is treated with Braunoderm® (Braun, Melsungen, Germany).

For the sham operation, dissection of the pulmonary trunk is performed using the L-shaped needle, but a ligating clip is not placed around the pulmonary artery. The lungs are then reinflated, and the wound is closed. Immediately after the operation, 0.5ml of 37°C saline is given subcutaneously. An analgesic buprenorphine hydrochloride (Temgesic®, 0.1 mg/kg, Sigma-Aldrich, Germany) is given subcutaneously every 8h for the next 48h. Once spontaneous respiration has resumed, animals are extubated, placed under a heating lamp, and closely observed for 6 hours to ensure a complete recovery from the anesthesia. The mice are then housed in a standard rodent cage with free access to food and water in a room kept at 23°C (133).

3.2.6 MCT-induced pulmonary hypertension model

Monocrotaline was dissolved in 0.5M HCl, and the pH was adjusted to 7.4 with 0.5M NaOH. A single subcutaneous injection of monocrotaline (60mg/kg, Sigma Aldrich) was administered to induce pulmonary hypertension in SD rats. Control rats received an equal volume of isotonic saline. Organs were harvested four weeks after saline/MCT injections.

3.2.7 Echocardiography

The VEVO2100 system was equipped with a 30-MHz, 100-frame-per-second micro-visualization linear probe (MS400, mouse cardiovascular) to perform echocardiography (Visual Sonics, Toronto, Canada). Anesthesia was initially administered to a mouse in an anesthesia induction chamber (Tabletop Laboratory Animal Anesthesia System, Vet Equip Inc. Pleasanton, USA) using 5% isoflurane and 100% oxygen at a flow rate of 1 L/min. The mouse was then positioned supine on an imaging platform. Throughout the investigation, the mouse's snout was maintained in a nasal cone attached to the anesthetic system to maintain a steady-

state sedation level (1 to 1.5 percent isoflurane mixed with 1 liter per minute of 100 percent oxygen) while the animal breathed freely. A rectal thermometer (Indus Instruments, Houston, TX) was used to monitor and maintain body temperature at 37°C. Both eyes were treated with Dexpanthenol ophthalmic ointment (Bepanthen® Bayer, Leverkusen, Germany) to avoid scleral dryness. The four paws of the mouse were attached to the electrocardiogram (ECG) electrodes with surgical tape and electrode gel to measure heart rate (HR). A cotton applicator tip was used to apply depilatory cream to the chest from the sternum to the diaphragm to eradicate chest hair. The cream was removed after two minutes with a gently rolling motion of tissue paper, and the chest was then washed with a cotton swab moistened with distillation water. To overcome air attenuation, a pre-warmed acoustic coupling gel (Aquasonic® 100, Parker Laboratories, Inc.) was applied to the chest wall of the sedated and immobilized mouse. The echocardiographic evaluation administered 1.5 to 2.5 percent isoflurane to maintain a physiological heart rate (HR). HRs were kept similar throughout experimental groups (400–550 bpm). If the HR was above the acceptable range, the isoflurane concentration was briefly raised to 4 - 5 percent and subsequently lowered to 1.5 - 2 percent until the HR approached the appropriate level. Alternatively, if the HR was below the necessary range, the isoflurane concentration might be adjusted to 0.5 percent and then raised.

Initially, a typical 2D echocardiographic examination was done in the parasternal long-axis view to evaluate LV dimensions and systolic performance. The picture depth, breadth, and gain parameters were adjusted to maximize image quality. The echocardiographic measures were obtained using the typical procedures outlined in previously published papers (134). RV free wall thickness (RVWT) was determined utilizing a right parasternal long-axis view with both M-mode and B-mode images. Either RVOT or LVOT blood flow characteristics were used to estimate cardiac output. RVOT VTI-derived CO. From the parasternal short-axis view (with the focus on PA) at the aortic valve level, two-dimensional pictures of the right ventricular outflow tract (RVOT) and pulsed-wave Doppler profiling of the pulmonary blood flow were acquired. The pulsed-wave Doppler sample was positioned at the tip of the pulmonary valve leaflets and aligned with color Doppler mode to enhance laminar flow. RVOT dimeter (RVOTd) was measured utilizing the parasternal short-axis view at the pulmonary valve levels during mid-systole. RVOT VTI was determined using the RVOT pulsed-wave Doppler flow velocity profile. Based on these echocardiographic measures, the RVOT stroke volume (SV) was computed as follows: SV = ((LVOTd) 2 x 3.14 x (VTI)/4) LVOT VTI-derived CO. The Doppler angle varied slightly, so the interrogation beam was perpendicular to the aortic flow to acquire the highest flow velocity. The left ventricular outflow tract (LVOT) flow velocity and velocity time integral (LVOT VTI) profiles were obtained from a right supraclavicular perspective. Using B-mode echocardiography at the center of the aortic valve during mid-systole and a modified left

parasternal log-axis view focused on the LVOT, the LVOT diameter (LVOTd) was measured. Based on these echocardiographic measures, the following formula was used to determine LVOT SV: SV = ((LVOTd) 2 x 3.14 x (VTI)/4)

Tricuspid annular systolic velocity (RVS') and tricuspid annular plane systolic excursion (TAPSE) were assessed to evaluate RV function. The M-mode cursor was positioned at the intersection of the tricuspid annulus and RV free wall using the apical four-chamber image to determine TAPSE. RVS' velocity was estimated using Tissue Doppler imaging (TDI) at the lateral aspect of the tricuspid annulus in the four-chamber view.

All echocardiographic image (M-mode, 2D, and flow) data were collected in triplicate, omitting the respiration peaks. All photos were taken between 10 and 25 minutes following induction of anesthesia, and computations were performed after acquisition. The chest wall was cleansed with tissue paper, and paw tapes were removed when the imaging was complete. The anesthetic was discontinued, and the mouse was allowed to recuperate while unrestrained on the heated ECG pad. The mouse was returned to its cage after it regained consciousness.

3.2.8 MRI, hemodynamic, and RV hypertrophy measurements

Cardiac MRI was performed on days 0 (pre-OP), or 35. Cardiac MRI measurements were performed on a 7.0T Bruker PharmaScan, equipped with a 300mT/m gradient system, using a custom-built circularly polarized birdcage resonator and the IntraGateTM self-gating tool (Bruker, Ettlingen, Germany). Mice were measured under the influence of isoflurane (2.0% v/v) anesthesia delivered in an oxygen/medical air (0.5/0.5 L/min) mixture. Body temperature was maintained at 37 ◦C throughout the experiment. The measurement is based on the gradient echo method (repetition time = 6.2ms; echo time = 1.6ms; field of view = 2.20x2.20 cm; slice thickness = 1.0mm; matrix = 128x128; repetitions = 100; resolution 0.0172 cm/pixel). The imaging plane was localized using scout images showing the sagittal and coronal view of the heart, followed by axial acquisition orthogonally to the septum of both scout scans. Multiple (9–10) contiguous axial slices were acquired for complete coverage of the left and right ventricle. MRI data were analyzed using Qmass digital imaging software (Medis, Leiden, Netherlands) (135-137).

Invasive hemodynamic measurements were performed as described previously (48). Briefly, mice were anesthetized using isoflurane and fixed on a homeothermic plate (AD Instruments, Spechbach, Germany) in a supine position. A rectal probe was inserted to measure the core body temperature and was maintained at 37 ºC. A high-fidelity 1.4F micromanometer/Mikro-Tip Pressure catheter (Millar Instruments, Houston, TX) was inserted into the right ventricle through the right jugular vein to measure the RVSP. Systemic arterial pressure (SAP) was

measured by catheterizing the LV through the left carotid artery. Data were analyzed using the PowerLab data acquisition system (MPVS-Ultra Single Segment Foundation System. AD Instruments) and LabChart 7 software. The heart and lungs were perfused with PBS and harvested after the measurements. The RV was separated from the LV and the septum (S) to calculate the Fulton index (weight ratio of RV/(LV+S)).

3.2.9 Cell Culture

Human cardiac fibroblasts (HCFs) were grown on poly-lysine coated dishes in a fibroblast medium supplemented with FBS, FGS, penicillin, and streptomycin. Cells were maintained at 37 °C in a 5% CO2 incubator. Experiments were performed with cells from passages 5 to 6. A basal medium supplemented with 0.1% FCS was used for serum starvation.

3.2.10 Transfection with siRNA

Human CFs were transfected with different siRNAs using Lipofectamine 3000 Transfection Reagent (Invitrogen) in an optiMEM serum-free medium. FOXO3 siRNA (Cat. No. 4392420 and All Stars negative siRNA (Cat. No. 1027281) as non-silencing control (si_NS) were obtained from Qiagen. Cells were transfected with siRNA for 6 hours in the serum-free medium.

3.2.11 Cell culture with matrix stiffness plates

Ready-to-use hydrogels were pre-coated with rat tail collagen type 1 bound to 100mm petrisoft™ polystyrene dishes (Cell Guidance Systems Ltd). To mimic the physiological and pathophysiological matrix stiffness, we used petrisoft™ dishes with Young's (elastic) modulus of 0.5 kPa (soft matrix), 12kPa (medium matrix) and 50 kPa (stiff matrix) as described previously (32). Human cardiac fibroblasts (HCFs) (700,000 cells per dish) were plated onto dishes with soft and stiff matrices after 24h. Cells were treated with Trifluoperazine dihydrochloride (TFP) (10µM) for 24h. Later cells were trypsinized and the cell suspension was divided for subsequent RNA and protein extraction.

3.2.12 RNA isolation, cDNA synthesis and qRT-PCR

Total mRNA from heart tissues was isolated using miRNeasy micro Kit/RNeasy mini Kit (Qiagen, Germany) following the manufacturer's protocol. The procedure included the proteinase K digestion step for removing abundant proteins in fiber-rich PAB right ventricles. 20-30 mg of heart tissue was used for each sample. Tissue was homogenized prior to isolation in RLT buffer (provided by kit) using Precellys homogenizer (Peqlab, Germany). Total mRNA from cells was isolated using miRNeasy micro Kit (Qiagen, Germany) following the

manufacturer's protocol. RNA concentration and purity were determined using Nanodrop (Thermo Scientific). cDNA synthesis with equal amounts of RNA was performed using a High-capacity cDNA reverse transcription kit (Applied Biosystems) according to the manufacturer's instructions (**Table 3**).

Table 3. Compounds of master mix for reverse transcription

Applied Biosystems Kit	
Components	**Volume**
RNA (1ug)	
Dnase/Rnase-free H2O	10 - Vol of RNA
Total	10ul
Components	**1x (ul)**
10x RT buffer	2
25x dNTP mix	0,8
10xRT Random primers	2
ddH20	3,7
Rnase inhibitor	0,5
Reverse Transcriptase	1
Total	10ul
Total volume for reaction	**20ul**

qPCR was performed with StepOnePlus™ real-time PCR systems (Applied Biosystems) (**Table 4**) using the PCR protocol mentioned in (**Table 5**). For comparison of expression levels, Ct values of the gene of interest (GOI) were normalized to reference gene Porphobilinogen Deaminase (PBGD) or Hypoxanthine Phosphoribosyltransferase 1 (HPRT1). ΔCt was calculated as ΔCt = Ct (reference gene) – Ct (gene of interest). Higher ΔCt values indicate higher expression.

Table 4. qRT-PCR reaction mix composition

Components	**Volume (µl)**
iTaq™ Universal SYBR® Green Supermix	7
Forward primer, 10 µM	0.5
Reverse primer, 10 µM	0.5
cDNA template	2
Nuclease free water	10

Table 5. qPCR reaction steps

qRT PCR steps	Temperature	Time	Number of repeats
Initial denaturation	95°C	3 min	1
Denaturation	95°C	10 sec	
Annealing	60°C	30 sec	40
Elongation	72°C	30 sec	
Denaturation	95°C	10 sec	1
Melting curve	65°C to 95°C	Increment 0.5°C for 5 sec	1

3.2.13 RNA sequencing

All the RNA sequencing protocols were performed at the Bioinformatics core facility (Deep Sequencing Platform Service group) at the Max Planck Institute for heart and lung research, Bad Nauheim, by Dr. Stefan Guenther

From RV tissues

For RNA-seq analysis, total RNA was isolated from RV tissues using the RNeasy mini kit (Qiagen) combined with on-column DNase digestion (DNase-Free DNase Set, Qiagen) to avoid contamination by genomic DNA. RNA and library preparation integrity was verified with LabChip Gx Touch 24 (Perkin Elmer). 750ng of total RNA was used as input for VAHTS Stranded mRNA-seq Library preparation following the manufacturer's protocol (Vazyme). Sequencing was performed on the NextSeq500 instrument (Illumina) using v2 chemistry with a 1x75bp single-end setup. The resulting raw reads were assessed for quality, adapter content and duplication rates with FastQC (Andrews S. 2010, FastQC: a quality control tool for high throughput sequence data. Available online at: http://www.bioinformatics.babraham.ac.uk/projects/fastqc). Trimmomatic version 0.39 was employed to trim reads after a quality drop below a mean of Q20 in a window of 5 nucleotides (Bolger et al., Trimmomatic: a flexible trimmer for Illumina sequence data). Only reads between 30 and 150 nucleotides were cleared for further analyses. Trimmed and filtered reads were aligned versus the Ensembl mouse genome version mm10 (ensemble release 101) using STAR 2.7.7a with the parameter "--outFilterMismatchNoverLmax 0.1" to increase the maximum ratio of mismatches to mapped length to 10% (Dobin et al., STAR: ultrafast universal RNA-seq aligner). The number of reads aligning to genes was counted with featureCounts 1.6.5. tool from the Subread package (Liao et al., featureCounts: an efficient general purpose program for assigning sequence reads to genomic features). Only reads mapping at least

partially inside exons were admitted and aggregated per gene. Reads multiple overlapping genes or aligning to multiple regions were excluded. Differentially expressed genes were identified using DESeq2 version 1.30.0 (Love et al., Moderated estimation of fold change and dispersion for RNA-Seq data with DESeq2). Only genes with a minimum fold change of +- 2 (log2 = +-1), a maximum Benjamini-Hochberg corrected p-value of 0.05, and a minimum combined mean of 5 reads were significantly differentially expressed. The Ensemble annotation was enriched with UniProt data (release 06.06.2014) based on Ensembl gene identifiers (Activities at the Universal Protein Resource (UniProt)).

From Human Cardiac Fibroblasts

1µg of total RNA was input for VAHTS Stranded mRNA-seq Library preparation following the manufacturer's protocol (Vazyme). Sequencing was performed on the NextSeq2000 instrument (Illumina) using a P3 flow cell with a 1x72bp single-end setup. The resulting raw reads were assessed for quality, adapter content and duplication rates with FastQC (Andrews S. 2010, FastQC: a quality control tool for high throughput sequence data. http://www.bioinformatics.babraham.ac.uk/projects/fastqc). Trimmomatic version 0.39 was employed to trim reads after a quality drop below a mean of Q20 in a window of 5 nucleotides (Bolger et al., Trimmomatic: a flexible trimmer for Illumina sequence data). Only reads between 30 and 150 nucleotides were cleared for further analyses. Trimmed and filtered reads were aligned versus the Ensembl human genome version hg38 (ensemble release 104) using STAR 2.7.9a with the parameter "--outFilterMismatchNoverLmax 0.1" to increase the maximum ratio of mismatches to mapped length to 10% (Dobin et al., STAR: ultrafast universal RNA-seq aligner). The number of reads aligning to genes was counted with featureCounts 2.0.2. tool from the Subread package (Liao et al., featureCounts: an efficient general purpose program for assigning sequence reads to genomic features). Only reads mapping at least partially inside exons were admitted and aggregated per gene. Reads overlapping multiple genes or aligning to multiple regions were excluded. Differentially expressed genes were identified using DESeq2 version 1.30.0 (Love et al., Moderated estimation of fold change and dispersion for RNA-Seq data with DESeq2). Only genes with a minimum fold change of +- 2 (log2 = +-1), a maximum Benjamini-Hochberg corrected p-value of 0.05, and a minimum combined mean of 5 reads were significantly differentially expressed. The Ensemble annotation was enriched with UniProt data (release 06.06.2014) based on Ensembl gene identifiers (Activities at the Universal Protein Resource (UniProt))

3.2.14 Protein isolation and Western Blotting

Cells were homogenized in RIPA buffer containing 1x protease and phosphatase inhibitor cocktail (Thermo Scientific, USA). Heart tissue was homogenized in Precellys homogenizer (Peqlab, Germany) with 500µl of RIPA buffer with protease/phosphatase inhibitor cocktail. Subsequently, the samples were centrifuged for 30 min at 14000 rpm. Protein concentration was measured using BioRad DC Protein Assay. Equal amounts of protein were loaded onto 10% polyacrylamide gels (**Table 6**) in running buffer (**Table 7**) and were transferred onto the PVDF membrane. The transfer was carried out for 1h and 25 min at 100 V in a blotting buffer (**Table 8**). Membranes were blocked for 1h in 5% milk and incubated overnight with the primary antibodies at 4°C with shaking. Post washing, membranes were incubated with appropriate horseradish peroxidase (HRP)-conjugated secondary antibodies, followed by developing with SuperSignal West Femto Chemi-luminescent Substrate (Thermo Scientific, USA) and capturing the signal using an Image reader (GE Healthcare). Densitometric analysis of the blots was acquired using multi gauge software (Fujifilm, Tokyo, Japan). Expression was quantified using band intensity values (in arbitrary units) normalized to ACTB or GAPDH.

Table 6. Composition of Gel

Gel Component	**Percentage of gel**	
	6% (Stacking gel)	**10% (Resolving gel)**
Acrylamide 30%	0.625mL	1.5mL
Tris-HCL	0.5mL	2mL
SDS 10%	25µL	60µL
APS 10%	12.5µL	30µL
TEMED	2.5µL	6µL
Water upto final volume	1.3mL	2.4mL

Table 7. Running buffer composition

Components	**Final concentration**
Tris	25mM
Gycline	250mM
SDS 10% (w/v)	0.10%
Water	Up to final volume

Table 8. Blotting buffer composition

Components	Final concentration
Tris	50mM
Gycline	40mM
Methanol (v/v)	20%
Water	Upto final volume

3.2.15 Immunofluorescence

After various treatments, cardiac fibroblasts were fixed in PBS/PFA 4% for 10 min and permeabilized with PBS/Triton 100X 0.1% for 10min at room temperature. The cells were then washed with 1x PBS and blocked with 5% BSA solution for 1h at RT. Primary antibodies were diluted in 3% BSA and incubated overnight at 4°C. The next day, cells were incubated with appropriate secondary antibodies, and nuclei were counterstained with DAPI. Images were acquired using Zeiss LSM 710 confocal microscope or Leica fluorescence microscope.

3.2.16 Histological and immunofluorescence analyses of mouse right ventricles

Mouse RVs were fixed with 4% PFA at 4ºC overnight and embedded in paraffin, sectioned at 5µm and stained with wheat germ agglutinin (WGA) conjugated with Alexa-488 to determine cardiomyocyte cross-sectional area (CSA), with isolectin B4 (IB4) conjugated with Alexa-594 to assess the capillary density. To assess the degree of fibrosis, RV sections were stained with Picrosirius red (Direct red 80, Sigma, cat. no. 365548). Subsequently, imaged and quantified by calculating the ratio of picrosirius red-stained connective tissue area (stained red) to total myocardial area (stained yellow) using Leica Qwin V3 computer-assisted image analysis software and macro program "Collagen" (Leica Microsystem, Wetzlar, Germany) as described previously (1,3). CSA was measured using Image J (NIH, USA). At least 10 randomly chosen areas per section were imaged and quantified at 40x magnification.

For staining, mouse hearts from Sham and PAB animals were harvested and washed in cold HBSS (Gibco, USA) buffer. Right and left ventricles were separated and embedded in Tissue-Tek OCT compound (Sakura, USA), frozen on dry ice. About 6-10µm sections were cut and mounted on glass slides. Sections were postfixed with ice-cold acetone and methanol (1:1) for 10mins at room temperature (RT). Sections were permeabilized with PBST (0.1% Triton X-100 in PBS) for 10mins, blocked with 5% BSA for 1h at RT and incubated with primary antibodies diluted in 3% BSA at 4ºC overnight. Post washing sections were incubated with

secondary antibodies and Draq5 at RT for 1h. After three washes, sections were mounted with Dako mounting medium. Images were taken using Zeiss LSM 710 microscope

3.2.17 Statistical analysis

Data were plotted as individual data points with mean in addition. Statistical analysis was performed in GraphPad Prism Version 9 (GraphPad Software Inc., SanDiego, CA, USA) using a two-tailed unpaired Student's t-test for experiments with two groups or one-way ANOVA with Dunnett´s multiple comparison test for time-course experiments or two-way ANOVA with Sidak's correction for posthoc multiple comparisons for experiments including multiple groups. Kaplan-Meier survival analysis was used to determine mortality risk following the PAB procedure. A P value less than 0.05 was considered statistically significant. In the figures, asterisks denote statistical significance (*P < 0.05; **P < 0.01; ***P < 0.001; ****P < 0.0001).

4. RESULTS

4.1 FOXO3 is increased explicitly in compensated RV and significantly decreased in decompensated RV of PAH patients

To explore the role of FOXOs in RV remodeling in PAH, we first assessed the FOXOs expression pattern in healthy human RV (hRV) versus compensated RV (cRV) and decompensated RV (dcRV) from PAH patients. *FOXO3* expression was significantly increased in cRV compared with control and decreased in dcRV compared with cRV from PAH patients. Whereas *FOXO1* expression was unchanged and *FOXO4* expression was increased in cRV compared to hRV (**Figure 9A–9C**)

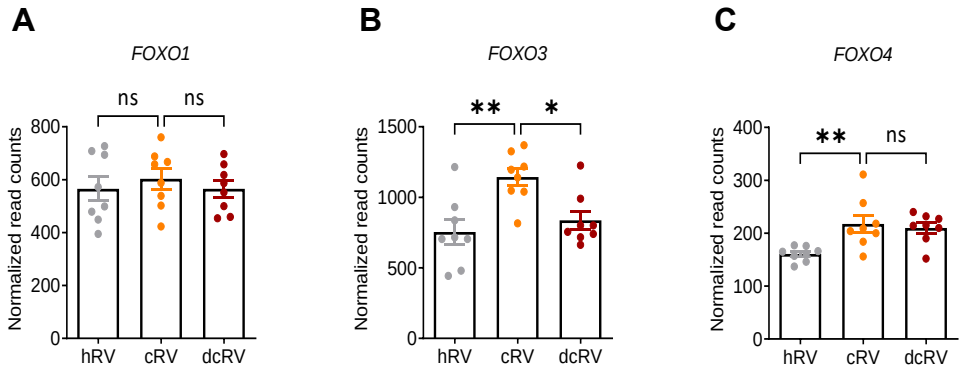

Figure 9. Expression of FOXO isoforms in RVs of human PAH patients. A–C) Normalized read counts of *FOXO1, FOXO3* and F*OXO4* derived from RNA sequencing of healthy, compensated (cRV) and decompensated RV (dcRV) tissues homogenates. hRV (n=8), cRV (n=8), dcRV (n=8). Error bars indicate the mean with SEM. Data were analyzed using one-way ANOVA with tukey's multiple comparisons test. *p<0.05, **p<0.01, ns=not significant.

Similarly, the known target genes of the FOXO signaling pathway which are involved in various cellular processes such as autophagy (*GABARAP*), cell cycle regulation (*GADD45A*), Immune regulation (*S1PR1*), oxidative stress and DNA repair (*SOD2*), metabolism (*ACOX1*) and muscle atrophy (*FBXO32*) were also significantly regulated in cRV and dcRV of PAH patients (**Figure 10A–10F**).

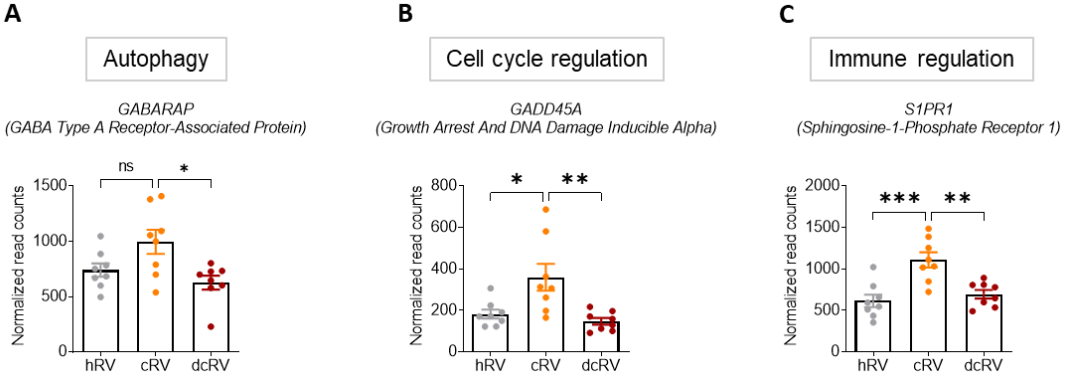

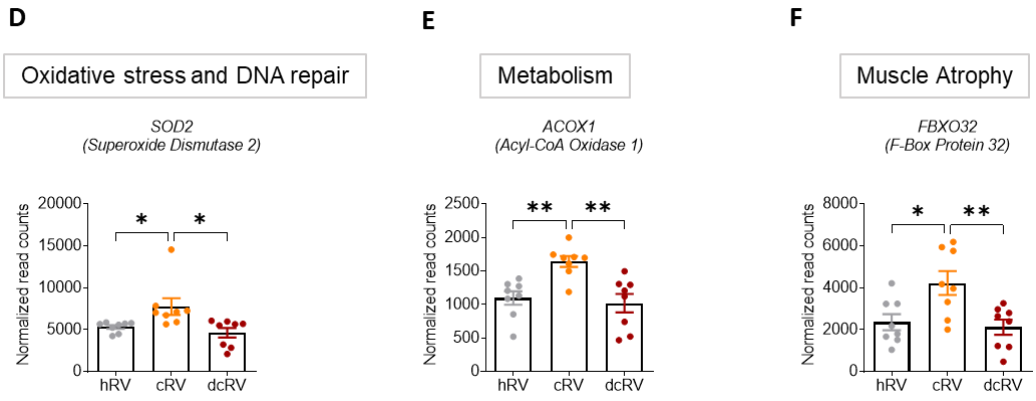

Figure 10. Expression of FOXO signaling target genes in RVs of human PAH patients. A–F) Normalized read counts of *GABARAP, GADD45A, S1PR1, SOD2, ACOX1* and *FBXO32* derived from RNA sequencing of healthy, compensated (cRV) and decompensated RV (dcRV) tissues homogenates. hRV (n=8), cRV (n=8), dcRV (n=8). Error bars indicate the mean with SEM. Data were analyzed using one-way ANOVA with tukey's multiple comparisons test. *p<0.05, **p<0.01, ***p<0.001, ns=not significant.

4.1.1 mRNA expression of FOXO1 and FOXO3 is downregulated in compensated and decompensated RV of PAH patients

Next, we performed mRNA expression analysis using qRT-PCR from the cDNA reverse transcribed from RNA extracted from RV of hRV, cRV and dcRV. Correspondingly, the mRNA expression of both *FOXO1* and *FOXO3* was unchanged in the cRV state but was significantly downregulated in the dcRV state (**Figure 11**).

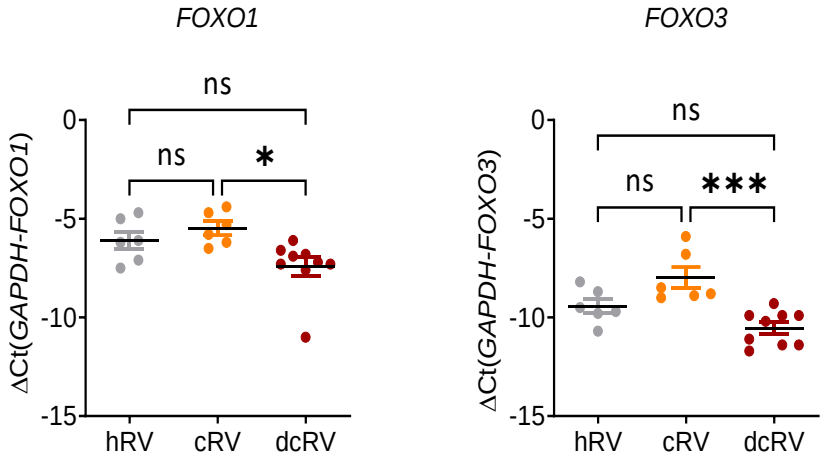

Figure 11. mRNA expression of *FOXO1* and *FOXO3* isoforms in RVs of human PAH patients. *FOXO1* and *FOXO3* mRNA expression in healthy, compensated (cRV) and decompensated (dcRV) RVs. hRV (n=6), cRV (n=6), dcRV (n=9). Error bars indicate the mean with SEM. Data were analyzed using one-way ANOVA with tukey's multiple comparisons test. *p<0.05, ***p<0.001, ns=not significant.

4.1.2 Reduced immunoreactivity of FOXO3 in decompensated RV of PAH patients

The histological expression pattern of FOXO3 was assessed by immunofluorescence staining in the RV sections of healthy controls, compensated and decompensated PAH patients. The staining of RV sections with wheat gram agglutinin (WGA) indicated hypertrophy in cardiomyocytes in both cRV and dcRV. Consistent with RNA seq and quantitative real-time PCR results, the overall signal intensity of FOXO3 was increased in cRV and decreased in dcRVs. The signal was predominantly in the nucleus in hRV, in the nucleus and the cytoplasm in cRV and almost completely absent in dcRV (**Figure12**)

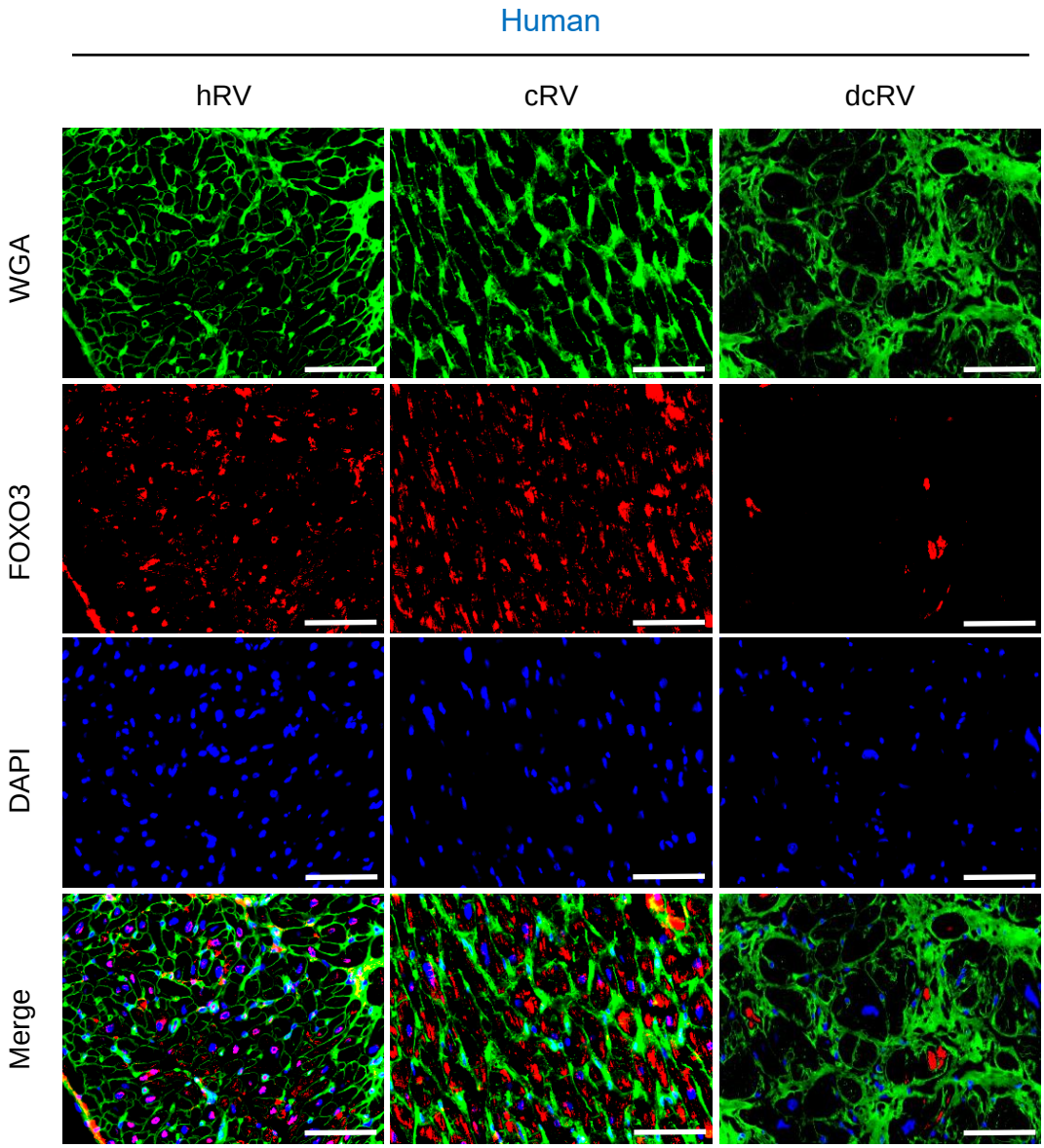

Figure 12. Immunolocalization of FOXO3 in human healthy, compensated and decompensated RV tissues. Representative immunofluorescence stainings of WGA (green), FOXO3 (red) and DAPI (blue). hRV (n=3), cRV (n=3) and dcRV (n=3). Scale bar: 50µm.

4.2 Transcriptional downregulation of Foxo isoforms in MCT induced RV failure in rats

Further to explore the expression pattern of Foxos in the animal models classically used to study the evolution of RV remodeling, which essentially also mimics the molecular and histological features described in PAH patients. We first employed the MCT (5 weeks) rat model, which mimics the natural course of RV failure. Interestingly, all the Foxo isoforms (*Foxo1, Foxo3*, and *Foxo4*) are transcriptionally downregulated in RV of rats injected with MCT relative to their respective controls (**Figure 13A–13C**). Similar to human decompensated RV, Foxos were significantly downregulated in MCT RV.

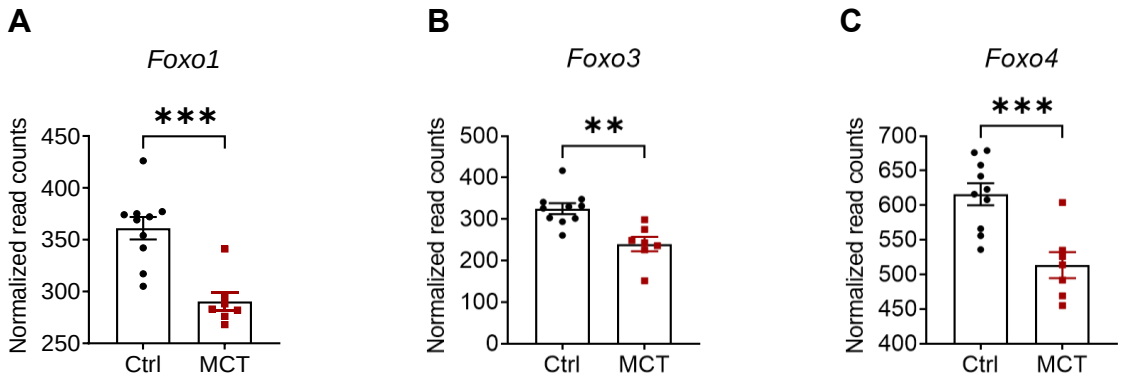

Figure 13. Expression of FoxO isoforms in RV of MCT rats. A-C) Normalized read counts of *Foxo1*, *Foxo3* and *Foxo4* derived from RNA sequencing of control (n=10) and MCT (5 weeks) (n=7) rat RV tissues homogenates. Error bars indicate the mean with SEM. Data were analyzed using one-way ANOVA with tukey's multiple comparisons test. **p<0.01, ***p<0.001.

Next, we performed mRNA expression analysis using qRT-PCR from the cDNA reverse transcribed from RNA extracted from RV of control and MCT rats. Similarly, the mRNA expression of *Foxo3* was significantly downregulated in the MCT rats (**Figure 14**).

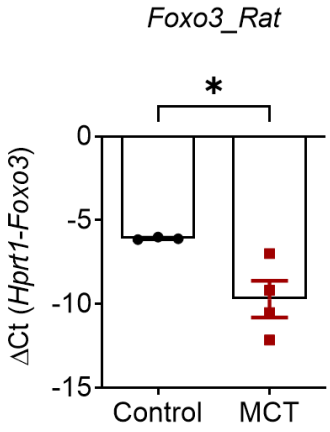

Figure 14. mRNA expression of *Foxo3* in RV of MCT rats. *Foxo3* mRNA expression in control (n=3) and MCT (n=4) RV. Error bars indicate the mean with SEM. Data were analyzed using an unpaired t-test. *p<0.05.

4.2.1 Dysregulated activity of Foxo3 in MCT induced RV failure in rats

Next, we assessed the total and phosphorylated protein expression levels of Foxo3 in cytoplasmic and nuclear lysate fractions from RV homogenates of control and MCT rats. Western blot analysis (**Figure 15A**) and subsequent densitometric quantification demonstrated a significant decrease in the total foxo3 levels (**Figure 15B**) and a significant increase in the phosphorylation levels of foxo3 (**Figure 15C**) in the nuclear fraction of MCT RV compared to controls. However, there was no significant change in the cytoplasmic levels of foxo3 in both MCT and control RV.

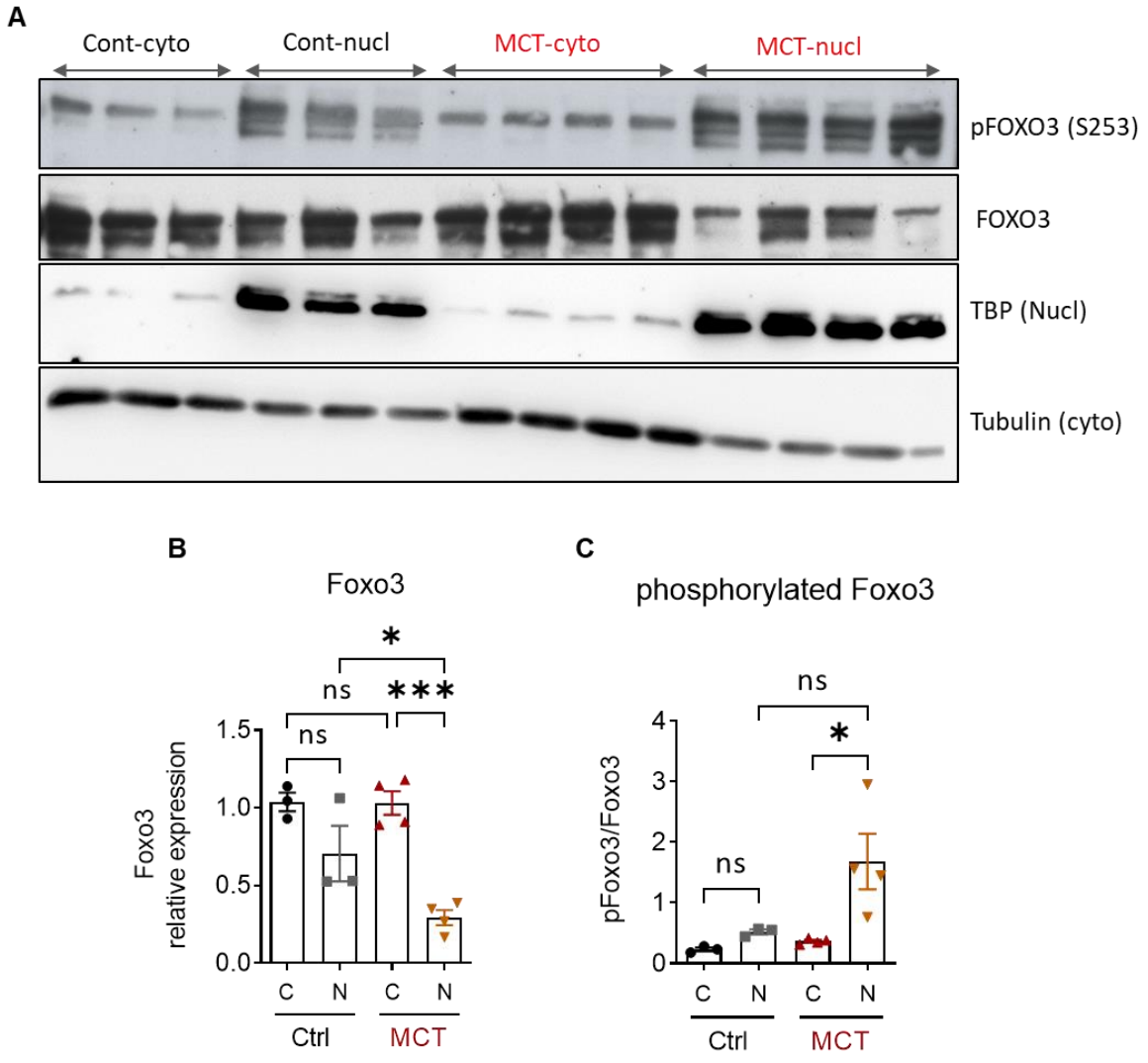

Figure 15. Protein expression of Foxo3 in RV of MCT rats. A) Representative western blot images of cytoplasmic and nuclear protein lysates of control (n=3) and MCT (n=4) rat RV tissues homogenates. **B, C)** Densitometric quantification of the western blots. Error bars indicate the mean with SEM. Data were analyzed using one-way ANOVA with tukey's multiple comparisons test. *p<0.05, ***p<0.001, ns=not significant.

4.2.2 Reduced immunoreactivity of Foxo3 in MCT-induced RV failure in rats

The histological expression pattern of Foxo3 was assessed by immunofluorescence staining in the RV sections of control and MCT RVs. Consistent with stainings from human hRVs, the signal was predominantly in the nucleus in the control RV and the overall signal intensity was decreased in MCT rats, similar to human dcRVs. (**Figure 16**).

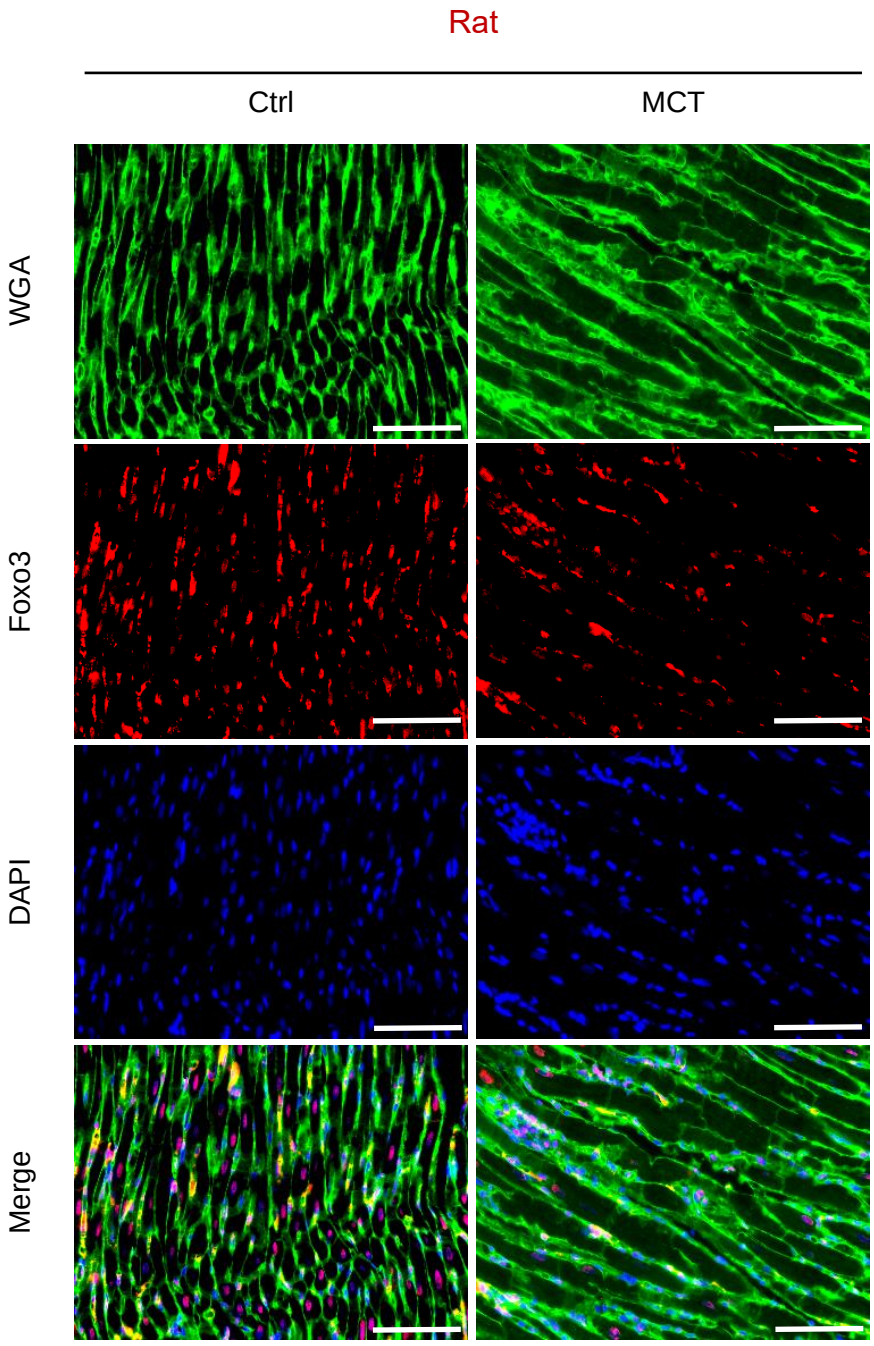

Figure 16. Immunolocalization stainings of Foxo3 in control and MCT RV tissues. Representative immunofluorescence stainings of WGA (green), Foxo3 (red) and DAPI (blue). Ctrl (n=3), MCT (n=3). Scale bar: 50µm.

4.3 Expression of Foxo3 in pulmonary artery banding (PAB) model of RV dysfunction

The next preclinical animal model we employed is the PAB model of RV dysfunction. This model is based on the narrowing of the internal diameter of the main pulmonary artery, which serves as a model of RV failure. This model does not impact the pulmonary vasculature but exhibits direct effects on the RV due to increased pressure overload. Two time points of PAB were employed to understand RV's compensated (day 35) and decompensated states (day 53). A cardiac functional assessment revealed a decrease in the ejection fraction (RVEF) and an increase in RVSP and Fulton index (RV/LV+S) in the PAB group at both time points compared to their respective sham groups. Although not significant, the RVEF and Fulton index were worsened to a greater degree at day 53 of PAB (**Figure 17A–C**)

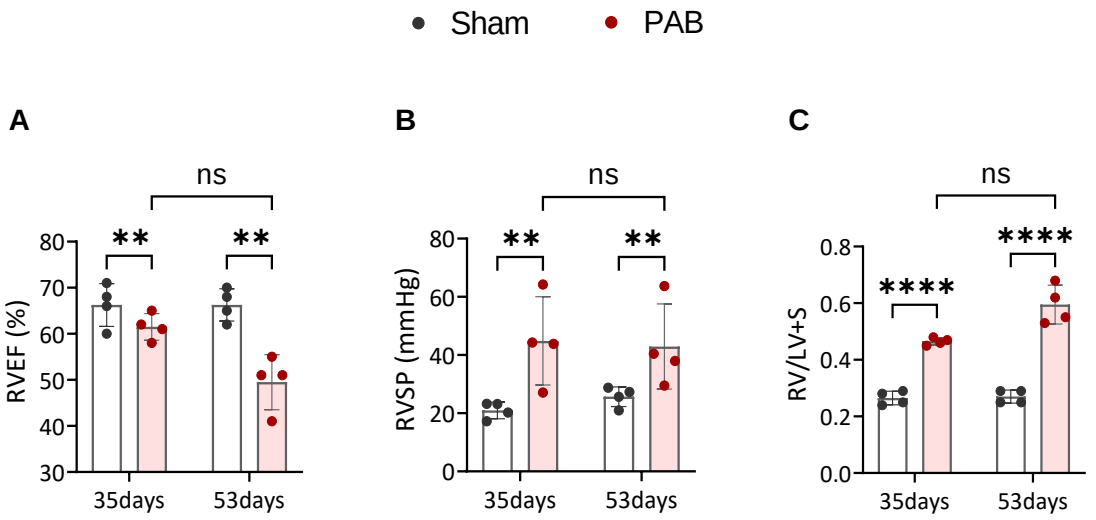

Figure 17. Cardiac function, Haemodynamic and RV hypertrophy measurements in rats subjected to PAB. RV ejection fraction (RVEF), RV systolic pressure (RVSP) and Fulton index (RV/LV+S) measured in Sham (n=4) and PAB (n=4) at day 35 and day 53 post PAB. Error bars indicate the mean with SEM. Data were analyzed using two-way ANOVA with tukey's multiple comparisons test. **p<0.01, ****p<0.0001, ns=not significant.

Further, we assessed the expression of the total and phosphorylated state of Foxo3 in the compensated state of RV hypertrophy. We subjected rats to sham or PAB surgery and harvested the RV tissues after 5 weeks (35d) and isolated protein. Western blot analysis revealed foxo3 localized in the nucleus and the phosphorylated Foxo3 at serine 253 residue (pFoxo3 (S253)) in both cytoplasm and nucleus (**Figure 18A**). Although there was no significant difference in the total Foxo3 levels (**Figure 18B**), pFoxo3 levels were significantly reduced in the nucleus of rats subjected to PAB compared to sham animals (**Figure 18C**), which corroborates the findings from humans where foxo3 expression was increased at the compensated state of RV.

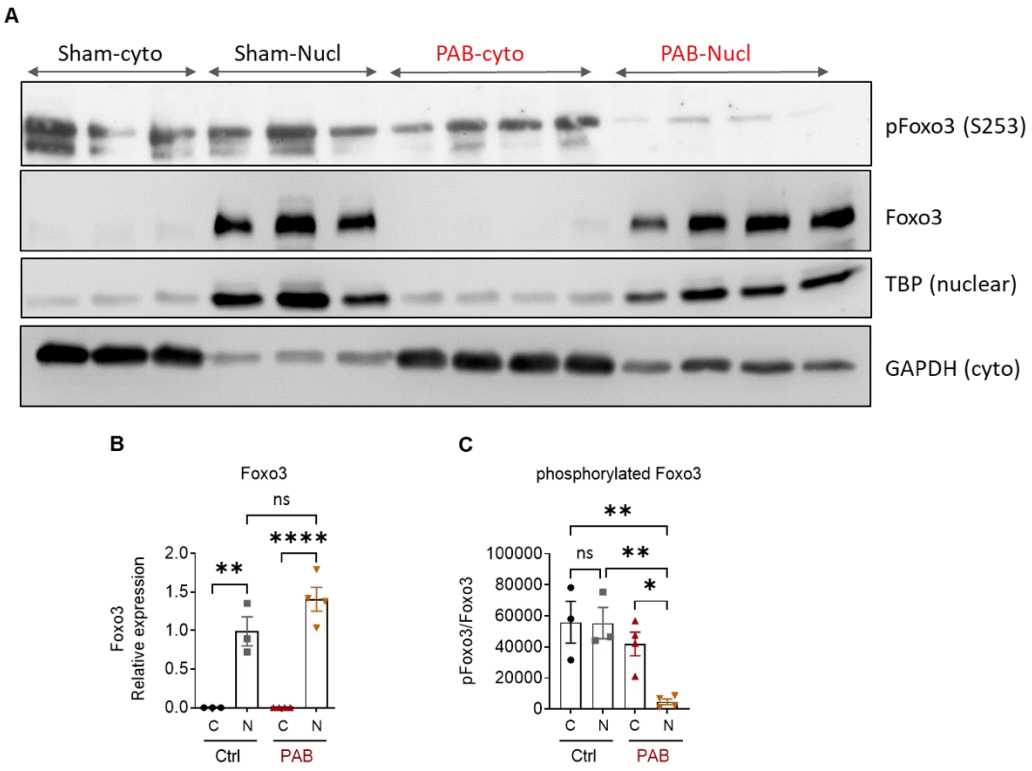

Figure 18. Protein expression of Foxo3 in RV of PAB 35days rats. A) Representative western blot images of cytoplasmic and nuclear protein lysates of Sham (n=3) and PAB35days (n=4) rat RV tissues homogenates. B, C) Densitometric quantification of the western blots. Error bars indicate the mean with SEM. Data were analyzed using one-way ANOVA with tukey's multiple comparisons test. *p<0.05, **p<0.01, ****p<0.0001, ns=not significant.4.3.1

4.3.1 Downregulation of Foxo3 in pulmonary artery banding (PAB) induced RV failure

We assessed the expression of Foxo3 in sham and PAB rats (53days). Similar to findings in humans and the MCT model, *Foxo3* mRNA expression in the decompensated RV was significantly downregulated in rats subjected to PAB (Figures **19A and 19B**).

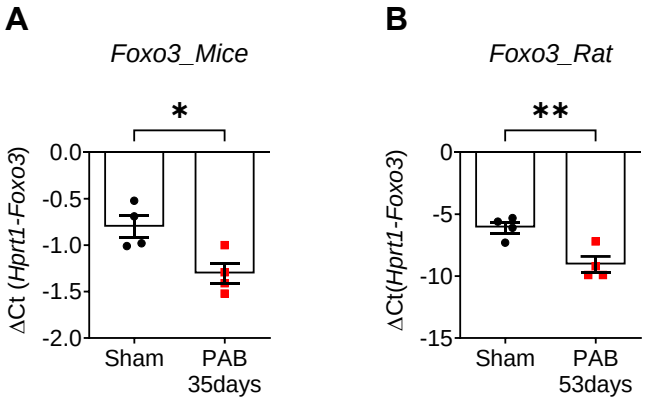

Figure 19. mRNA expression of *Foxo3* in RV of PAB in rodents. A) *Foxo3* mRNA expression in sham (n=4) and PAB 35d (n=4) mice RV. **B)** *Foxo3* mRNA expression in sham (n=4) and PAB 53d (n=4) rat RV. Error bars indicate the mean with SEM. Data were analyzed using an unpaired t-test. *p<0.05, **p<0.01.

The histological expression pattern of Foxo3 was assessed by immunofluorescence staining in the RV sections of Sham and PAB RV. Consistent with stainings from human RVs, the signal was predominantly in the nucleus in the sham RV; however, the overall signal intensity was decreased in rats subjected to PAB (**Figures 20**).

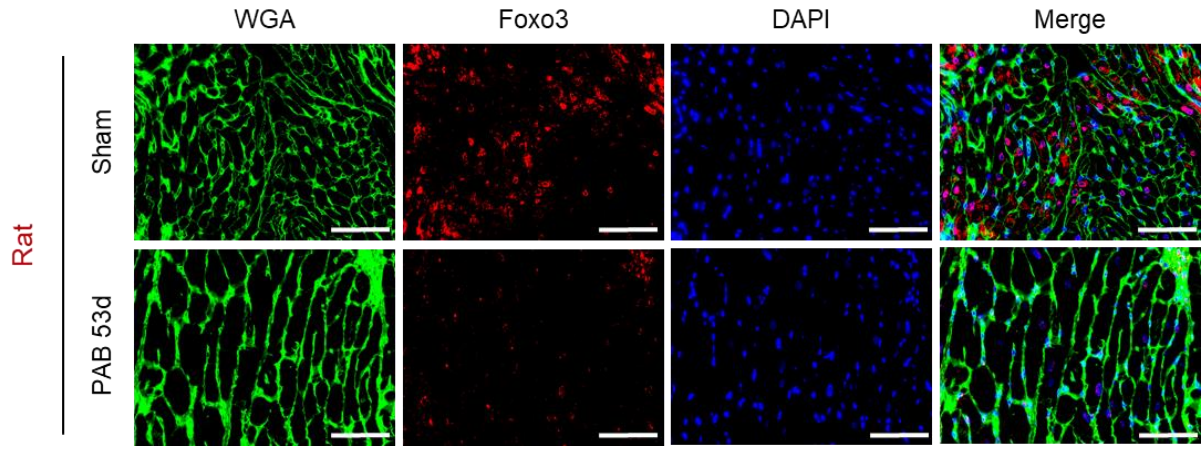

Figure 20. Immunolocalization stainings of Foxo3 in control and PAB RV tissues. A) Representative immunofluorescence stainings of WGA (green), Foxo3 (red) and DAPI (blue), Sham (n=3), PAB 53days (n=3) rat RV. Scale bar: 50µm.

4.4 FOXO3 expression is downregulated in cardiac fibroblasts (CFs) when cultured on a stiff matrix

Mechanically, fibrosis is distinguished by matrix stiffness, which has been demonstrated to enhance CF activation, thus accelerating the progression of fibrosis via a positive feedback process (138). To delineate whether mechanical or physical cues conveyed by ECM stiffness modulated the expression of FOXO3 in CFs, we used matrigel coated cell culture dishes with different stiffness (0.5/12/50 kPa) to mimic the normal, compensated and decompensated states of myocardial tissues (**Figure 21A and 21B**).

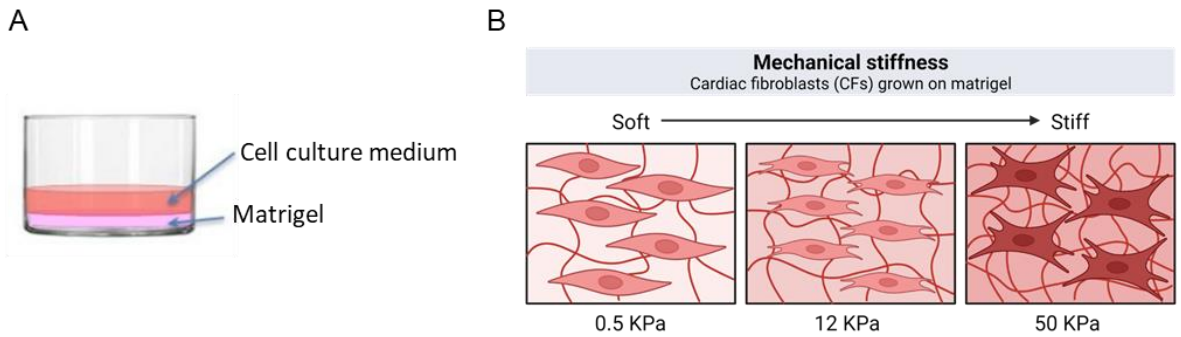

Figure 21. Expression of FOXO3 in CFs cultured on soft and stiff matrix. A) Graphical image illustrating the later view of a cell culture well coated with matrigel. **B)** Representative graphical illustration of cardiac fibroblasts cultured on soft, medium and stiff matrix gels.

We performed mRNA and protein expression analysis of total and phosphorylated FOXO3 in cardiac fibroblasts cultured on soft (0.5 kPa), medium (12 kPa) and stiff matrix (50 kPa). Although the mRNA expression of FOXO3 was not significantly altered in CFs when cultured on medium and stiff matrix, there is an appreciable downward trend in the expression in the medium matrix and increased in the stiff matrix (**Figure 22A**). We next assessed the total and phosphorylated levels of FOXO3. Interestingly, the levels of pFOXO3 were increased and total FOXO3 levels were decreased with an increase in stiffness of the matrix. The consequences of FOXO3 downregulation lead to activation of extracellular matrix (ECM) protein markers like Periostin (POSTN) in CFs cultured on the stiff matrix (**Figures 22B and 22C**). Through immunofluorescence staining, we found that different hydrogel stiffnesses imposed different degrees of CF activation, where the expression of FOXO3 was decreased with increasing matrix stiffness (**Figure 22D**). Collectively, these data indicate that the activity and subcellular localization of FOXO3 could be associated with stiff matrix-induced cardiac fibroblast activation and regulation of ECM-related genes.

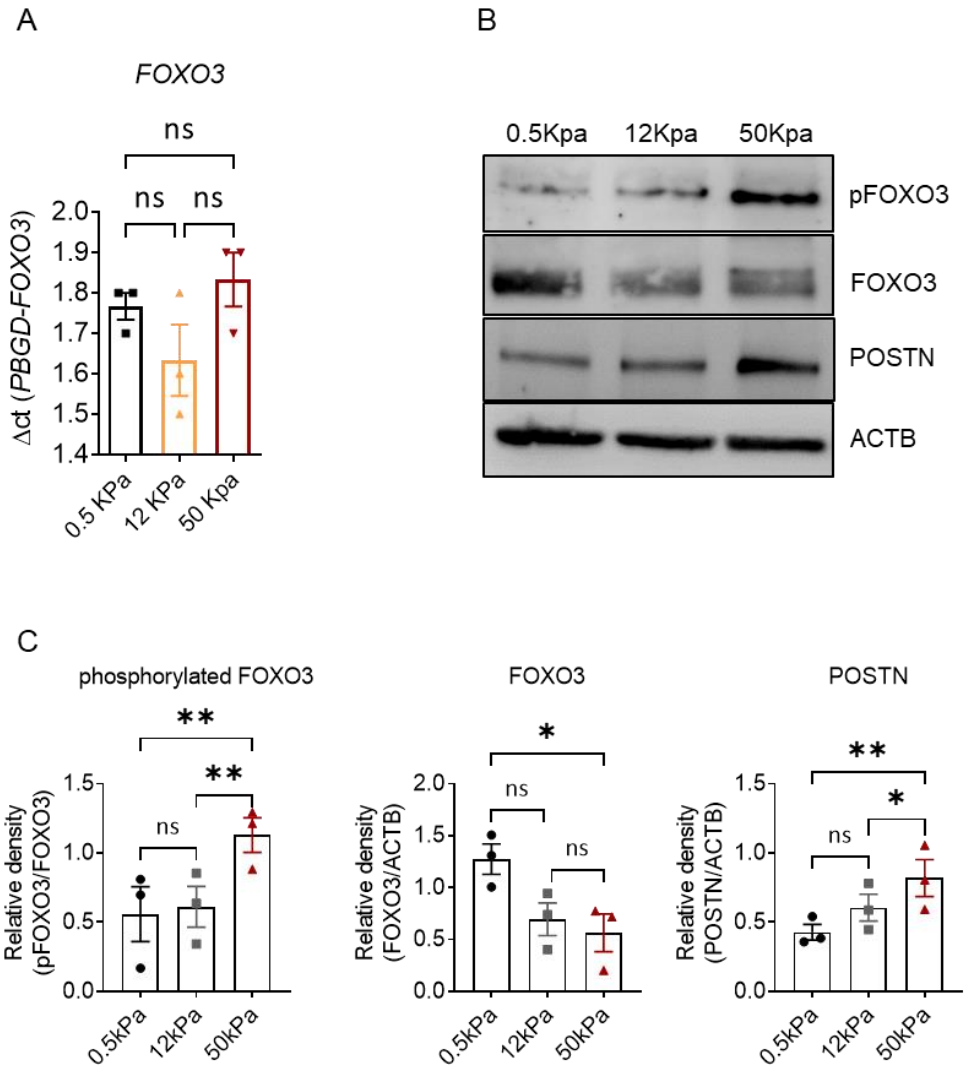

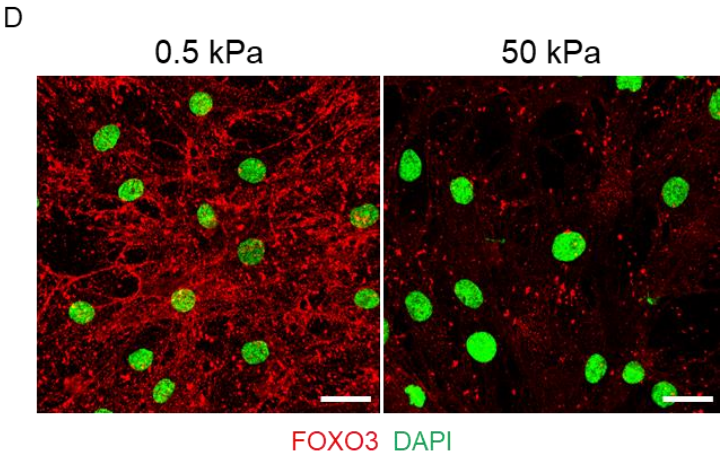

Figure 22. The expression and activity of FOXO3 in the CFs cultured on a stiff matrix. A) qRT-PCR analysis of FOXO3 in CFs cultured on different matrix stiffness at 24h time point. **B)** Representative images of protein levels of pFOXO3, FOXO3 and POSTN determined by western blot analysis. **C)** Corresponding densitometric quantification of the western blots. **D)** Immunofluorescence images indicated decreased FOXO3 expression with increasing stiffness (FOXO3 (red), DAPI (green)). Scale bar = 50 µm. n=3. Error bars indicate the mean with SEM. Data were analyzed using one-way ANOVA with tukey's multiple comparisons test. *p<0.05, **p<0.01, ns=not significant.

4.5 FOXO3 expression is diminished in cardiac fibroblasts (CFs) in response to hypoxia

To explore the regulation of FOXO3 under hypoxic stress, a pathophysiological process involved in the transition of the compensated RV to decompensated RV (139), primary human CFs were cultured under normoxia and hypoxia (1% O_2) for 48h. A decrease in *FOXO3* mRNA expression and correspondingly a significant increase in remodeling markers (*ACTA2*, *POSTN*) and hypoxic markers (*CA9*) were observed under hypoxia compared to normoxia (**Figure 23A**). Similarly, the protein expression of FOXO3 and remodeling markers (aSMA and POSTN) were increased in hypoxia (**Figure 23B**) which were then quantified (**Figure 23C**).

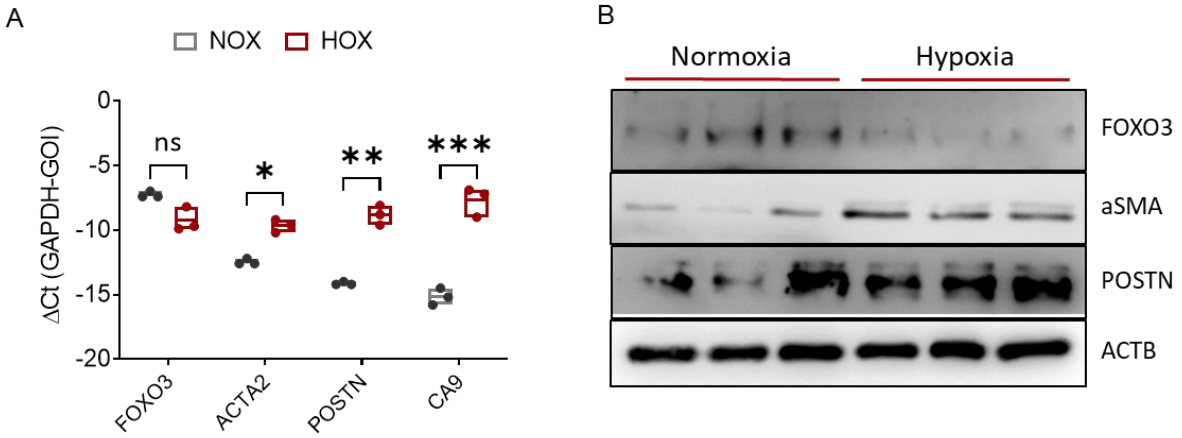

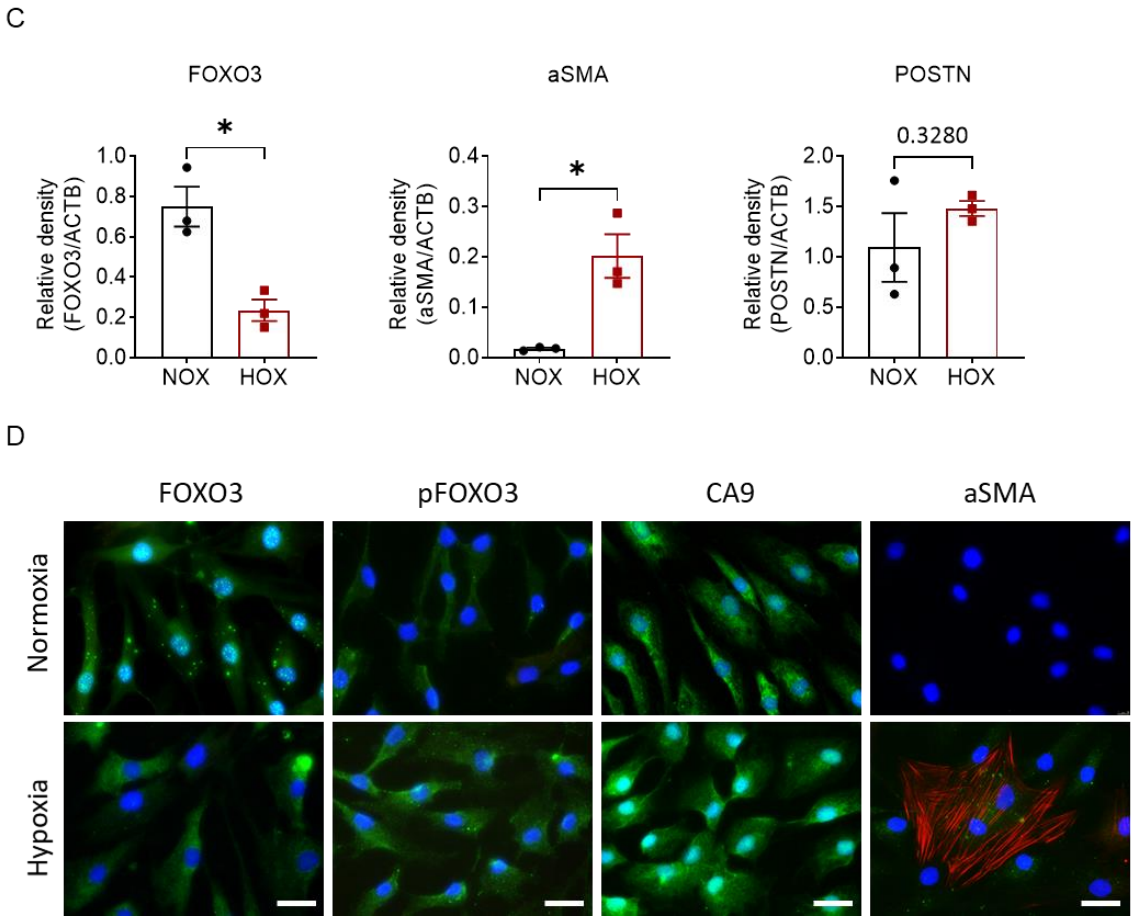

Figure 23. The expression of FOXO3 in response to Hypoxia. Human primary cardiac fibroblasts (HCFs) (n=3) were cultured under hypoxia for 48h, and cell lysates were prepared at indicated timepoint. **A)** mRNA expression of FOXO3, remodeling and hypoxic marker genes in HCFs. Data were analyzed using 2-way ANOVA with Sidak's multiple comparison test. **B)** Western blots analysis of FOXO3, aSMA and POSTN and corresponding **C)** densitometric analysis. Data were analyzed using the Unpaired t-test. **D)** Subcellular localization of FOXO3 (green), pFOXO3 (green), CA9 (green) and aSMA (red), DAPI (blue) in HCFs. Error bars indicate mean with SEM.. *p<0.05, **p<0.01, ***p<0.001, ns=not significant. Scale bar: 50µm.

To further evaluate the subcellular localization, we performed immunofluorescence stainings, indicating the nuclear exclusion of FOXO3 and increased phosphorylation of FOXO3 in HCFs cultured under hypoxia. Hypoxic marker carbonic anhydrase 9 (CA9) and myofibroblast marker alpha-smooth muscle actin (aSMA) staining was increased in hypoxic CFs (**Figure 23D**). These observations confirmed that FOXO3 expression is dysregulated under hypoxia and could promote the fibrogenic response of CFs.

4.6 Knockdown of FOXO3 in human cardiac fibroblasts activates ECM and interferon-associated transcriptional targets

To investigate FOXO3 dependent differential expressed transcriptional targets, we reduced FOXO3 expression using siRNA in cultured human primary cardiac fibroblasts. 48h post siRNA transfection (*siFOXO3*), both mRNA and protein expression of FOXO3 was significantly reduced as compared to the negative control (*siScr*) siRNA treatment (**Figure 24A and 24B**). To identify the direct transcriptional targets and signaling pathways regulated by FOXO3, we extracted RNA from siScr, and siFOXO3 treated cells and performed RNA sequencing. BioAnalyzer assessed RNA integrity (RIN), and RIN values of all samples were over 7. A total of 76 genes were differentially regulated by FOXO3, out of which 34 were up-regulated differentially expressed genes (DEGs) and 42 were down-regulated DEGs analyzed using EdgeR (FDR<0.05; Log2FC>+-0.585, Mean counts>5) (**Figure 24C and 24D**)

To generate insights into the potential biological functions of these DEGs, we performed functional enrichment analyses to identify top enriched transcription factors using TRANSFAC and JASPAR database, top enriched pathways using Reactome pathways database and biological processes using Gene Ontology (GO) database. Interestingly we found enrichment of crucial developmental transcription factors (TFs) such as *KLF4, KLF11* and *MYCN,* also other transcription factors like *IRF9,* which play an important role in anti-viral immunity by driving the cell into an antiviral state (**Figure 25A**)

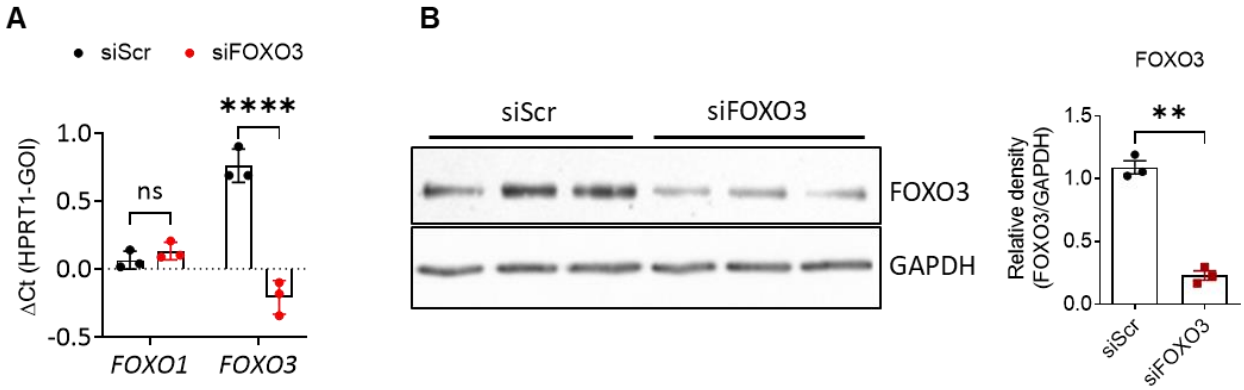

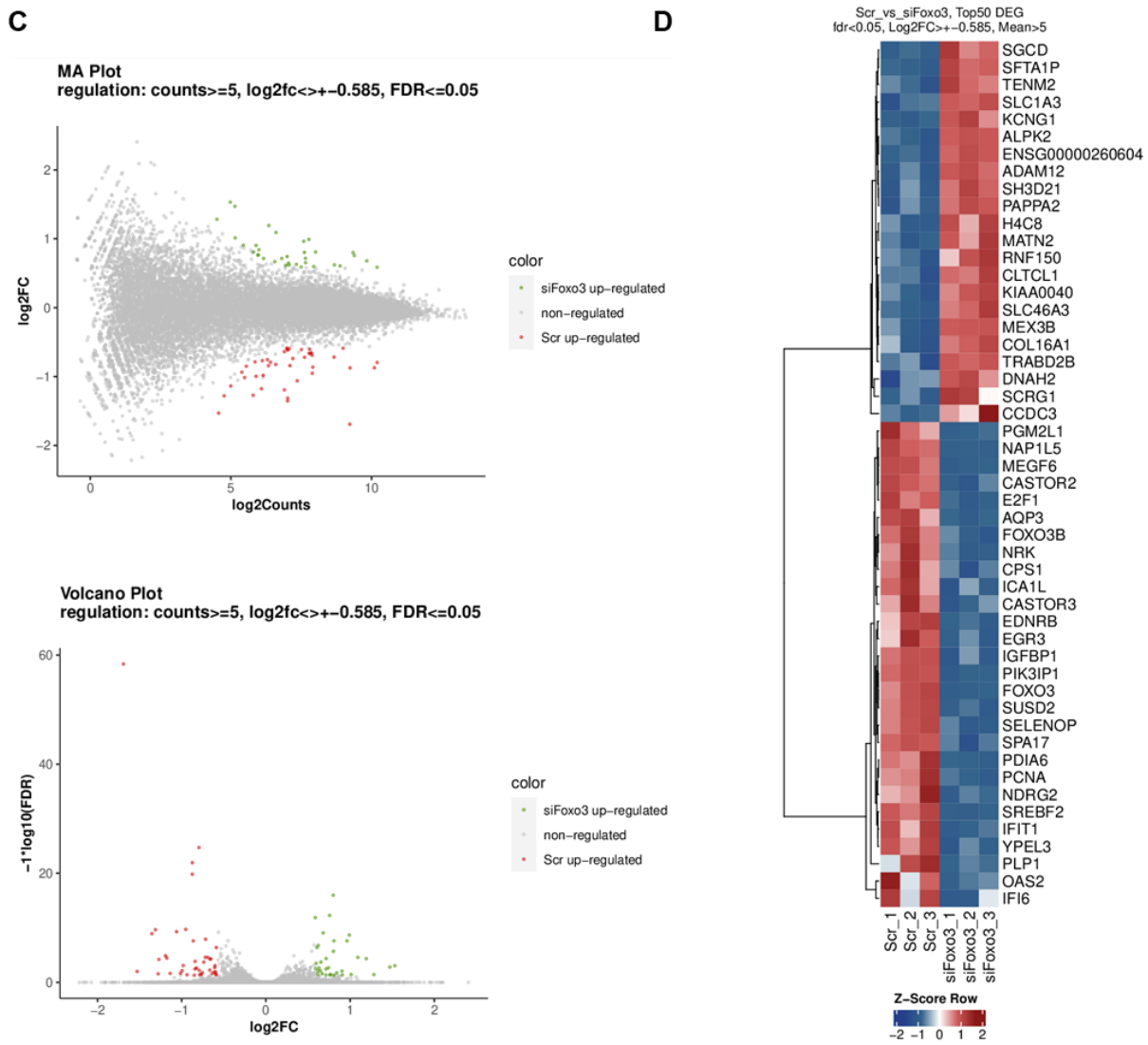

Figure 24. Analysis of differentially expressed genes (DEGs) upon knockdown of FOXO3 in HCFs.
HCFs were transfected with negative control siRNA (*siSCr)* (n=3) or *siFOXO3* (n=3) for 48h followed by RNA and protein extraction. Both **A)** mRNA levels and **B)** protein levels of FOXO3 in siScr and siFOXO3 and their respective quantifications. Data were analyzed using 2-way ANOVA with Sidak's multiple comparison test (A) and paired t-test (B). **C)** The MA plot displays mean normalized counts vs. log2-FC. The volcano plot shows the significance of each expressed gene (−log10 (FDR) values on the y-axis) plotted against the FC (log2 scale) (x-axis). Significant DEGs classified by DESeq2 are highlighted in red or green. **D)** Heatmap representation of the top 50 significant DEGs according to the FDR computed by DESeq2 (FDR<0.05; Log2FC>+-0.585, Mean counts>5). Depicted are row-wise z-scores of DESeq2-normalized counts.

The analysis revealed deregulated genes and pathway networks associated with interferon signaling and ephrin signaling (**Figure 25B**). Furthermore, GO enrichment analysis pointed towards biological processes such as cellular response to the type 1 interferon signaling pathway (**Figure 25C**).

A

Top enriched transcription factors

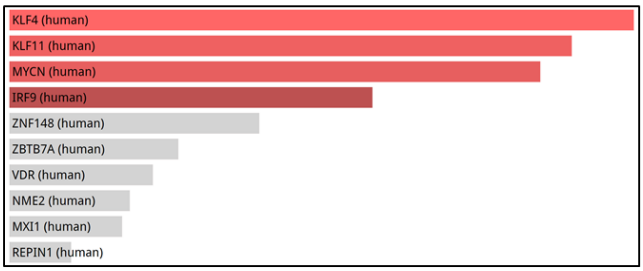

Index	Name	P-value
1	KLF4 (human)	0.009590
2	KLF11 (human)	0.01290
3	MYCN (human)	0.01499
4	IRF9 (human)	0.03341
5	ZNF148 (human)	0.05737
6	ZBTB7A (human)	0.08447
7	VDR (human)	0.09540
8	NME2 (human)	0.1065
9	MXI1 (human)	0.1105
10	REPIN1 (human)	0.1409

B

Top enriched pathways

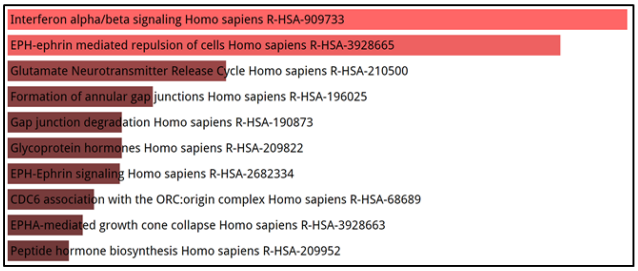

Index	Name	P-value
1	Interferon alpha/beta signaling Homo sapiens R-HSA-909733	0.0001927
2	EPH-ephrin mediated repulsion of cells Homo sapiens R-HSA-3928665	0.0003063
3	Glutamate Neurotransmitter Release Cycle Homo sapiens R-HSA-210500	0.003109
4	Formation of annular gap junctions Homo sapiens R-HSA-196025	0.005165
5	Gap junction degradation Homo sapiens R-HSA-190873	0.006403
6	Glycoprotein hormones Homo sapiens R-HSA-209822	0.006403
7	EPH-Ephrin signaling Homo sapiens R-HSA-2682334	0.006492
8	CDC6 association with the ORC:origin complex Homo sapiens R-HSA-68689	0.007763
9	EPHA-mediated growth cone collapse Homo sapiens R-HSA-3928663	0.008396
10	Peptide hormone biosynthesis Homo sapiens R-HSA-209952	0.009240

C

Top enriched Gene Ontologies (biological process)

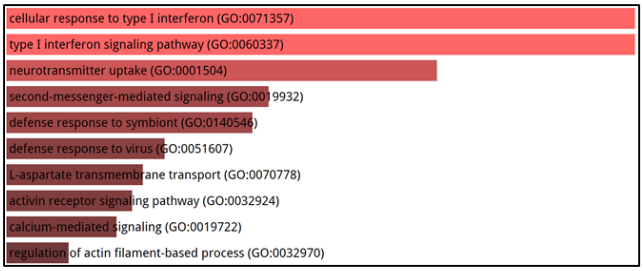

Index	Name	P-value
1	cellular response to type I interferon (GO:0071357)	0.0001500
2	type I interferon signaling pathway (GO:0060337)	0.0001500
3	neurotransmitter uptake (GO:0001504)	0.0003770
4	second-messenger-mediated signaling (GO:0019932)	0.0008251
5	defense response to symbiont (GO:0140546)	0.0008898
6	defense response to virus (GO:0051607)	0.001339
7	L-aspartate transmembrane transport (GO:0070778)	0.001482
8	activin receptor signaling pathway (GO:0032924)	0.001558
9	calcium-mediated signaling (GO:0019722)	0.001675
10	regulation of actin filament-based process (GO:0032970)	0.002093

Figure 25. Histogram of Transcription factors (TFs), Gene Ontology (GO) enrichment and pathway analysis of DEGs. A pathway enrichment analysis was performed on a target list of 285 DEGs. The list of significantly enriched categories is displayed as bar charts with –log2 (P-value) and a corresponding table chart. The enrichment analysis was conducted against the following databases: **A)** top enriched transcription factors (TRANSFAC and JASPAR PWMs). **B)** top enriched pathways (Reactome pathways). **C)** top enriched Gene Ontology (GO) biological process.

4.7 Fibroblast-specific Foxo3 deletion deteriorates RV function in mice subjected to chronic pressure overload

4.7.1 Decreased survival rate

To determine whether Foxo3 depletion in FBs plays a role in the RV failure, we generated FB-specific loss of function by crossing Foxo3$^{fl/fl}$ mice with mice harboring Col1a1 driven Cre recombinase. Adult mutant (Foxo3$^{fl/fl}$; Col1a1^{Cre}, hereafter referred to as Fibroblast specific Foxo3 knockout (fb-Foxo3$^{-/-}$)) and control (Foxo3$^{fl/fl}$ denoted as wildtype (WT)) mice were next subjected to PAB surgery and post five weeks (35 days) of PAB. Mice underwent cardiac MRI and right heart catheterization (RHC) before being sacrificed for anatomical and histological assessments. A group of sham-operated WT and mutant mice served as controls (**Figure 26A**). None of the sham-operated mice died during surgery and throughout the experiment. During the period of the disease development in PAB-operated mice, none of the mice died in the WT group, while two mutant mice subjected to PAB died two days before the termination of the experiment (**Figure 26B**).

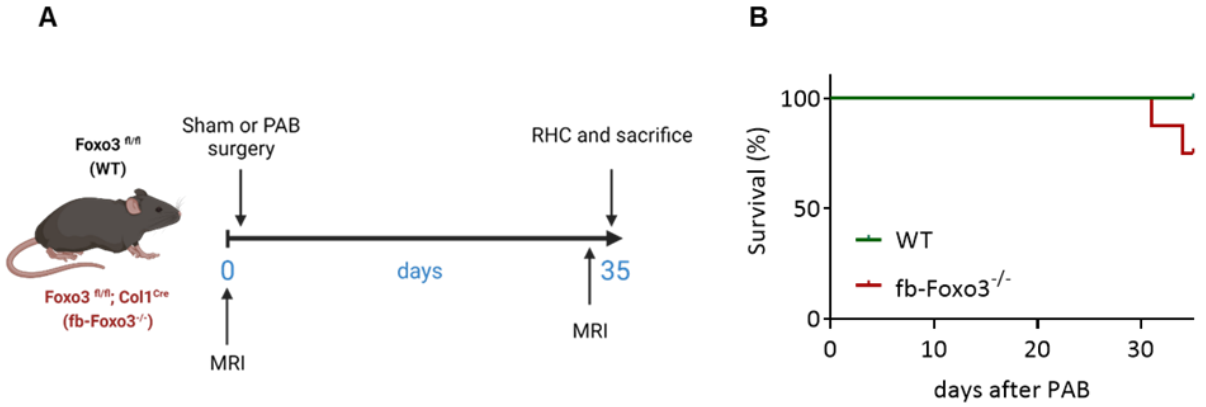

Figure 26. A) Schematic representation of the experimental design. **B)** Kaplan-Meier survival curve demonstrates increased post-pulmonary artery banding (PAB) mortality in mutant mice (fb-Foxo3$^{-/-}$) compared with wildtype (WT) mice.

4.7.2 Reduced RV function assessed by cardiac magnetic resonance (CMR) imaging

Additionally, we assessed cardiac function using non-invasive imaging techniques such as CMR imaging. A representative two-chambered short axis (**Figure 27A**) and four-chambered long axis cine images (**Figure 27B**) at end-systolic and end-diastolic phases in both WT and mutant mice subjected to PAB displayed hypertrophy and a substantial increase in end-systolic and end-diastolic right ventricle internal diameter (RVID) (double-headed arrows in **Figure 27A and Figure 27B**). However, five weeks post-PAB, mutant mice (fb-Foxo3-/-) displayed a severe dilation of RV. As a result, the left ventricle was compressed, reflected in the linear shape of the interventricular septum (IVS).

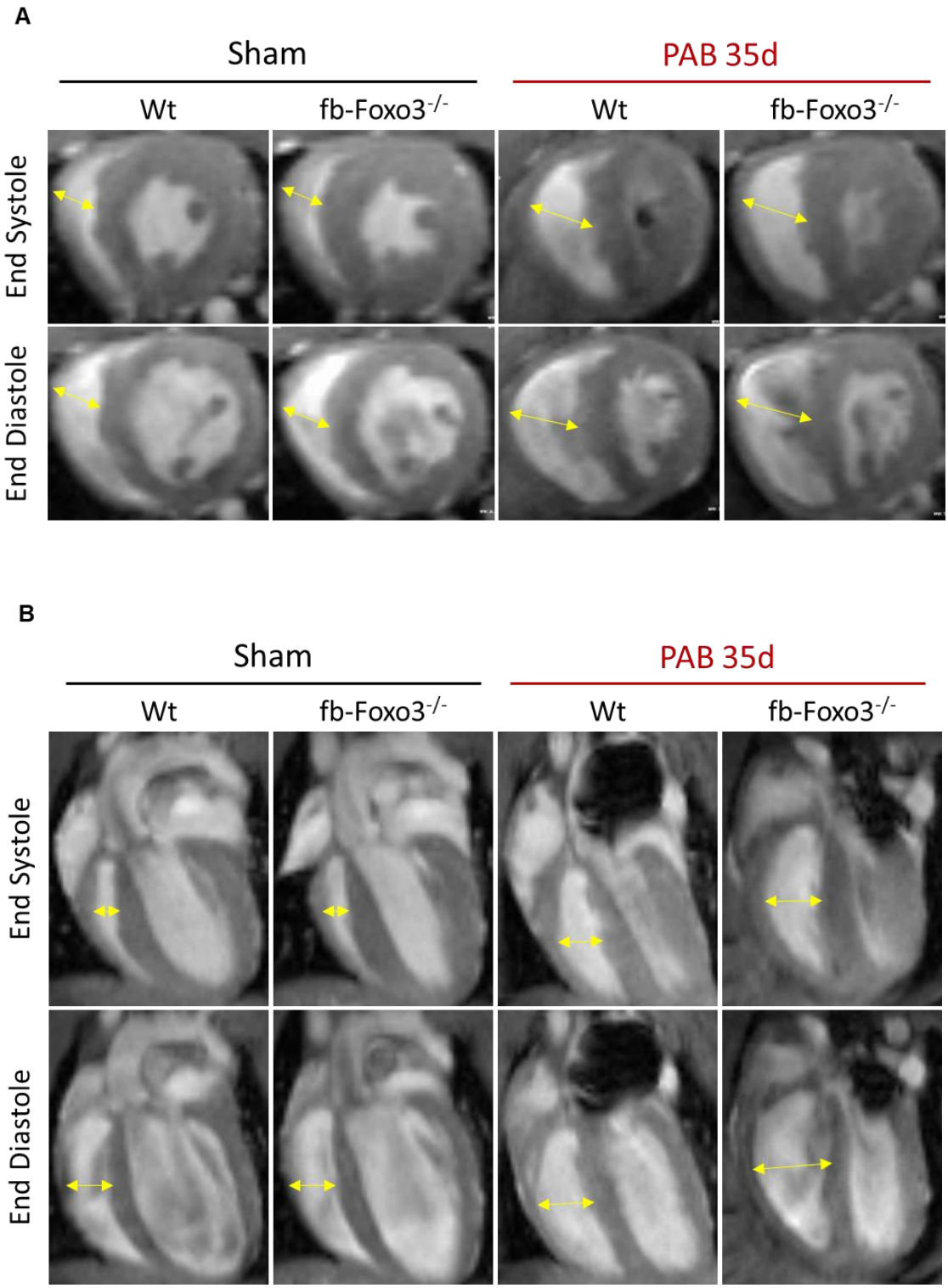

Figure 27. Representative MRI images of a mouse heart at end-diastolic and systolic images for each experimental group are shown in **A)** axial (two-chambered) and **B)** coronal (four-chambered) view at end-diastole and end-systole at 5 weeks after Sham or PAB surgery.

Next, we assessed the cardiac functional parameters by analyzing the images acquired from CMR imaging. As hypothesized, the analysis revealed RV dysfunction in WT mice that underwent PAB surgery which is reflected by a significant decrease in cardiac index (CI) and

Ejection fraction (RVEF). Simultaneously, the RV end-diastolic volume to LV end-diastolic volume ratio (RVEDV/LVEDV) and RV end-diastolic mass to RV end-diastolic volume (RVEDM/RVEDV) ratio is significantly increased in WT on day 35 post-PAB. However, interestingly, mutant mice (fb-Foxo3-/-) that underwent PAB surgery exhibited much more severe RV dysfunction compared to WT mice at day 35 post-PAB, which was reflected by the significant decrease in the CI, stroke volume index (RVSVI) and RVEF, and a significant increase in RVEDV/LVEDV. In conjunction, the mutant mice group displayed severe RV dysfunction compared to the WT group upon PAB (**Figure 28A-28E**).

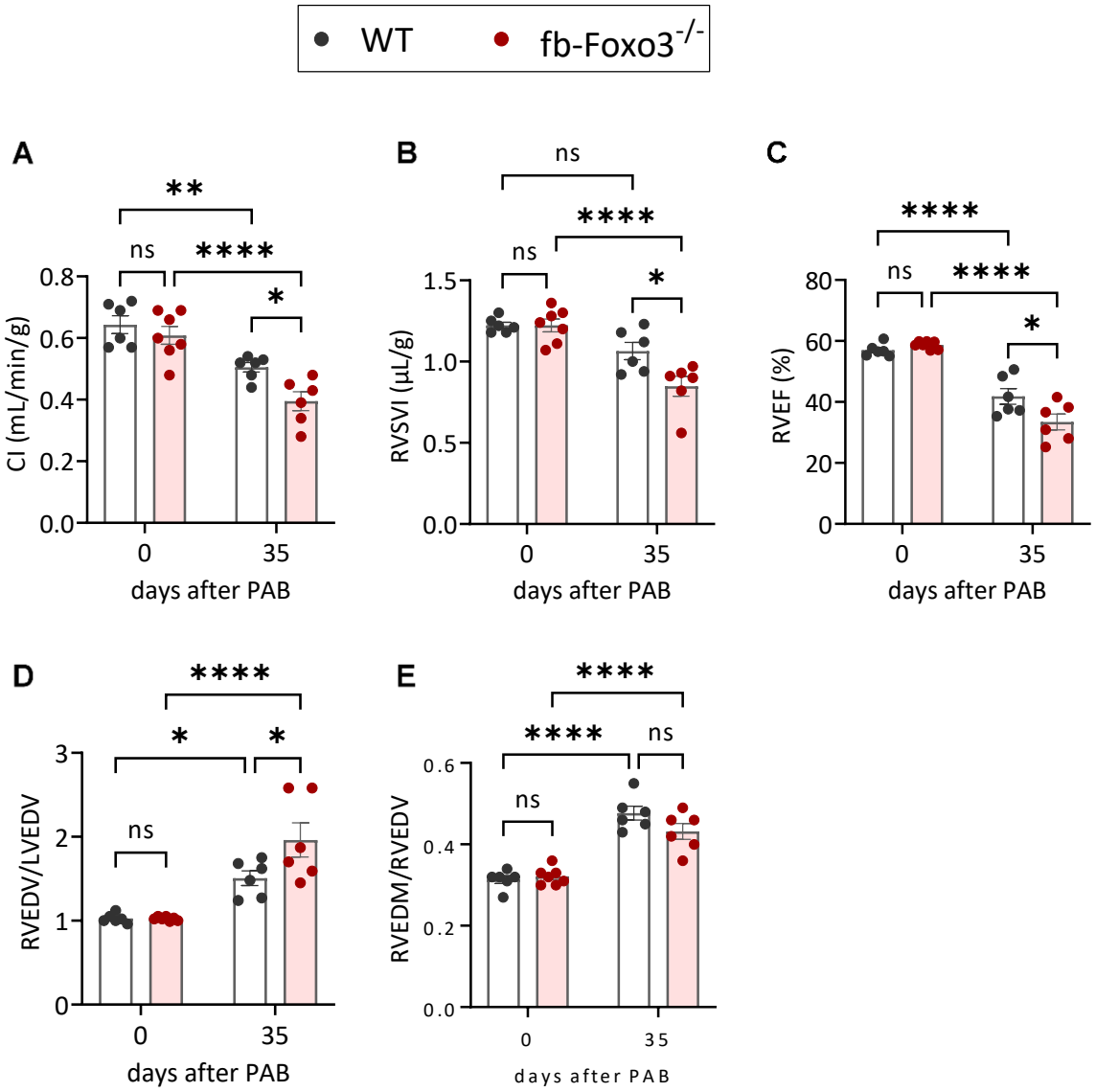

Figure 28. Cardiac functional analysis of Fibroblast specific Foxo3 knockout upon PAB.
A-E) Cardiac index (CI), RV stroke volume index (RVSVI), RV ejection fraction (RVEF), RV end-diastolic volume to LV end-diastolic volume ratio (RVEDV/LVEDV) and RV end-diastolic mass to RV end-diastolic volume (RVEDM/RVEDV) were measured in WT (Sham (n=6) and PAB (n=6)) and mutant mice (Sham (n=7) and PAB (n=6)) both at baseline (day0) and day 34 post PAB. Error bars indicate the mean with SEM. Data were analyzed using two-way ANOVA with tukey's multiple comparisons test. *p<0.05, **p<0.01, ****p<0.0001, ns=not significant.

4.7.3 Altered hemodynamic response in mutant mice

Before sacrificing the mice at day 35 post-PAB, invasive right heart catheterization (RHC) and anatomical measurements were performed to measure the systemic and pulmonary hemodynamics and the hypertrophic growth of RV, respectively. All PAB-operated mice developed severe right ventricular hypertrophy as evident with significantly increased Fulton index (RV/LV+S) and RV mass to tibia length ratio (RV/tibia length); however, the hypertrophy was more pronounced in the mutant mice subjected to PAB compared to WT littermates. Similarly, PAB-operated WT mice displayed increased right ventricular end-diastolic pressure (RVEDP). However, PAB-operated mutant had significantly higher values of RVEDP compared to WT littermates, while mutant PAB mice had significantly higher RVEDP values compared to WT littermates. PAB surgery resulted in a similar degree of increased RVSP in both WT and mutant mice.

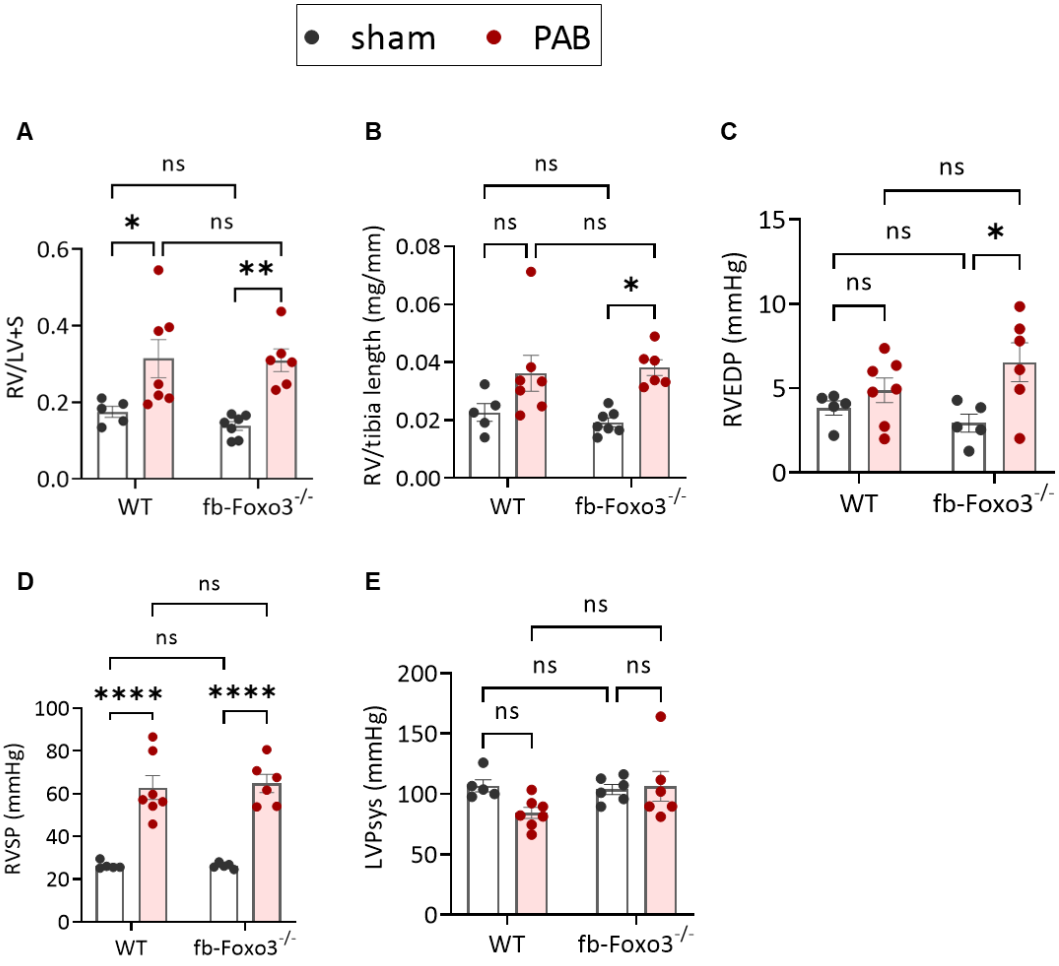

Figure 29. Hemodynamic and anatomical parameters of Fibroblast specific Foxo3 knockout upon PAB. A-E) Fulton index (RV/LV+S), RV/tibia length, Right ventricular end-diastolic pressure (RVEDP, mmHg), Right ventricular systolic pressure (RVSP, mmHg), Left ventricular systolic blood pressure (LVSP, mmHg) was measured in WT (Sham (n=5) and PAB (n=7)) and mutant mice (Sham (n=7) and PAB (n=6)) at day 35 post-PAB. Error bars indicate the mean with SEM. Data were analyzed using two-way ANOVA with tukey's multiple comparisons test. *p<0.05, **p<0.01, ****p<0.0001, ns=not significant.

On day 35 post sham or PAB surgery, mice from all groups had no significant changes in left ventricular systolic pressure (LVSP), regardless of their genetic background or treatment (**Figure 29A-29E**). Together these results demonstrate that loss of Foxo3 in Col1a1 lineage CFs leads to reduced cardiac function and increased cardiac hypertrophy after PAB-induced pressure overload injury.

4.7.4 Immunofluorescence and histopathological assessment of cardiomyocyte hypertrophy, capillary density and fibrosis in RV

Immunofluorescence staining on transversal slices of right ventricular cardiomyocytes stained with wheat gram agglutinin (WGA-FITC) (green), which specifically stains the cell membrane of all cardiac cell types, was employed to measure the CSA of RV cardiomyocytes and Isolectin b4 (IB4) (red) which stains explicitly the cell membrane of endothelial cells to quantify the capillary density in the RV. As seen in (**Figure 30A**), the individual cardiomyocytes are much more prominent in size in the PAB group on day 35. However, quantitatively, the CSA in mutant mice was markedly increased, with no capillary density change compared to Wt PAB mice (**Figure 30B-30C**).

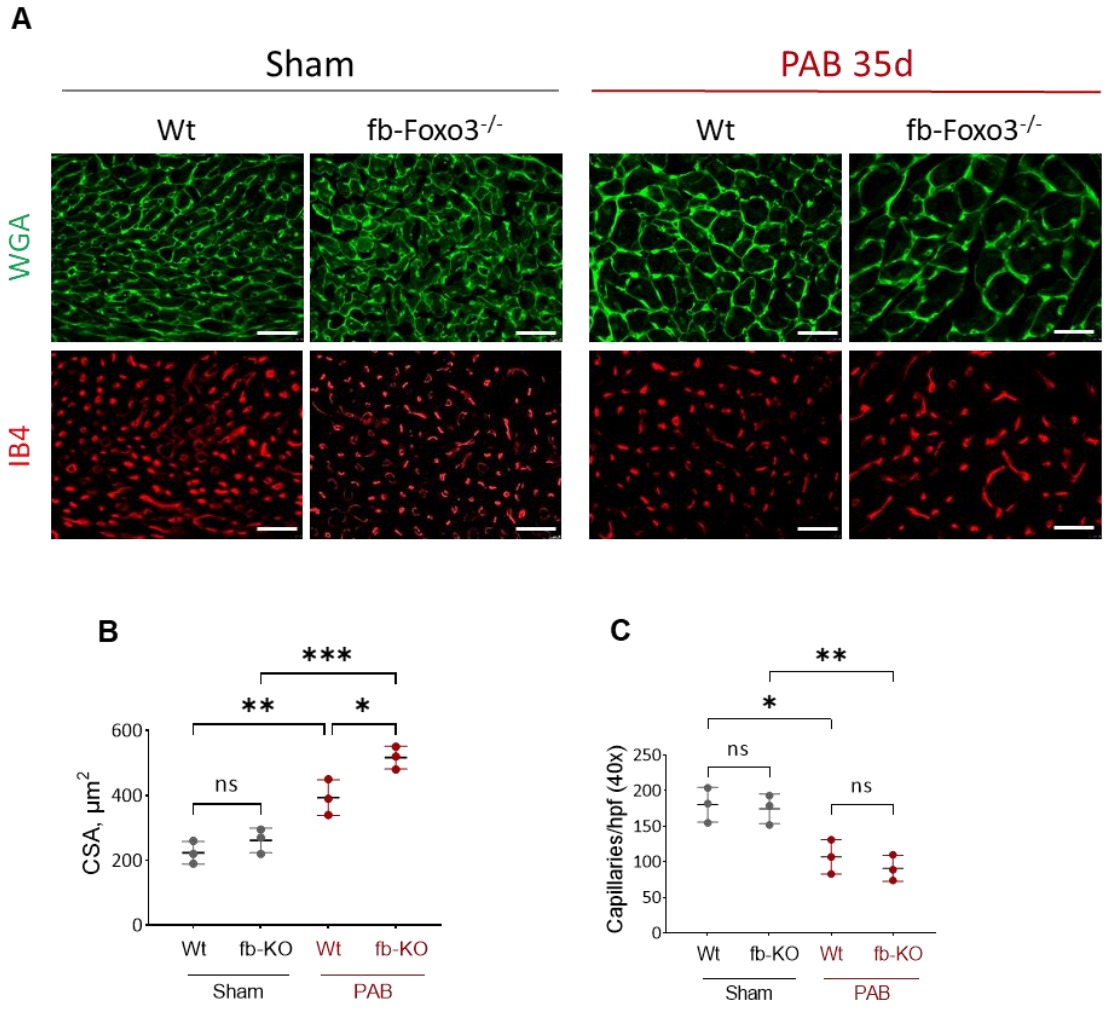

Figure 30. A) Representative images of RV stained with Wheat germ agglutinin (WGA) (green) or Isolectin B4 (IB4) (red) from Wt and mutant mice subjected to either sham or PAB. **B–C)** Quantitative analyses of cardiomyocyte cross-sectional area and capillary density in RVs from WT (Sham (n=3) and PAB (n=3)) and mutant mice (Sham (n=3) and PAB (n=3)) at day 35 post-PAB. Error bars indicate the mean with SEM. Data were analyzed using one-way ANOVA with tukey's multiple comparisons test. *p<0.05, **p<0.01, ***p<0.001, ns=not significant.

Histological examination of right ventricular tissues with Picric Sirius red staining revealed that mice upon PAB developed a marked increase of RV myocardial fibrosis compared to sham mice (**Figure 31A**). However, at least histologically, no significant changes were observed in myocardial fibrosis between Wt and mutant mice upon PAB. (**Figure 31B**).

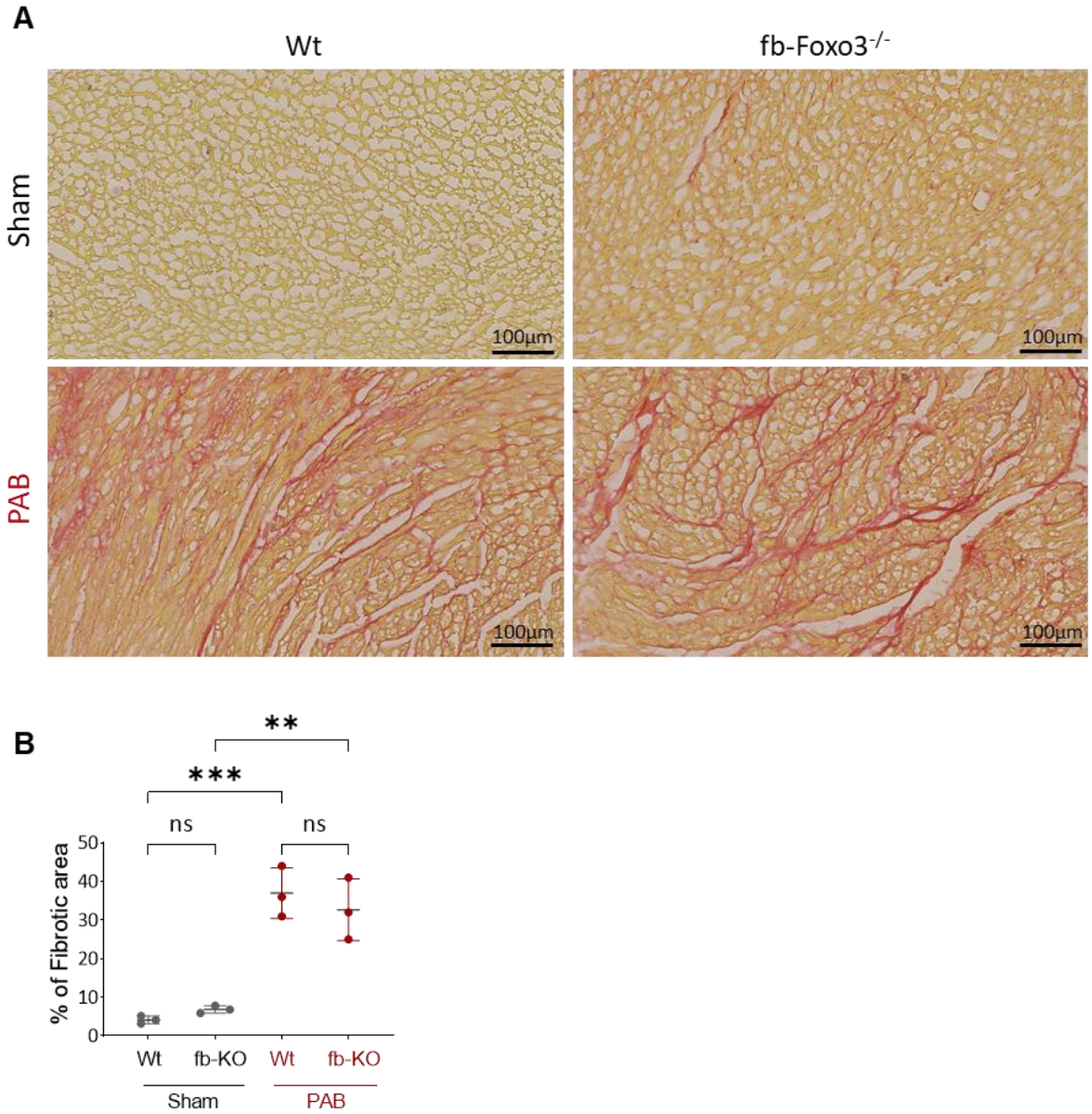

Figure 31. A) Representative images of RV stained with Picric sirious red from Wt and mutant mice subjected to either sham or PAB. **B)** Quantitative analysis of the percentage of fibrotic area in RVs from WT (Sham (n=3) and PAB (n=3)) and mutant mice (Sham (n=3) and PAB (n=3)) at day 35 post-PAB. Error bars indicate the mean with SEM. Data were analyzed using one-way ANOVA with tukey's multiple comparisons test. **p<0.01, ***p<0.001, ns=not significant. Scale bar:100µm.

4.7.5 mRNA expression profiling of maladaptive remodeling genes

Next, we examined if the known marker genes induced during maladaptive remodeling in RV upon PAB, such as hypertrophic markers genes (*Nppa, Nppb*), fibrotic marker genes (*Postn, Col3a1*), cell contractility genes (*Myh6, Myh7, Acta2, Actc1*), cell cycle genes (*Ccnd1*). The genes induced during maladaptive remodeling presented heterogeneous expression levels between different animals, possibly due to different cell compositions of the tissue samples and heterogeneity in the constriction of the pulmonary artery. *Nppa* was significantly upregulated in both genotypes of the PAB group. However, *Nppb, Myh7 and Postn* were specifically upregulated in mutant mice subjected to PAB, indicating more pronounced pathological hypertrophy in those mice (**Figure 32**).

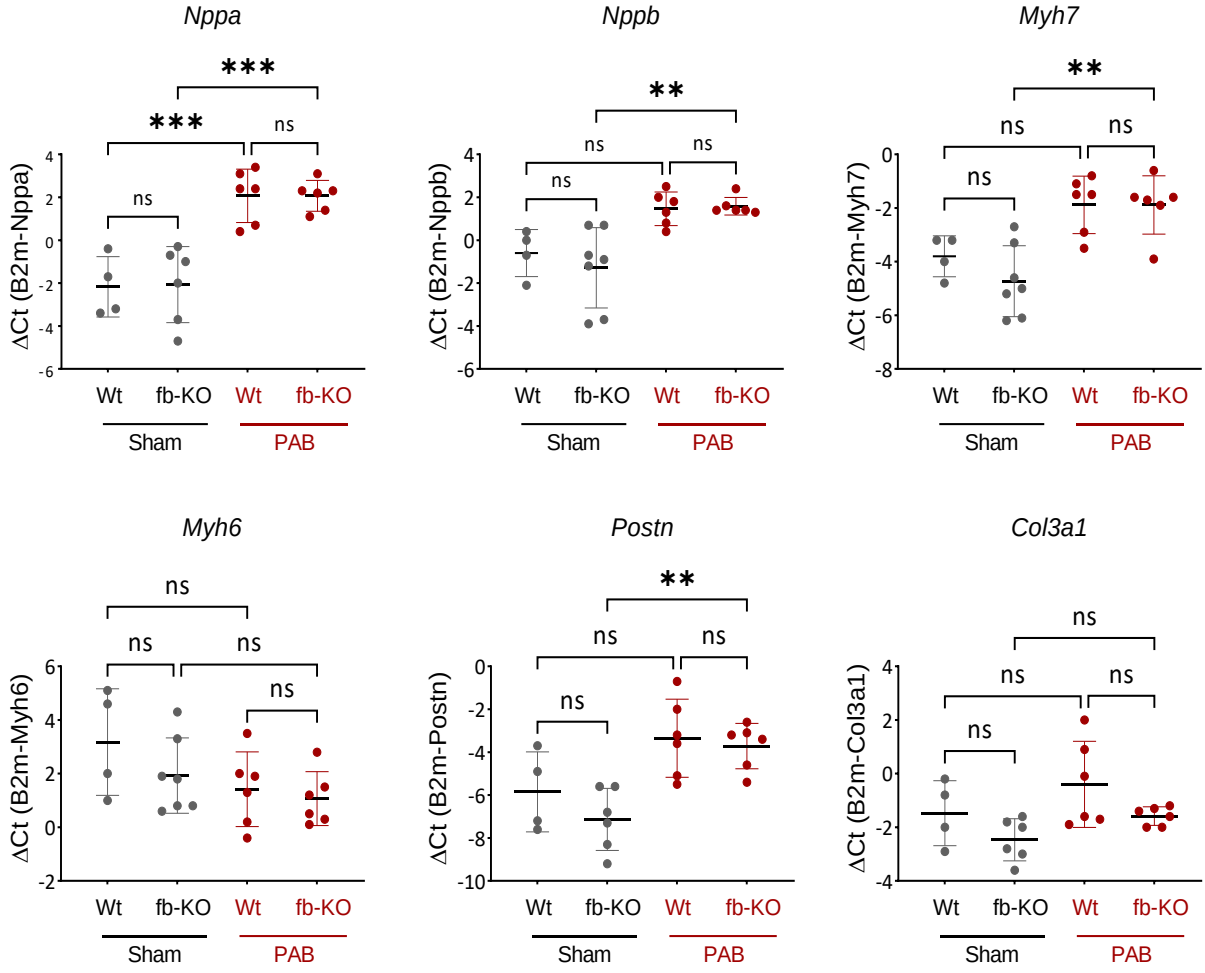

Figure 32. Relative mRNA expression of remodeling and heart failure marker genes in RVs from WT (Sham (n=3) and PAB (n=3)) and mutant mice (fb-KO) (Sham (n=3) and PAB (n=3)) at day 35 post PAB. Error bars indicate the mean with SEM. Data were analyzed using one-way ANOVA with tukey's multiple comparisons test. *p<0.05, **p<0.01, ***p<0.001, ns=not significant.

4.7.6 Comparison of transcriptomic profiles in the RV of WT-Sham and Fb-FoxO3-Sham mice

To determine fibroblast-specific FoxO3 deletion-mediated alteration of gene expression in RV of sham mice, RNA-seq was used to analyze the transcriptome of RV tissue from WT-Sham and FB-FoxO3 mice. The volcano plot shows the significance of each expressed gene (−log10 (FDR) values on the y-axis) plotted against the FC (log2 scale) (x-axis). Significant DEGs classified by DESeq2 are highlighted in red or green between WT-Sham and FB-FoxO3-Sham groups (**Figure 33A**). A total of 255 DEGs were obtained between the groups, and a heatmap with the top 50 most significantly DEGs (up or down) for this contrast (sorted by smallest padj) (**Figure 33B**). Compared with WT-Sham, upregulated genes in the FB-FoxO3 group were associated with innate immune responses, such as 'defense response to virus,' 'cellular response to interferon-alpha and gamma,' 'positive regulation of type I interferon-mediated signaling pathway' (**Figure 33C**). These results indicate that Foxo3 might be involved in regulating innate immune responses, such as interferon-mediated signaling pathways in the RV of mice.

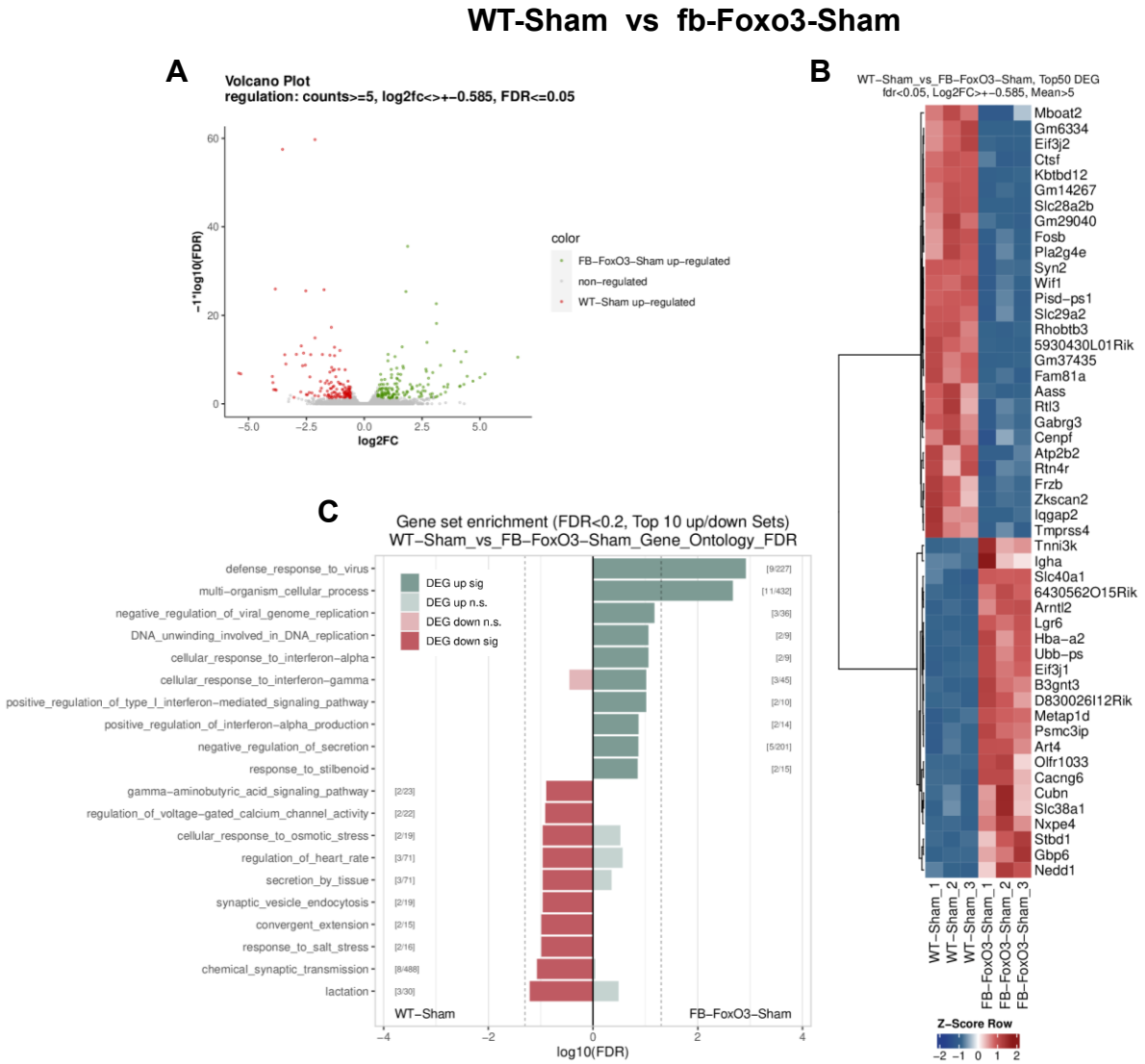

Figure 33. Transcriptomic profiling in the RV of FB-FoxO3 mutant mice. **A)** The volcano plot shows that the significant DEGs classified by DESeq2 are highlighted in red or green. **B)** A heatmap shows the top 50 DEGs between WT-Sham (n=3) and Fb-FoxO3-Sham (n=3) mice. **C)** GSEA analysis of the DEGs between WT-Sham and Fb-FoxO3-Sham.

4.7.7 Comparison of transcriptomic profiles in the RV of WT-Sham and WT-PAB mice

To determine PAB-mediated alteration of gene expression in RV of WT mice, RNA-seq was used to analyze the transcriptome of RV tissue from WT-Sham and WT-PAB mice. The volcano plot shows the significance of each expressed gene (−log10 (FDR) values on the y-axis) plotted against the FC (log2 scale) (x-axis). Significant DEGs classified by DESeq2 are highlighted in red or green between WT-Sham and WT-PAB groups (**Figure 34A**). A total of 1270 DEGs were obtained between the groups, and a heatmap with the top 50 most significantly DEGs (up or down) for this contrast (sorted by smallest padj) (**Figure 34B**). Compared with WT-Sham, upregulated genes in the Wt-PAB group were associated with ECM-related terms, such as ‘Extra cellular matrix organization,’ ‘Integrin signaling,’ ‘ECM

synthesis and degradation,' 'Immune system.' Compared with WT-Sham, downregulated genes in the WT-PAB group were associated with G-protein coupled adrenergic receptors, such as 'Adrenoreceptors' (**Figure 34C**). These results indicate that PAB in WT mice induces ECM reorganization or remodeling, leading to a stiff matrix in the RV, and the changes in ECM can negatively impact the sympathetic response ('flight-or-fight response'), resulting in abnormal heart rate and energy demand responses.

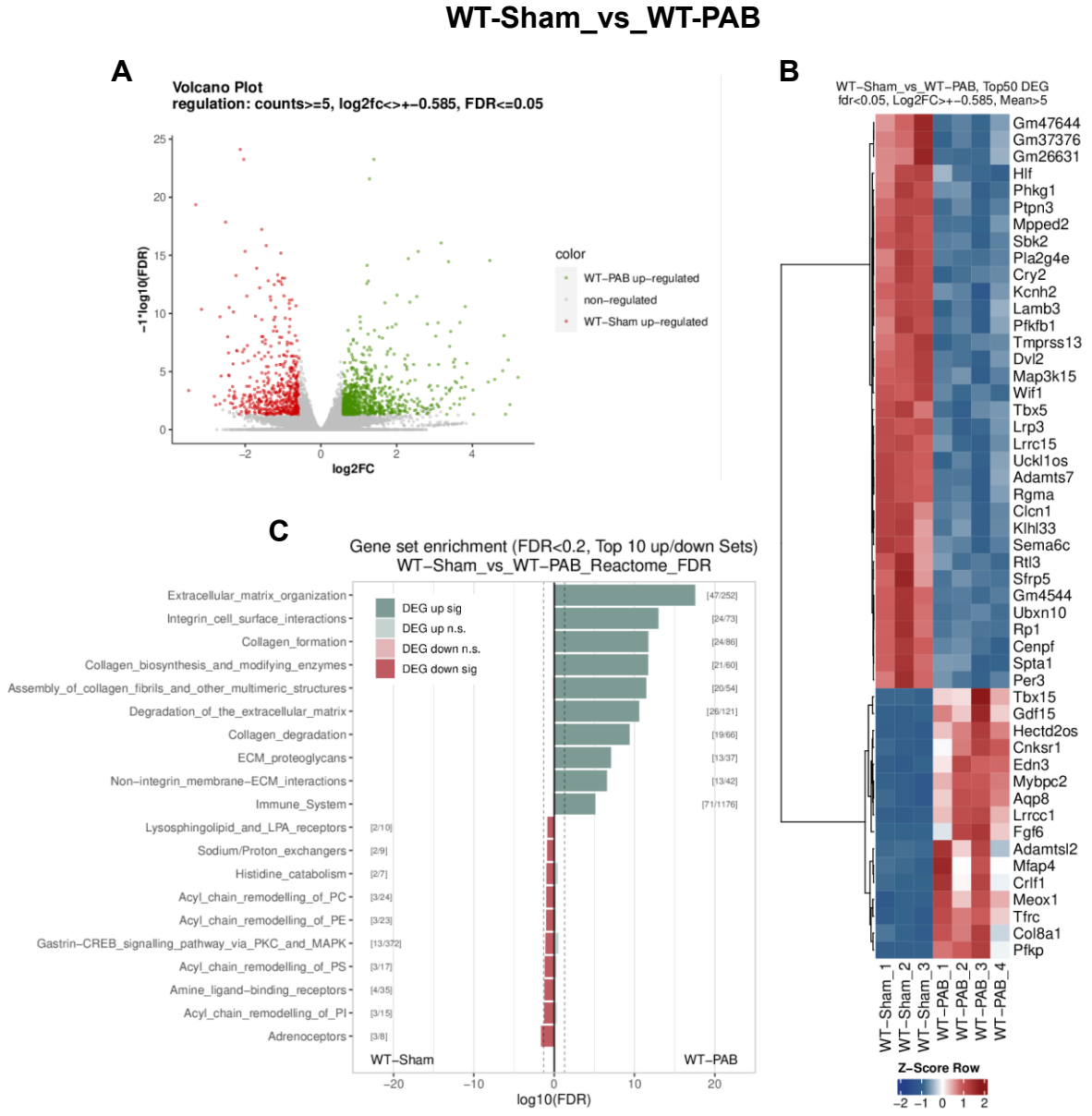

Figure 34. Transcriptomic profiling in the RV of WT-PAB mice. **A)** The volcano plot shows that the significant DEGs classified by DESeq2 are highlighted in red or green. **B)** A heatmap shows the top 50 DEGs between WT-Sham (n=3) and WT-PAB (n=4) mice. **C)** GSEA analysis of the DEGs between WT-Sham and WT-PAB mice.

4.7.8 Comparison of transcriptomic profiles in the RV of FB-FoxO3-Sham and FB-FoxO3-PAB mice

To determine the transcriptional response of FB-FoxO3 upon subjecting them to PAB, RNA-seq was used to analyze the transcriptome of RV tissue from FB-FoxO3-Sham and FB-FoxO3-PAB mice. The volcano plot shows the significance of each expressed gene (−log10 (FDR) values on the y-axis) plotted against the FC (log2 scale) (x-axis). Significant DEGs classified by DESeq2 are highlighted in red or green between WT-Sham and WT-PAB groups (**Figure 35A**). A total of 530 DEGs were obtained between the groups, and a heatmap with the top 50 most significantly DEGs (up or down) for this contrast (sorted by smallest padj) (**Figure 35B**).

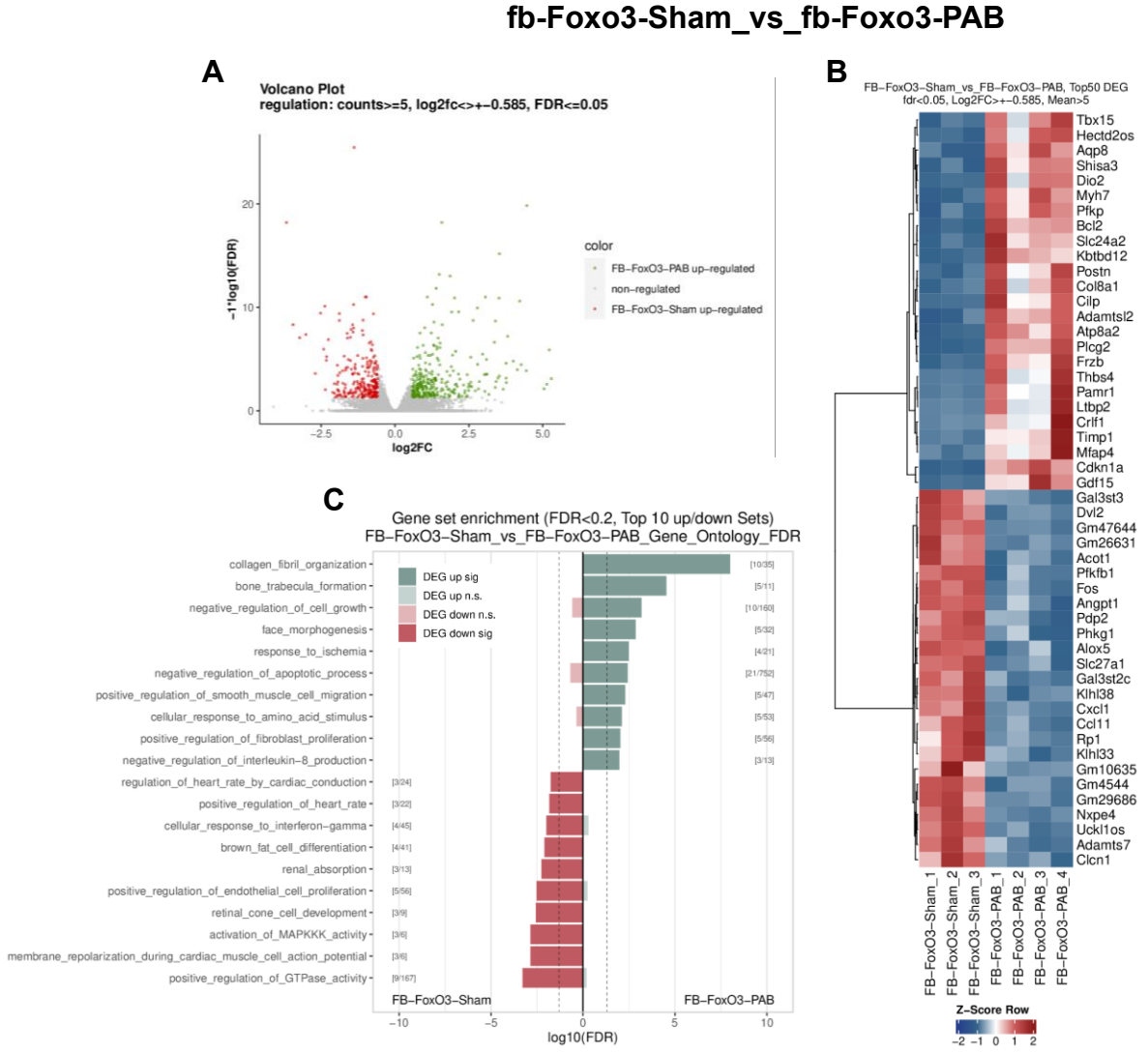

Figure 35. Transcriptomic profiling in the RV of FB-FoxO3 mice upon PAB. **A)** The volcano plot shows that the significant DEGs classified by DESeq2 are highlighted in red or green. **B)** A heatmap shows the top 50 DEGs between FB-FoxO3-Sham (n=3) and FB-FoxO3-PAB (n=4) mice. **C)** GSEA analysis of the DEGs between FB-FoxO3-Sham and FB-FoxO3-PAB mice.

Compared with FB-FoxO3-Sham, upregulated genes in the FB-FoxO3-PAB group were associated with pro-proliferative and anti-apoptotic phenotypes, such as ‘negative regulation of the apoptotic process,’ ‘positive regulation of smooth muscle cell migration, ‘positive regulation of fibroblast proliferation.’ Compared with FB-FoxO3-Sham, downregulated genes in the FB-FoxO3-PAB group were associated with the process that activates or increases the activity of a GTPase, cardiac muscle cell plasma membrane potential changes and positive regulation of endothelial cell proliferation (**Figure 35C**). These results indicate that PAB in FB-FoxO3 mice induces hyperproliferation of fibroblasts and coronary artery remodeling, leading to myocardial and periarteriolar fibrosis. Down regulation of endothelial cell proliferation also hints toward blunted angiogenic and cardiac conduction processes.

4.7.9 Comparison of transcriptomic profiles in the RV of WT-PAB and FB-FoxO3-PAB mice

As it is evident from the previous sections that the cardiac function of FB-FoxO3 is much worse than WT mice subjected to PAB, RNA-seq was used to analyze the transcriptome of RV tissue from FB-FoxO3-PAB and WT-PAB mice. The volcano plot shows the significance of each expressed gene (−log10 (FDR) values on the y-axis) plotted against the FC (log2 scale) (x-axis). Significant DEGs classified by DESeq2 are highlighted in red or green between WT-Sham and WT-PAB groups (**Figure 36A**).

A total of 254 DEGs were obtained between the groups, and a heatmap with the top 50 most significantly DEGs (up or down) for this contrast (sorted by smallest padj) (**Figure 36B**). Compared with WT-PAB, in the FB-FoxO3-PAB group, there were few gene enrichment terms. Compared with WT-PAB, downregulated genes in the FB-FoxO3-PAB group were associated with ‘complement cascade,’ ‘Innate immunity,’ and ‘Toll-like receptor signaling’ (**Figure 36C**). These results indicate that PAB in FB-FoxO3 mice blunts the innate immune signaling by dysregulating the Toll-like receptor signaling pathway and complement cascade system.

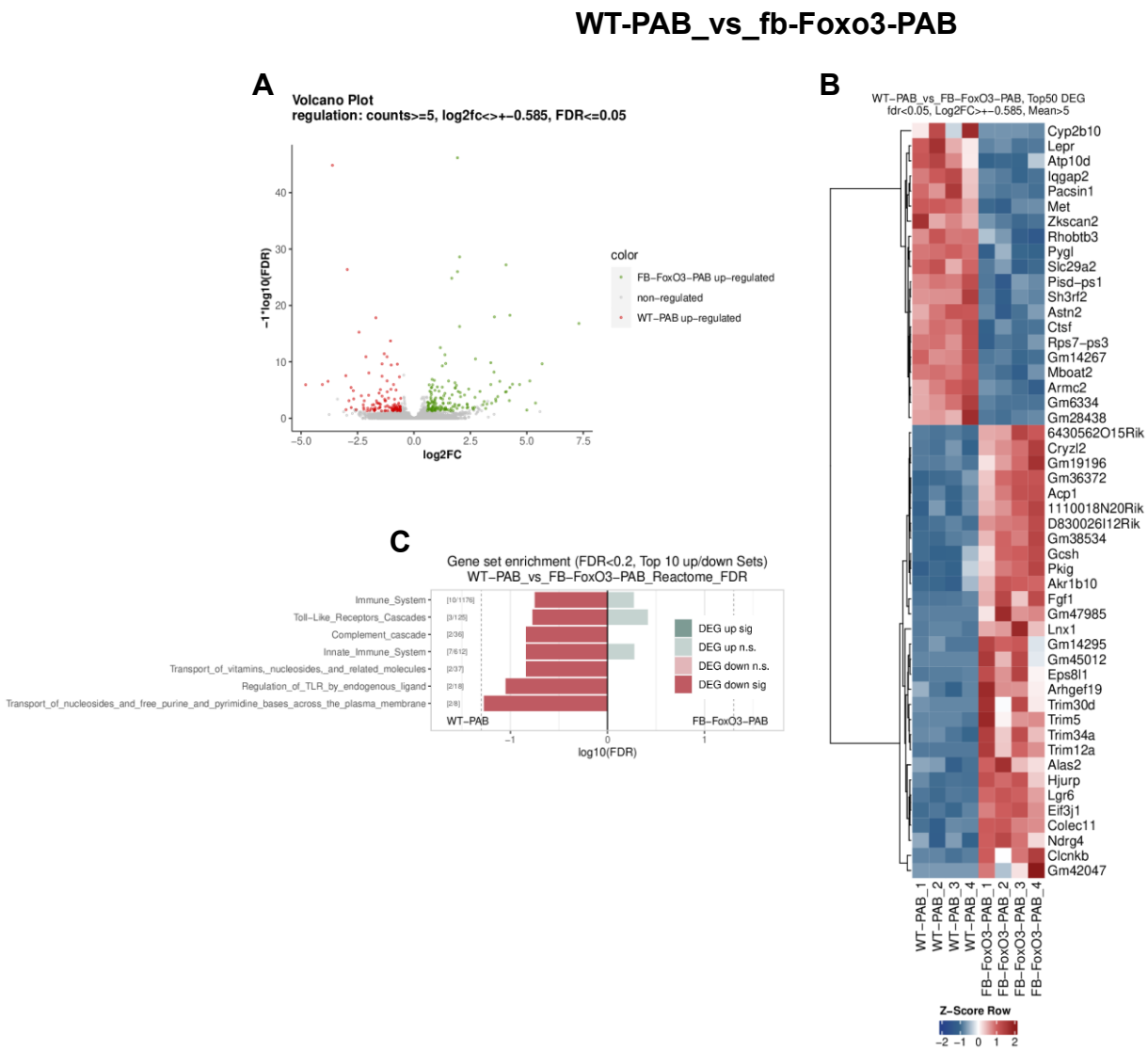

Figure 36. Transcriptomic profiling in the RV of FB-FoxO3 mice upon PAB compared to WT mice upon PAB. **A)** The volcano plot shows that the significant DEGs classified by DESeq2 are highlighted in red or green. **B)** A heatmap shows top 50 DEGs between WT-PAB (n=3) and FB-FoxO3-PAB (n=4) mice. **C)** GSEA analysis of the DEGs between WT-PAB and FB-FoxO3-PAB mice.

4.8 Pharmacological activation of Foxo3 improves established RV dysfunction in animal models

With the consistent correlation of FOXO3 downregulation to declined RV function established in the previous sections of the results, we sought to determine whether pharmacological activation of FOXO3 could improve RV function *in vivo*. In this study, we used the antipsychotic drug trifluoperazine (TFP), which was repurposed for cancer treatment due to its anti-tumor properties in various preclinical cancer models (140-142). Especially, TFP was reported to inhibit the AKT/forkhead box protein O3 (FOXO3) axis and interfere with DNA repair mechanisms and autophagy (140-142), all of which are implicated in the abnormal behavior of

cardiac cells in the decompensated RV. Recently, our Canadian collaborators also showed that TFP exerts anti-survival and anti-proliferative effects on PAH-PASMCs, and its administration improved established PAH in two preclinical models (143)(**Figure 37**). However, whether TFP has a beneficial effect on diastolic function and contractile properties of RV remains unknown. To address this question, together with our collaborators, we assessed the effects of TFP in two well-established animal models mimicking the RV dysfunction due to progressive vascular remodeling (143).

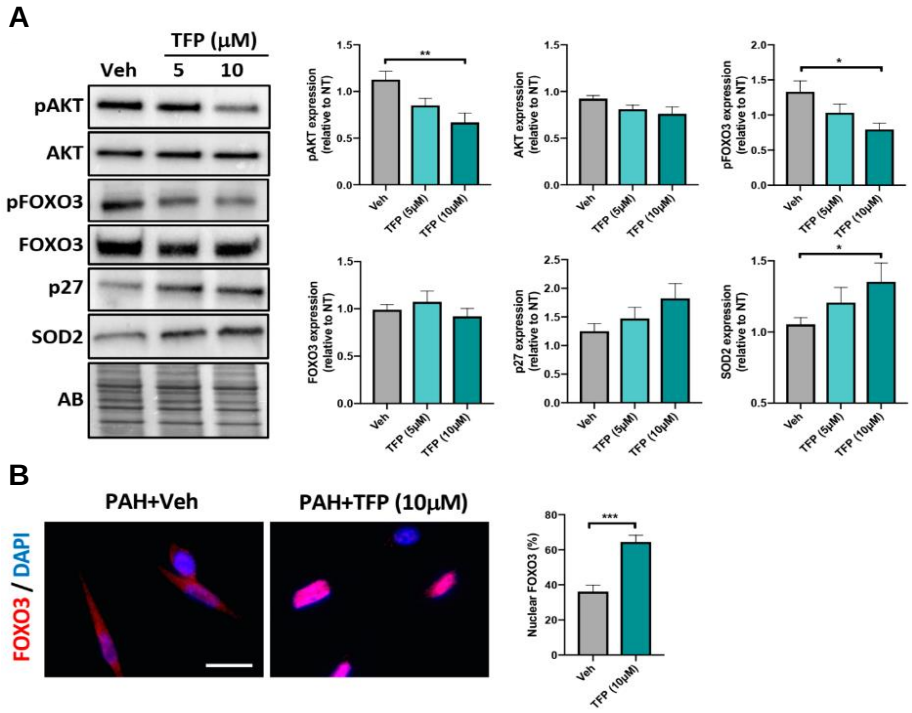

Figure 37. Trifluoperazine (TFP) inhibits AKT activity, leading to nuclear translocation of FOXO3 in PAH-PASMCs (n=9). (A) Representative Western blots and corresponding densitometric analyses of p(Ser473)-AKT, AKT, p(Ser253)-FOXO3, FOXO3, p27 and SOD2 in PAH-PASMCs exposed or not to TFP for 24 h. **(B)** Representative immunofluorescence images for subcellular localization of FOXO3 in PAH-PASMCs exposed to TFP (10 µM) or its vehicle for 24 h. Quantification of the percentage of cells exhibiting nuclear expression of FOXO3 is shown. Protein expression was normalized to Amido black (AB). * $p < 0.05$; ** $p < 0.01$ and *** $p < 0.001$. Scale bars: 20 µm. *Reused under Creative Commons Attribution License from reference (143)*.

4.8.1 Effects of trifluoperazine (TFP) treatment on Monocrotaline (MCT) and Sugen hypoxia-induced RV decompensation in rats

We first employed an MCT animal model that mimics the RV dysfunction in PAH patients. To accomplish the purpose, rats received a single injection of monocrotaline. Two weeks after MCT injection, rats were randomized into two groups that received either TFP or vehicle (**Figure 38A**). Administration of TFP significantly reduced end-diastolic pressure (EDP, mmHg) and improved arterial elastance (Ea). Treatment with TFP also significantly improved stroke volume (SV) and cardiac output (CO), whereas end-systolic pressure (ESP, mmHg) and slope

of maximum and minimum derivative of the change in systolic pressure over time (dP/dtmax, dP/dtmin) were unchanged (**Figure 38B**). Further, we assessed the RV hypertrophy in MCT-treated rats by measuring cardiomyocyte cross-sectional area (CSA), which was significantly attenuated upon treatment with TFP compared to vehicle-treated animals (**Figure 38C**).

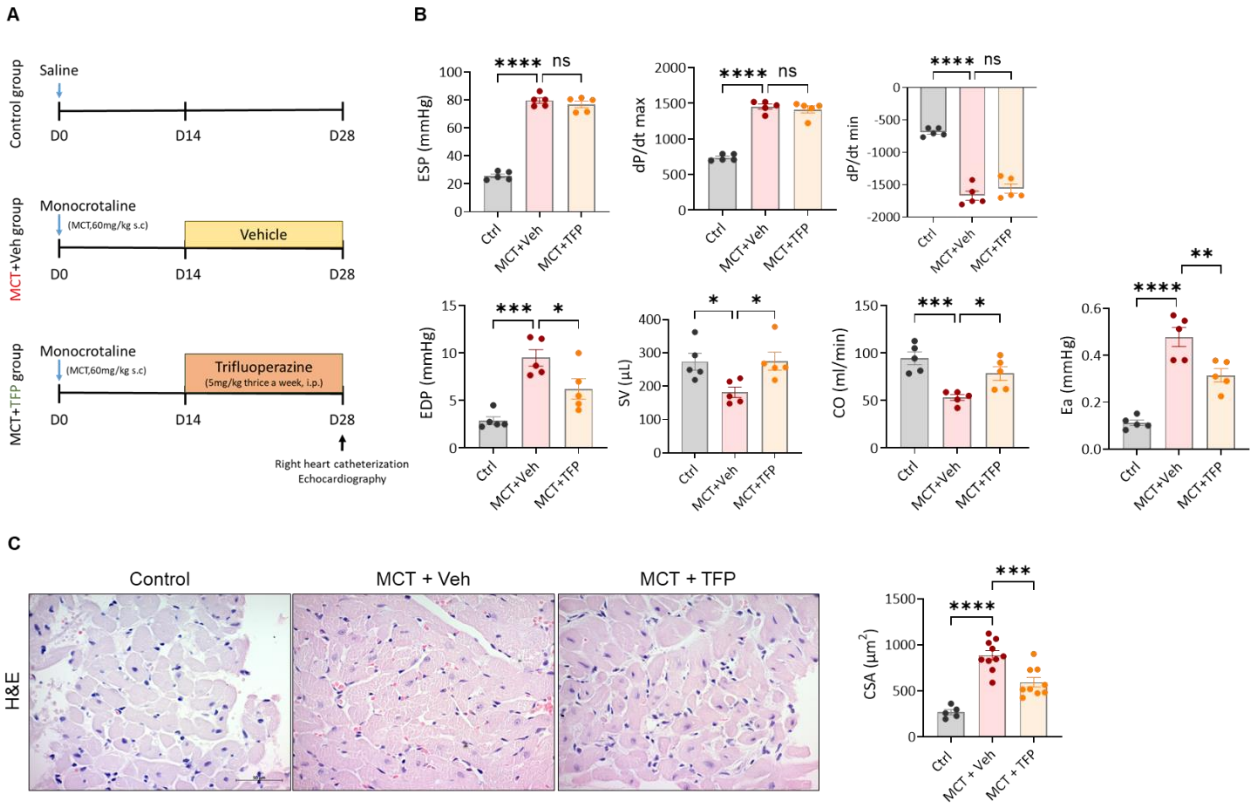

Figure 38. Effects of trifluoperazine (TFP) treatment on Monocrotaline (MCT) induced RV decompensation in rats. **A)** Schematic representation of the experimental protocol for induction and therapeutic intervention in the MCT-induced PAH rat model. **B)** End diastolic pressure (EDP, mmHg), End systolic pressure (ESP, mmHg), the slope of maximum/minimum derivative of the change in systolic pressure over time (dP/dtmax, dP/dtmin), Arterial Elastance (Ea), stroke volume (SV), cardiac output (CO). **C)** Representative images of RV CSA measured and quantified in control (CTRL) (n=5), MCT+vehicle (Veh) (n=5) and MCT+TFP (n=5) rats. Data are presented as mean ± SEM; * $p < 0.05$; ** $p < 0.01$; *** $p < 0.001$; **** $p < 0.0001$. Scale bar: 20 µm.

We then employed a second animal model, the sugen/hypoxia (Su/Hx) rat model, to assess the therapeutic effects of TFP on RV function. Rats received a single injection of sugen (a vascular endothelial growth factor (VEGF) receptor inhibitor) on day 0 and were exposed to hypoxia for 3 weeks before being randomly assigned to treatment with vehicle or TFP thrice a week for the subsequent 14 days (**Figure 39A**). On day 35, all animals underwent RHC assessment before they were sacrificed. Consistent with the results obtained in the MCT-induced RV dysfunction, administration of TFP significantly reduced end-diastolic pressure (EDP, mmHg), end-systolic pressure (ESP, mmHg) and slope of the maximum derivative of the change in systolic pressure over time (dP/dtmax). Treatment with TFP also reduced the arterial load and improved arterial elastance (Ea), whereas cardiac output (CO) was

unchanged (**Figure 39B**). Further, we assessed the RV hypertrophy in Su/Hx treated rats by measuring cardiomyocyte cross-sectional area (CSA), which was significantly attenuated upon treatment with TFP compared to vehicle-treated animals (**Figure 39C**).

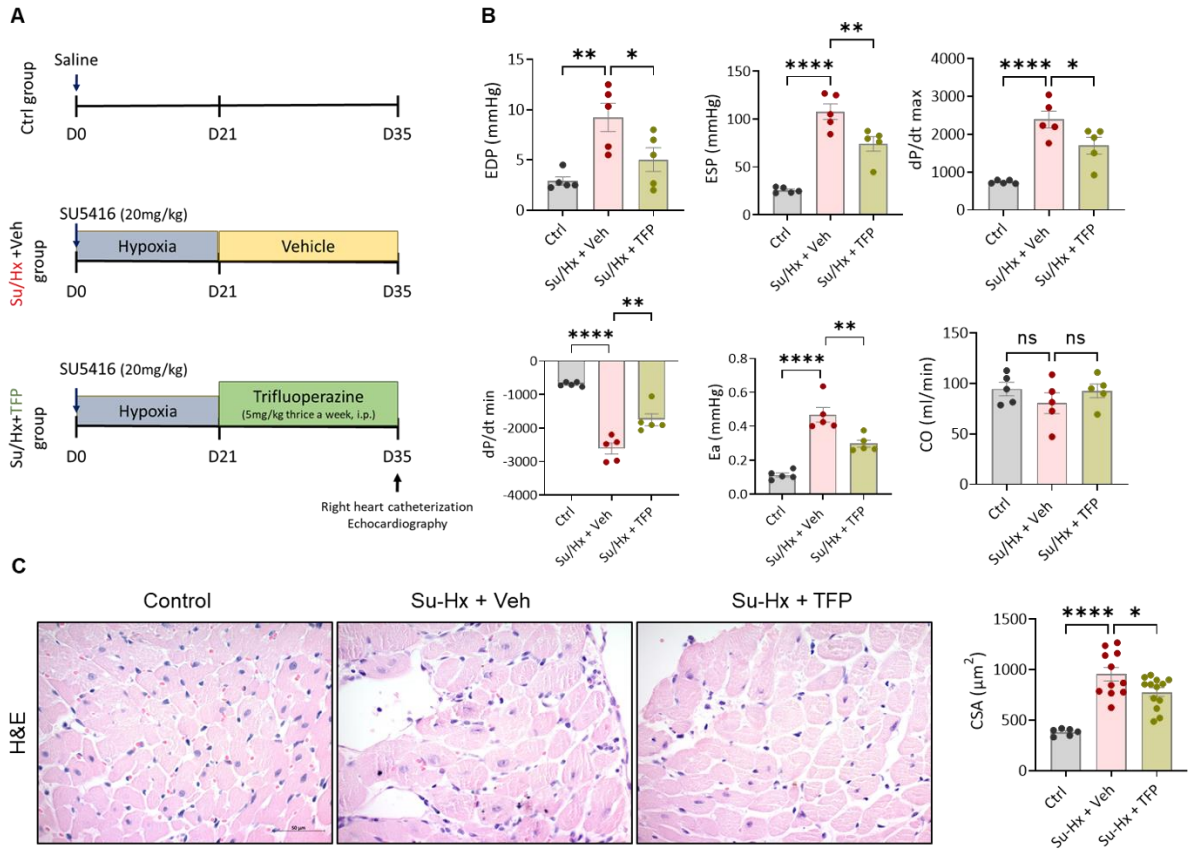

Figure 39. Effects of trifluoperazine (TFP) treatment on Sugen-Hypoxia (Su/Hx) induced RV decompensation in rats. **A)** Schematic representation of the experimental protocol for induction and therapeutic intervention in the Su/Hx-induced PAH rat model. **B)** End diastolic pressure (EDP, mmHg), End systolic pressure (ESP, mmHg), the slope of maximum/minimum derivative of the change in systolic pressure over time (dP/dtmax, dP/dtmin), Arterial Elastance (Ea), cardiac output (CO). **C)** Representative images of RV CSA measured and quantified in control (CTRL) (n=5), Su/Hx+vehicle (Veh) (n=5) and Su/Hx+TFP (n=5) rats. Data are presented as mean ± SEM; * $p < 0.05$; ** $p < 0.01$; *** $p < 0.001$; **** $p < 0.0001$. Scale bar: 20 µm.

5. DISCUSSION

Pulmonary artery hypertension (PAH) is characterized by pathological remodeling of the pulmonary vasculature, elevating right ventricular (RV) afterload and ultimately establishing RV dysfunction. RV dysfunction is the predominant predictor of death in PAH (144-146), and the responsiveness of the RV determines the survival of PAH patients. In addition, RV dysfunction is not caused only by an increase in afterload since some PAH patients indicate the development of RV dysfunction despite therapy with pulmonary vasodilators (147, 148). Currently, there are no PAH treatment options that specifically target the RV. Furthermore, markers of LV remodeling poorly predict RV dysfunction (149). Therefore, a better understanding of the fundamental molecular mechanisms that drive RV failure is necessary to improve the long-term prognosis of PAH (150).

In this study, we aimed to explore the role of the FoxO3 transcription factor during RV remodeling and dysfunction in PAH. To address our research objectives, we screened FoxO signaling molecules in human, mouse and rat RV samples. We assessed FoxO3 regulation in human primary cardiac fibroblasts exposed to various pathological stimuli. Generated fibroblast-specific foxO3 KO mice, subjected them to chronic pressure overload and evaluated the cardiac function of the mice. Additionally, two preclinical rat models of RV function were employed to assess the therapeutic potential of FoxO activators in this case, TFP, *in vivo.* The following are the key findings of this study: i) FOXO3 is increased explicitly in compensated RV and significantly decreased in decompensated RV, ii) mRNA expression of FOXO1 and FOXO3 is downregulated in compensated and decompensated RV of PAH patients, iii) histological expression of FOXO3 is reduced in decompensated RV, iv) Foxo3 activity and histological expression are dysregulated in MCT rats and PAB RV of the mouse, v) FoxO3 is dysregulated in various pathophysiological processes involved in RV dysfunction, vi) fibroblast specific deletion of FoxO3 declined RV function in mice subjected to PAB, vii) pharmacological activation of FoxO3 prevent RV dysfunction in Su-Hx and MCT rat models.

5.1 Inactivation of Foxo3 transcription factor in human decompensated RV

RV hypertrophy is an adaptive or compensated response to pathological remodeling of pulmonary arteries; if not paid attention, it can eventually lead to maladaptive or decompensated RV, one of the strongest causes of mortality in PAH patients (144) (**Figure 40**). Several groups worldwide are investigating strategies to reverse decompensated state or prolong the compensated state of RV. Since FOXOs are key transcription factors involved in multiple aspects of cardiac diseases, they have emerged as promising targets in recent years. Therefore, it is crucial to understand the FOXO regulation in physiological and pathological RV hypertrophy.

The role of FOXO3 has not been elucidated in the context of RV failure until now. Our study is the first to screen FOXOs expression in human RV tissues from healthy control, compensated and decompensated RV. Interestingly, FOXO3 is upregulated during compensated hypertrophy and downregulated in decompensated RV (**Figure 9B**). Similarly, the known target genes of the FOXO signaling pathway involved in various cellular processes are also significantly regulated in RV-C and RV-DC of PAH patients. Previous studies also showed that Foxo3 is inactivated in the hypertrophic heart and can surpass the antigrowth program induced by Foxo (126). In another study by Fang et al., cardiac hypertrophic response in high-fat diet-associated obesity is mediated by the inactivation of Foxo3 by the Akt pathway (151). As shown in the study by Kim et al., the inactivation of FOXO pathways is responsible for abnormal cardiac growth in PRKAG2 diseases, which is rescued by FOXO1 overexpression (134).

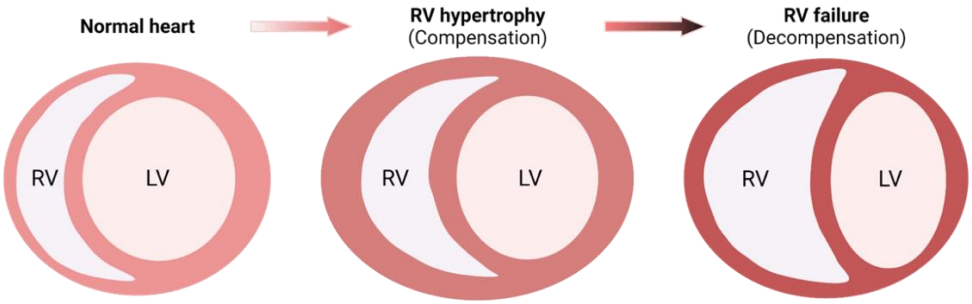

Figure 40. **Graphical representation of RV transition from compensation to decompensation.** *"Created with BioRender.com."*

Transcriptional regulation of FOXOs was further validated by qPCR from the RNA extracted from human compensated and decompensated RV tissues. Indeed both *FOXO1* and *FOXO3* were significantly downregulated in the human dcRV. Though, there was no significant change observed in the mRNA expression at the compensated state (**Figure 11A**). Furthermore, using indirect fluorescence staining of paraffin-embedded human sections, we could further validate the expression pattern and localization of FOXO3 in cRV and dcRV. The signal was predominantly in the nucleus in hRV, in the nucleus and the cytoplasm in cRV and sporadically distributed in dcRV (**Figure 12A**). Various signaling pathways that include Gq-phospholipase C-diacylglycerol (DAG)/inositol triphosphate (IP3), mitogen-activated protein kinases, calcineurin-nuclear factor of activated T cells (NFAT), phosphatidylinositol 3-kinase (PI3K)/protein kinase B (AKT), mTOR, TGF-β, play a significant role in the development of cardiac hypertrophy, and complex crosstalks and feedbacks among these pathways are widely studied (152, 153). In the field of cardiac hypertrophy research, noncoding RNAs such as microRNAs (miRNAs), circular RNAs (circRNAs), and long noncoding RNAs (lncRNAs) have also been receiving increasing interest in recent years and have been implicated in both cardiac development and pathological remodeling (154, 155). Multiple microRNAs, including

miR-1, miR-21, and miR-132/212, have been found to affect the process of vascular remodeling and cardiac hypertrophy by modulating the expression of several target genes, including 1-adrenergic receptor, TGF1 receptor III, matrix metalloproteinase-2, and connexin 43, PDGFRβ (156-158). However, the interaction of FOXO transcription factors with non-coding RNAs is underexplored, which could determine the expression pattern of FOXOs. Although the expression of FOXOs in compensatory cardiac hypertrophy of LV has been extensively studied, to our knowledge, this is the first study demonstrating a decreased FOXO1 and FOXO3 expression in the human dcRV.

5.2 Expression and localization of Foxo3 in experimental models of RV dysfunction

In the current study, two established animal models of RV dysfunction were employed to further understand the Foxo3 expression levels and localization pattern during cRV and dcRV. To begin with, we analyzed the normalized read counts from RNA-sequencing performed on the RV from control and MCT rats. The analysis demonstrated significant downregulation of *Foxo1, Foxo3* and *Foxo4* in the RV of MCT rats. At the mRNA level, Foxo3 exhibited a significant decrease in MCT rat RV (**Figure 14**). Multiple pathways are activated or inactivated during pressure overload-induced cardiac growth resulting in metabolic maladaptation, contractile dysfunction, abberant angiogenesis and dysregulated adrenergic signaling. Several growth factors, cytokines, metabolites and hormones are mediators of several pathways that can activate or inactivate FOXO proteins. These results suggest that beta2 -AR stimulation results in rapid upregulation of miR-374b-5p and miR-7a-1-3p in myotubes, resulting in a decrease in FoxO1 mRNA expression via the beta2 -AR-cAMP signaling pathway (159). Ang II signaling effects on sGC expression occurred through an AT1 receptor and FoxO transcription factor-dependent mechanism at both the mRNA and protein expression levels (160). Regulation of the stress response is a key function of FOXO transcription factors and activation of FOXOs in response to stress is partly mediated by Jun-N terminal kinase (JNK) (161). Metabolic adaptation of cardiomyocytes is fundamental to the survival of the stressed heart. The ATP-dependent potassium channels (KATP channels) are the most important sensors of cellular energy status that can strongly regulate the expression of Foxo1 and Foxo3 during the compensation and decompensation of the heart (162). Altered Ca^{2+} handling is often present in diseased hearts undergoing structural remodeling and functional deterioration. Calmodulin-dependent protein kinase II (CaMKII) and the calmodulin-dependent protein phosphatase calcineurin (Cn) are two major transducers of Ca2+ signals in cardiomyocytes which are known to regulate Foxo signaling in the heart (163). To further elucidate the molecular processes of FOXO proteins in transcriptional control, more research has focused on post-translational modifications (PTMs). >400 forms of protein PTMs, including phosphorylation, acetylation, ubiquitination, methylation, glycosylation, tiny ubiquitin-like

modification, and nitrosylation, have been identified. Different PTMs alter the expression of FOXO target genes and influence the activity, subcellular localization, DNA-binding activity, and half-life of FOXO proteins through distinct enzymatic processes (164). FOXO protein phosphorylation, mediated by various protein kinases, is the most significant PTM. Different enzymes control phosphorylation at distinct locations on FOXO proteins to generate distinct biological effects. Therefore, we next analyzed the phosphorylation status and the sub-cellular localization of Foxo3 in the control and MCT rat RV homogenates. Interestingly, the total Foxo3 levels in the nuclear fraction were significantly decreased, and phosphorylated levels of Foxo3 were increased in the MCT RV compared to ctrl RV. However, no changes were observed in the cytoplasmic fraction (**Figure 15A-15B**). Corroborating these findings, we also observed a significant reduction in the immunoreactivity of Foxo3 in rat MCT RV compared to control RV (**Figure 16**).

The MCT model is the classical experimental PAH model to study pathophysiological mechanisms and therapeutic options for the disease. However, RV dysfunction in the MCT model is due to progressive vascular remodeling. Although there are numerous well-characterized animal models for LV failure, the PAB model is the only one that can be used reliably to study RV failure. Pressure overload is the most prevalent cause of RV hypertrophy and failure in individuals with PAH and other disorders associated with PH. The PAB model of RV hypertrophy and failure has lately attracted considerable interest as one of the most important research tools for elucidating the processes driving RV remodeling and assessing possible RV-directed treatments. The most significant advantage of this model over classical animal PH models (chronic hypoxia-induced PH and monocrotaline (MCT)-induced PH) and the distinctive SuHx-PH model (combination of a vascular endothelial growth factor receptor (VEGFR) antagonist, Sugen 5416 (Su5416), and exposure to 3 weeks of chronic hypoxia in rats) is that it permits a detailed and specific investigation of the mechanisms of RV dysfunction and remodeling independent of pulmonary vascular remodeling. Creating a fixed RV pressure overload by placing a metal clip on the main pulmonary artery or ligating it with a suture to reduce the main pulmonary cross-sectional area to around 70 percent is a fundamental aspect of the PAB model, which is utilized in a variety of animals, including small (mice and rats) and large (sheep, pigs, and lambs) animals. In order to investigate the contribution of Foxo3 in RV dysfunction due to exclusive pressure overload, we further investigated the expression of Foxo3 at day 35 post-PAB. Changes in the RV function at day 35 post-PAB were more representative of the compensated state of RV hypertrophy (**Figure 17**). Western blot analysis revealed foxo3 localized in the nucleus and the phosphorylated Foxo3 at serine 253 residue (pFoxo3 (S253)) in both cytoplasm and nucleus. Although there was no significant difference in the total Foxo3 levels, pFoxo3 levels were significantly reduced in the nucleus of rats

subjected to PAB compared to sham animals (**Figure 18A-18C**), which correlates with the expression pattern of Foxo3 in human cRV. As observed in humans and the MCT model, the decompensated RV Foxo3 mRNA expression was significantly downregulated in mice and rats subjected to PAB (**Figure 19**). Consistent with stainings from human decompensated RV, the signal was predominantly in the nucleus in the sham RV. However, the overall signal intensity was substantially decreased in mice and rats subjected to PAB (**Figure 20**). Apart from the above-mentioned various signaling cascades that are activated during RV remodeling, the variability in the Foxo3 protein expression and phosphorylation between MCT and PAB model could be partly explained by RV changes in the MCT model is not a reflection of mere pressure overload that is developed in the model but also due to direct effects of MCT on the RV and system vasculature. Moreover, in the MCT model, the RV systolic pressure increases over a span of time, while they are acutely induced in the PAB model.

5.3 FOXO3 expression is diminished in human cardiac fibroblasts (CFs) in response to stiff matrix or hypoxia

The pathophysiological mechanism causing RV failure is complicated and multifaceted. Hence, in vitro models reproducing fibroblasts' adaptive and maladaptive characteristics are insufficient. Despite this, some in vitro models are necessary to understand the pathogenesis in addition to the in vivo findings.

Cardiac fibroblasts (CFs) are responsible for maintaining ECM composition and organization in the ventricular walls. They are critical mediators of the fibrosis that develops in various forms of cardiac remodeling pathologies. In response to injury, the CFs become activated and acquire a myofibroblast phenotype, characterized by pro-proliferative, excessive ECM production, and contractile phenotype due to expression of smooth muscle actin (SMA). Conversely, it is becoming increasingly clear that activated CFs display multiple overlapping phenotypes depending on their location and the stage of remodeling (165, 166). It has been established that the altered mechanical properties of the myocardium associated with cardiac diseases activate CFs (167). However, similar to the heterogeneity of CFs phenotypes, the mechanical alterations occurring in and adjacent to the infarct are regionally variable and change during the compensation and decompensation phases of remodeling. Therefore teasing out if mechanical cues regulate specific phenotypic traits may identify novel targets that could prevent the adverse progression of cardiac remodeling (168). The fibroblast to myofibroblast conversion is a complex process that requires coordinated interaction of several factors and mechanisms. It is widely described that substrate stiffness influences cell morphology and function; for example, the stiff matrix can promote stress fiber formation in cultured fibroblasts and promote their transdifferentiation into myofibroblasts (169-171). Foxo3

was found to be down-regulated in IPF myofibroblasts in the lung (132). Another important signaling that acts as a mechanosensor in the heart and other contractile cell types is YAP/TAZ signaling, which can mediate adaptive cardiac remodeling in response to pressure overload (172). YAP and TAZ are mechanoactivated coordinators of the matrix-driven feedback loop, which drives the activation of fibroblast and fibrosis (173). YAP is a known nuclear co-factor of FoxO1 and can regulate FoxO1 activity (174). Our findings also corroborate that CFs display altered phenotypes when cultured on soft and stiff matrices.

Phosphorylated protein levels of FOXO3 were increased, and total levels were decreased in CFs cultured on a stiff matrix. It could be that activated YAP/TAZ signaling under a stiff matrix could bind to FOXO3 and modulates its activity and expression. Consequently, ECM protein markers like POSTN were in CFs cultured on the stiff matrix **(Figure 22)**. Substrate stiffness also regulates integrin-mediated mechanotransduction through intracellular signal transducers such as Rho kinases (ROCK) and focal adhesion kinases (FAK) in human mesenchymal stem cells (175) and a study by Richard Seonghun et al. have previously shown that in human lung fibroblasts, β1-integrin-ECM interaction decreases FoxO3a protein levels via caspase-3-mediated cleavage and promotes fibroblast proliferation (176). However, the mRNA levels were not changed in the stiff matrix. There could be several reasons for the discrepancy in the correlation between mRNA and protein levels. There are several complex steps between transcription and translation, and a cell could be controlling the mRNA expression due to the dynamic proliferating state of the cell (177-179). The rate of post-translational processing of FOXO proteins could also be a reason for low protein with the corresponding high mRNA levels. Furthermore, to better understand the role of FOXO3 in fibroblast to myofibroblast transition in a stiff environment, CFs with loss of Foxo3 should be cultured upon soft and stiff matrix and evaluate the transcriptional responses at various time points.

Similarly, PH and RV hypertrophy frequently develop in patients with hypoxic lung disease. Acute hypoxic exposure is correlated with an increase in mean pulmonary artery pressure (mPAP), resulting in an increased hemodynamic load on the RV. In addition, hypoxia may dysregulate the transcriptional response in the RV. However, the RV responses to such changes are not fully understood (180, 181). A study by Kimberly et al. found that chronic hypoxia modified the expression of nearly 400 genes in the RV of WT animals, including biological processes associated with gene pathways related to cardiac growth, development, and cell division, which contributed to the RV hypertrophic remodeling (182).

Moreover, it is a well-known concept that an important driver of epithelial-to-mesenchymal (EMT) in cancer by upregulating remodeling marker genes (183, 184). In this line, we exposed CFs to acute hypoxia in vitro and assessed the regulation of FOXO3. Mechanistically, in

contrast to previous studies (185), a decrease in FOXO3 mRNA expression and correspondingly a significant increase in remodeling markers (ACTA2, POSTN) and hypoxic markers (CA9) were observed under hypoxia compared to normoxia. Similarly, the protein expression of FOXO3 and remodeling markers (aSMA and POSTN) were increased in hypoxia (**Figure 23**). However, studies related to HIFs and FOXO3 interaction should be further addressed because HIFs are known master regulators of hypoxic cellular response and chromatin immunoprecipitation (ChIP) studies with HIF-1α demonstrated that FoxO3 as a direct target gene of HIF-1 (186). FOXO3 downregulation that we observed in our study is contradictory to its expression in a hypoxic situation of cancers, mainly driven by its complex microenvironment that is usually not observed in the myocardium of the heart. Nevertheless, RV remodeling is a chronic process and several genes have multiple peaks and troughs throughout the timeline. It is important to assess the expression of FOXO3 at several stages of the disease to understand its precise contribution to the RV remodeling process.

5.4 Loss of Foxo3 in CFs promoted adverse RV remodeling by dysregulating homeostatic proliferation of cardiac cells and innate immune signaling

To identify target genes of FOXO3 in CFs that might influence remodeling in the heart, we cultured human primary cardiac fibroblasts and silenced FOXO3 using siRNA followed by RNA-sequencing (**Figure 24**). Our findings indicate that FOXO3 restrains a transcriptional program enriched for genes associated with interferon signaling and ephrin signaling. Type 1 interferons (IFN-I) are central mediators of antiviral responses and their transcription is regulated by multiple transcription factors (187, 188), principal amongst are the family of interferon regulatory factors (IRFs) (189). The IRF gene regulatory networks are complex and contain multiple feedback loops within themselves and other TFs. Yusuf et al. have shown Klf4 as a novel FOXO target gene in B cells and overexpressing KLF4 causes cell cycle arrest and death in B cells (190). KLF12 acts as a negative regulator of FOXO1 by directly biding to its promoter region and disrupts the successful embryo implantation (191). It is already known from previous studies that FOXO3 can mediate the transcription of interferon signaling genes in different cell types, such as macrophages (192) and neural progenitor cells (193). Corroborating this link between Foxo3 and interferon genes, a zebrafish study showed that Foxo3b, an ortholog of mammalian FOXO3, is induced by a viral infection and inhibits irf3/irf7 transcriptional activity and negatively regulates cellular antiviral response (194).

Communication between the cells is essential for organ function and stress reactions, particularly in the heart. Cardiac fibroblasts, cardiomyocytes, endothelial cells, and immune cells are the key cell types that coordinate all functional activities in the ventricular myocardium. The non-cellular extracellular matrix (ECM) that provides structure and houses growth factors

and other signaling proteins that impact cell activity is essential to this cellular network. The ECM is synthesized and regulated by myocardial cells, predominantly by cardiac fibroblasts, and it also serves as a conduit for communication between all myocardial cells (195).

After cardiac damage, inflammation is a significant regulator of the reparative response. An immediate, strong inflammatory response is crucial for commencing the healing process after injury (196). Later immunological responses enhance repair. The timing and intensity of inflammatory reactions are crucial for healthy recovery. Persistent inflammation can cause more tissue damage, whereas inadequate responses prolong the harmful effects of damaging stimuli. All elements of cardiovascular health, including cardiac fibrosis, are governed by inflammation. Immune cells and fibroblasts are intricately intertwined, with one cell controlling the function of the other. Inflammatory responses that occur in the heart continue to be poorly understood, despite the fact that their study has increased in recent years.

Previous studies have shown a strong correlation between Foxo3 and innate immune responses. RNA binding protein YTHDF3 suppresses interferon-mediated innate immune responses by promoting Foxo3 translation (197). Foxo3 is also known to regulate genes important in the development and maintenance of macrophages, dendritic cells, B and T cells (198). FOXO transcription factors also function as central regulators of bacterial stimuli-induced innate immune responses in lung epithelial cells (199). FOXO3 is implicated in regulating NK cell activity and may play a key role in antiviral innate immunity. Therefore, populations with polymorphism in the FOXO3 gene resulting in increased FOXO3 activity may be beneficial in chronic inflammation, such as cancer and cardiovascular disease, but detrimental in managing acute viral infection (200). Supporting this claim, another study showed mice epithelial cells lacking Foxo3 exhibit reduced viral clearance capacity and enhanced lung inflammation in response to a challenge with rhinovirus via reducing IFN alpha and IFN beta expression (201). There is a further need to comprehend the mechanics of heart healing because no large-scale immunomodulatory or anti-inflammatory treatment procedures have been successfully implemented in clinical practice (202).

As a central coordinator of ECM deposition, inflammation and immune responses, Cardiac fibroblasts have been presented as sentinel cells interacting with local cardiomyocytes and inflammatory cells to regulate cardiac remodeling and the role of Foxo3 in regulating cardiac fibroblast function and cardiac remodeling has not been well studied. In the present study, we generated constitutive fibroblast-specific Foxo3 knockout mice and demonstrated that loss of Foxo3 in fibroblasts significantly worsened the cardiac function after PAB-induced cardiac dysfunction in mice. Interestingly, dysregulation of ECM due to CF-specific loss of Foxo3 lead to increased cardiomyocyte hypertrophy, despite the continued pressure overload stimulus.

However, collagen content and microvascular density were not significantly altered. Histopathology is based on the qualitative examination of ultra-thin (4µm thick), two-dimensional slices extracted from a three-dimensional heart. Using two-dimensional slices to define the quantitative fibrotic or angiogenesis status of the whole RV can sometimes be misleading. A three-dimensional approach would be more appropriate to evaluate the fibrotic status in a highly complex and heterogeneous tissue like the heart. However, a significant increase in hypertrophy of cardiomyocytes and impaired cardiac conduction in fb-Foxo3 KO PAB mice could be indicative of severe RV dilatation, which can further be explained by a much significant increase in RVEDV/LVEDV parameter, a surrogate marker for chronic volume overload and diastolic dysfunction of RV (**Figure 28-31**). Moreover, loss of Foxo3 in the fibroblasts after PAB leads to amplified mRNA expression of the classical prognostic markers for hypertrophy and heart failure such as *Nppa*, *Nppb, Myh7* and *Postn* (**Figure 32**), demonstrating a severe RV dysfunction in the mutant mice subjected to PAB.

Indeed, multiple studies have addressed transcriptomic changes in the left heart using bulk sequencing under normal conditions, after ischemic injury and upon TAC injury, but the RV response to pressure overload/PAB, at least in Foxo3 dependent manner, has so far not been addressed. Although a cardiomyocyte perspective has long been studied concerning the mechanisms of heart failure progression (203-209), the advent of cell-specific ablation mouse models and next-generation sequencing has expanded the view and shifted attention at least in part to the non-myocytes of the myocardium. In our bulk RNA-seq analysis from RV tissues in wildtype and mutant mice under sham or PAB, we observed strong differential gene expression patterns between wildtype and Foxo3 mutants both at the baseline and upon PAB-induced hypertrophy. At the baseline, Foxo3 mutants displayed a strong upregulation defense response to the virus through activation of interferon signaling, and this is consistent with previous findings in other cell types that Foxo3 mediates interferon signaling in neural progenitor cells (193) and macrophages (192). When subjected to chronic pressure overload, wildtype mice upregulated 9 terms related to ECM among the top 10, which signifies myocardial ECM as highly dynamic and adaptive to changes in hemodynamic and mechanical load which preserve the geometry and integrity of the RV (210) (**Figure 34**).

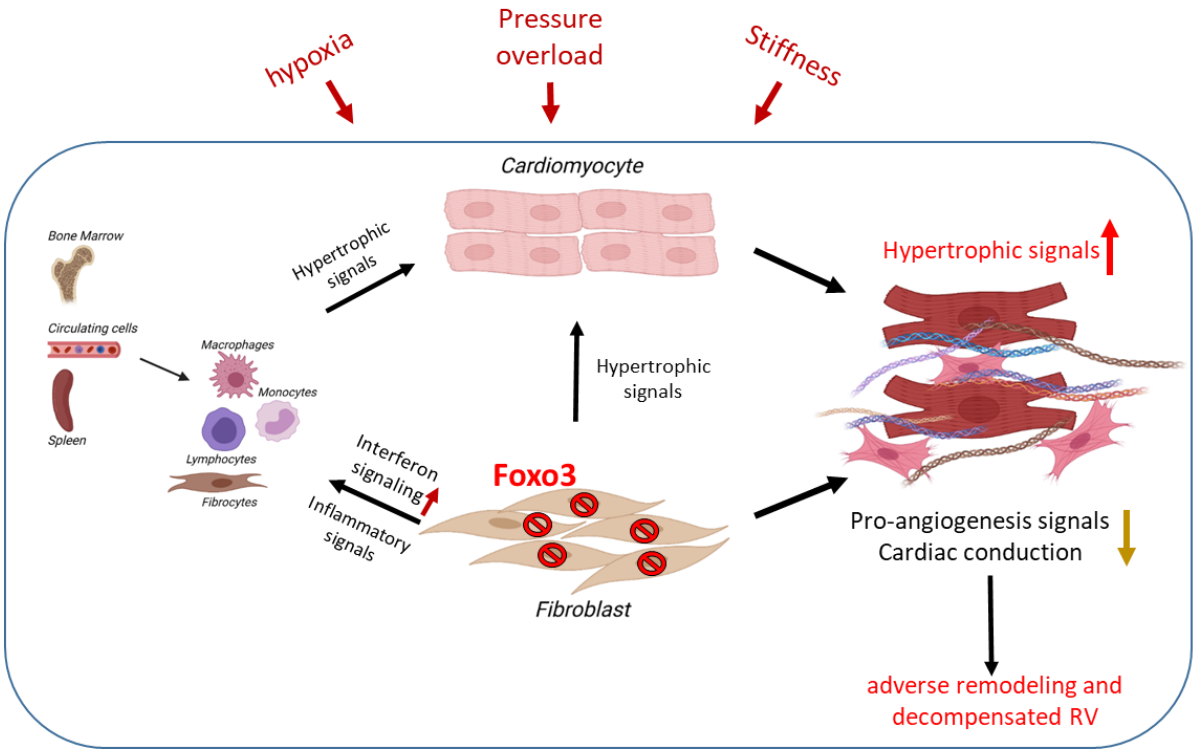

Figure 41. Schematic representation of loss of Foxo3 mediated adverse cardiac remodeling. Extra cellular pathogenic stimuli, such as hypoxia, chronic pressure overload and myocardial stiffness, modulate Foxo3 expression in fibroblasts (red 'NO' symbols), which leads to its phenotype switching by activating interferon signaling and secreting inflammatory signals that will attract the inflammatory cells to the heart. The crosstalk between pro-inflammatory fibroblasts, cardiomyocytes and endothelial cells will lead to persistent pro-hypertrophic signals, blunted angiogenic response and reduced cardiac conduction resulting in adverse cardiac remodeling and driving RV into decompensation. *"Created with BioRender.com."*

Further, our data suggest that chronic pressure overload in Foxo3 mutant mice induces pro-proliferative and anti-apoptotic phenotypes of cardiac fibroblast and smooth muscle cells leading to dysregulated collagen fibril organization. Moreover, Foxo3 mutant mice displayed a significant increase in response to ischemia indicative of increased oxygen requirements and reduced vascular density due to hypertrophy, diastolic dysfunction and abnormalities of intra-myocardial arterioles (211, 212). We also found depressed capillary density (**Figure 35**), predominantly induced in the chronic phase of pressure overload, where capillary rarefaction is known to develop, likely contributing to cardiac dysfunction. The association of capillary density with ischemic myocardium is a well-studied phenotype. FoxOs regulate endothelial cell migration and maintenance of vascular homeostasis (213-215). Loss of foxo3 could cause an imbalance in essential paracrine signaling between fibroblasts and endothelial cells, leading to aberrant angiogenesis (**Figure 41**).

Our study provides insights into the contribution of the fibroblast-specific Foxo3 role in RV remodeling and failure, which because of the use of bulk sequencing of RV tissues with a

higher sequencing depth, goes beyond the results of other studies in the field that relied mainly on a single cell in vitro cultures. It also serves as a deep resource and a reference for cardiac cellular and molecular gene expression pattern under baseline conditions and in chronic pressure overload.

5.5 Pharmacological activation of FoxO factors in vivo improves RV function

The findings from the transgenic mouse prompted the rationale that reactivation of Foxo3 could be an ideal strategy for reversing or slowing down the RV remodeling process. Given the role of FoxOs in pathological processes and aging, pharmacological modulation of FoxO functions is a potential strategy to develop new therapies and promote the survival of patients. However, FOXO factors, like many other transcription factors, are not easily targetable (216). Since FoxO transcription factors serve as the central regulator of cellular homeostasis and are tumor suppressors in human cancers, impaired FoxO activity has been reported in many cancers (217-219). So far, the only efficient method to increase FoxO activity is by using inhibitors that block upstream kinases like AKT, AMPK, PI3K that phosphorylate FoxO or by modulating microtubules (48, 220, 221). Studies in cancer and PAH, both in vitro and in vivo, show that TFP, an approved antipsychotic drug, imparts anti-tumor effects in experimental models by targeting various signaling pathways commonly dysregulated in pulmonary vascular diseases (143) (**Figure 42**). Other studies showed that PD-L1 protein levels were inversely correlated with FOXO3 protein levels in patients with ovarian, breast, and hepatocellular tumors. Pharmacological activation of FOXO3 abrogated PD-L1 protein expression and significantly improved the survival rate in syngeneic mouse tumor models (222). Other studies showed that TFP could improve myocardial function after acute occlusion of the left anterior descending artery and reperfusion (223).

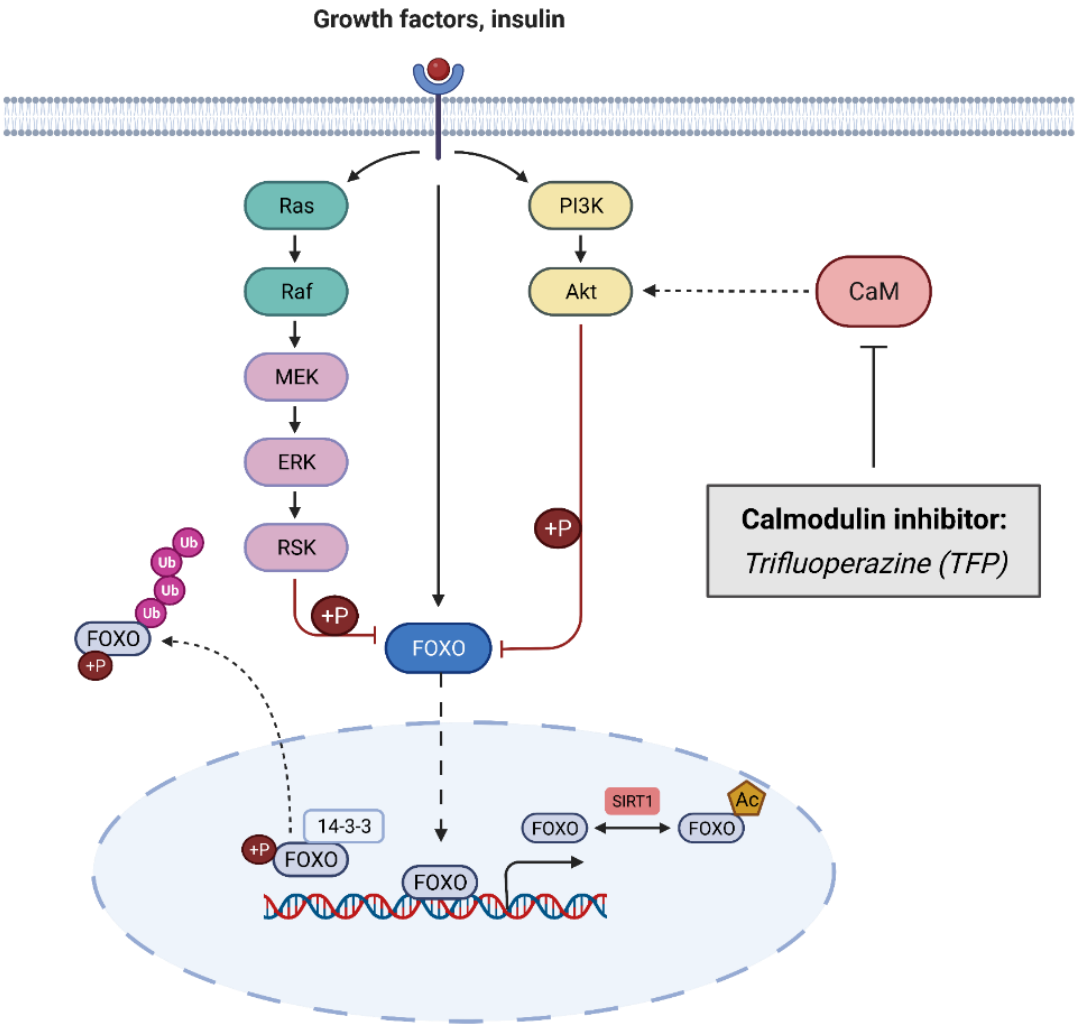

Figure 42. Schematic overview of the mechanism of modulating FoxO protein using Trifluoperazine (TFP). CaM: CalmodulinM; Ac:acetylation; P:phosphorylation; Ub: Ubiquitination. *"Created with BioRender.com."*

Until now, no concrete studies have understood the potential beneficial effects of FoxO activators in RV dysfunction. In this study, to determine the effects of TFP mediated by FoxO activation on RV function, two in vivo PAH models, MCT and SuHx rat models, were employed. MCT-injected rats and rats injected with SU5416 combined with three weeks of chronic hypoxia are the two well established PH animal models. The MCT, a toxic alkaloid, is subcutaneously injected into the rats, which progresses into PAH development characterized by increased medial wall thickening and an increase in the pulmonary artery pressures, consequently leading to structural abnormalities and dysfunction in the RV. In the Sugen/Hypoxia PAH rat model, a combination of SU5416, a vascular endothelial growth factor receptor 2 (VEGFR2) inhibitor, and subsequent exposure to chronic hypoxia is used for PH induction. The SuHx rats develop PAH due to endothelial cell death in the pulmonary vascular wall followed by the expansion of pro-proliferative and apoptotic resistant vascular cells.

Interestingly, the SuHx rat model develops neointima lesions mimicking the human PAH pathology. This model recapitulates pathological phenotypes observed in severe forms of PH, such as elements of inflammation and angio-obliteration leading to RV dilatation or failure (224, 225).

In this study, our results demonstrated that Foxo activation using TFP could be a potential therapeutic approach for PH patients with worse RV function. In two well established PH rat models, TFP treatment inhibited and reversed PH related increase in RVEDP, arterial elastance and cardiomyocyte hypertrophy (**Figures 38B and 39B**). As we know from previous studies, as the severity of PAH increases, there is an increase in max dP/dt and a decrease in min dP/dt, indicating the RV contractility changes (226). The beneficial effects of TFP on RV contractility and relaxation were observed in the Su-Hx rats, which is a more severe model of PH (**Figure 39**). In the MCT model, an improved stroke volume and cardiac output were upon treatment with TFP **(Figure 38**). Intriguingly, the in vivo cardioprotective effects of TFP were further characterized by a decrease in cardiomyocyte hypertrophy in both the animal models (**Figures 38 and 39C**). However, activating Foxo3 can be counterintuitive because studies show that Foxos can negatively regulate sirtuins (SIRTs), which play an important role in postnatal muscle growth and in preventing cachexia (227), which highlights the importance of moderate, stage and site-specific activation of FoxOs in pathologies associated with dysregulated FoxO signaling.

Therefore, our findings demonstrate that transient activation of FoxOs could serve as a potential therapeutic strategy for PAH patients with decompensated RV. Moreover, the improved contractile and relaxation properties of RV myocardium upon treatment with TFP illustrate its RV-specific beneficial effects and may serve as a therapeutic option in etiologies of RV failure other than PAH.

6. FUTURE OUTLOOK

In the present study, we have comprehensively evaluated the expression pattern of FOXO3 in the compensated and decompensated states of RV humans and further substantiated it in two animal modes of PH with severe RV dysfunction. Moreover, the current study also employs several invitro approaches to assess the expression of FOXO3 in human cardiac fibroblasts exposed to various pathophysiological stresses. Most importantly, we have generated fibroblast-specific Foxo3 KO mice and delineated the functional role of Foxo3 upon chronic pressure overload in mice. Transcriptomic analysis on the RV tissues revealed several novel signaling pathways dysregulated in fb-Foxo3 KO mice upon PAB. However, several aspects of Foxo3 signaling and its role in RV failure need to be addressed in the future outlook of this project.

6.1 Studying the role of Foxo3 in cardiac myocytes (CMs) and cardiac endothelial cells (CECs)

Since several studies showed that CMs and CECs play a significant role in cardiac remodeling and failure, studies in the context of these two cells are vital in understanding the disease progression and more cell-specific roles of Foxo3.

In vitro: Studies should address the influence of FoxO knockdown (siRNAs) or deletion (cells isolated from FoxO knockout mice) as well as constitutive activation of FoxOs (FoxO3-AAA mutants) on matrix stiffness (to mimic the PH conditions) dependent changes in cell morphology and functional aspects of CMs/CECs. The functional readouts include changes in cardiomyocyte hypertrophy, beating frequency, and assessment of cardiac function and stiffness using skinned cardiomyocytes. This should be followed by a detailed analysis of the underlying molecular signaling mechanisms.

In vivo: Myh6/7-Cre (driver line for cardiomyocytes) and Cdh5-Cre (driver line for endothelial cells) driven Foxo3 KO mouse lines need to be generated and subject them to Hypoxia+Su5416 and PAB to develop PH and RV dysfunction. In these studies, “standard” elaborate assessment of pulmonary hemodynamics and RV hypertrophy and function needs to be assessed. Moreover, specific imaging and analysis techniques should be applied to assess pulmonary artery distensibility index and RV stiffness. Since RV, systolic and diastolic longitudinal strain and strain rate were shown to be severely impaired upon chronic pressure overload MRI based speckle-tracking imaging should be employed to assess the myocardial strain/stiffness in the mutant mice that will be generated.

6.2 Comprehensive bioinformatics and Proteomic analysis of RV from fb-Foxo3 KO mice upon PAB

Further comprehensive bioinformatics approaches must be performed to gain deeper insights into Foxo3-dependent molecular targets in the heart during the remodeling process. For instance, different pair-wise comparisons of groups that were not addressed in this study, transcription factor analysis, and reconstruction of gene regulatory networks (GRN) to understand gene expression relationships between transcription factors and target genes. Using mass spectrometry-based quantitative proteomics, changes in protein expression levels need to be assessed and combined with RNA sequencing data to understand the alterations in the proteome throughout that are either or not the consequence of changes in the transcriptome.

6.3 Single-cell sequencing of RV from Wildtype and fb-Foxo3 KO mice in the presence or absence of PAB

Transcriptomic profiling studies from KO mice revealed interesting biological processes up and down-regulated such as innate immune processes like interferon and interleukin signaling and positive regulation of fibroblast proliferation. Therefore we hypothesize that a distinct proinflammatory subtype of fibroblasts is activated in the RV of KO mice upon PAB, which leads to the secretion of cytokines leading to either recruitment or activation of immune cells in the RV. Conventional bulk transcriptomics cannot reveal the cellular heterogeneity that drives this complexity of the disease. The coordinated functions of individual cells determine complex biological systems. To address this open question, we need to perform single-cell sequencing of RV from KO mice that examines the transcriptomes of individual cells, providing a high-resolution view of immune cell and fibroblasts sub populations.

6.4 Investigating the pharmacological activation of FoxOs in the pressure overload model

The beneficial effects of Trifluoperazine (TFP) that were exhibited in the in vivo rat models could be attributed to its effects on pulmonary vascular remodeling per se. In order to address the direct beneficial effects of TFP on the RV, we need to employ the PAB animal model and administer TFP in a therapeutic approach. Further molecular and biochemical assays should be performed to understand the molecular targets downstream of FoxOs. In addition, different dosages of TFP could be tested or more precise pharmacological compounds that can modulate FOXO activity to gain more prominent beneficial effects of FOXO activation. We strongly believe that understanding functional roles and specific downstream mechanisms of FoxO activation will improve treatment options for PH patients with RV dysfunction.

7. SUMMARY

Right ventricular (RV) dysfunction is often associated with poor prognosis independent of the etiology. In the context of pulmonary arterial hypertension (PAH), current clinical therapies primarily pursue vasodilation or reducing pulmonary vascular resistance, thereby alleviating the pressure overload on the RV. However, therapies that specifically target RV dysfunction are limited. Current heart failure treatment options approved for patients with left heart failure are less effective or harmful in the treatment of RV failure, given the distinctive geometry, mechanics and response to pressure overload of the RV. Therefore, it is crucial to identify cellular and molecular targets specifically altered in RV of PAH patients. Among the FoxO protein family (FoxO1, FoxO3, FoxO4, and FoxO6), FoxO3 was shown to play a critical role in various cellular processes. It is not surprising that FoxO protein inactivation has been implicated in a broad range of human diseases, including cancer, diabetes, neurodegeneration, and immune system dysfunction. Although many studies have been performed to elucidate the role of Foxo3 in cardiovascular disease in general, nothing is known in the pathophysiology of RV function, as well as specific downstream and upstream signaling pathways in the setting of RV remodeling.

During my doctoral work, I evaluated the transcriptional regulation and protein expression of FoxO isoforms in human compensated and decompensated RV. In human and preclinical animal models, FoxO3 expression is increased in the compensated state and decreased in the decompensated state of RV. FoxO3 is dysregulated in various pathophysiological processes such as hypoxia and stiff matrix that contribute to RV remodeling. Therefore, I hypothesized that fibroblast-specific ablation of FoxO3 (fb-FoxO3$^{-/-}$) in mice and subjecting them to pressure overload by performing pulmonary artery banding (PAB) would give us insights into the role of Foxo3 in RV remodeling. Accordingly, I observed that PAB caused a significant decrease in cardiac output, stroke volume, and ejection fraction, leading to much worse RV function in fb-FoxO3$^{-/-}$ mice compared to WT mice, as shown by cardiac MRI and invasive hemodynamic measurements. Further, to determine FoxO3-dependent transcriptional regulation during the remodeling process, I performed RNA-sequencing from the RV tissues and identified “pro-fibrotic pathways” and “pro-inflammatory pathways” are upregulated in the fb-FoxO3$^{-/-}$ mice compared to wildtype mice. In addition, This work provides evidence that trifluoperazine via FoxO activation improved established RV dysfunction in two preclinical models, which supports the view that transient reactivation of FoxO proteins may represent an avenue to improve RV function.

Taken together, this study signifies that FoxO3 represents a novel player in RV remodeling and serves as a new therapeutic target for treating RV failure.

8. ZUSAMMENFASSUNG

Eine rechtsventrikuläre (RV) Dysfunktion ist unabhängig von der Ätiologie häufig mit einer schlechten Prognose verbunden. Im Zusammenhang mit der pulmonalen arteriellen Hypertonie (PAH) zielen die derzeitigen klinischen Therapien in erster Linie auf eine Vasodilatation oder eine Verringerung des pulmonalen Gefäßwiderstands ab, wodurch die Drucküberlastung des RV gemildert wird. Es gibt jedoch nur wenige Therapien, die speziell auf die RV-Dysfunktion abzielen. Die derzeit für Patienten mit Linksherzinsuffizienz zugelassenen Behandlungsmöglichkeiten sind bei der Behandlung der RV-Insuffizienz aufgrund der besonderen Geometrie, Mechanik und Reaktion auf Drucküberlastung des RV weniger wirksam oder schädlich. Daher ist es von entscheidender Bedeutung, zelluläre und molekulare Ziele zu identifizieren, die im RV von PAH-Patienten spezifisch verändert sind. Von der FoxO-Proteinfamilie (FoxO1, FoxO3, FoxO4 und FoxO6) spielt FoxO3 nachweislich eine entscheidende Rolle bei verschiedenen zellulären Prozessen. Es überrascht nicht, dass die Inaktivierung des FoxO-Proteins mit einer Vielzahl menschlicher Krankheiten in Verbindung gebracht wird, darunter Krebs, Diabetes, Neurodegeneration und Funktionsstörungen des Immunsystems. Obwohl viele Studien durchgeführt wurden, um die Rolle von Foxo3 bei kardiovaskulären Erkrankungen im Allgemeinen aufzuklären, ist nichts über die Pathophysiologie der RV-Funktion sowie über spezifische nach- und vorgelagerte Signalwege im Zusammenhang mit dem RV-Remodeling bekannt.

Während meiner Doktorarbeit untersuchte ich die Transkriptionsregulation und Proteinexpression von FoxO-Isoformen im humanen kompensierten und dekompensierten RV. In humanen und präklinischen Tiermodellen ist die Expression von FoxO3 im kompensierten Zustand des RV erhöht und im dekompensierten Zustand des RV verringert. FoxO3 wird bei verschiedenen pathophysiologischen Prozessen wie Hypoxie und starrer Matrix, die zum Umbau des RV beitragen, dysreguliert. Daher stellte ich die Hypothese auf, dass die Fibroblasten-spezifische Ablation von FoxO3 (fb-FoxO3-/-) in Mäusen und deren Drucküberlastung durch Pulmonalarterienbanding (PAB) uns Einblicke in die Rolle von Foxo3 beim RV-Remodeling geben würde. Dementsprechend beobachtete ich, dass PAB eine signifikante Abnahme des Herzzeitvolumens, des Schlagvolumens und der Auswurffraktion verursachte, was zu einer deutlich schlechteren RV-Funktion bei fb-FoxO3-/--Mäusen im Vergleich zu WT-Mäusen führte, wie durch kardiale MRT und invasive hämodynamische Messungen gezeigt wurde. Um die FoxO3-abhängige Transkriptionsregulation während des Umbauprozesses zu bestimmen, führte ich eine RNA-Sequenzierung von RV-Gewebe durch und stellte fest, dass "pro-fibrotische Signalwege" und "pro-inflammatorische Signalwege" in fb-FoxO3-/--Mäusen im Vergleich zu Wildtyp-Mäusen hochreguliert sind. Darüber hinaus liefert diese Arbeit Beweise dafür, dass Trifluoperazin durch FoxO-Aktivierung die etablierte RV-

Dysfunktion in zwei präklinischen Modellen verbessert, was die Ansicht unterstützt, dass die vorübergehende Reaktivierung von FoxO-Proteinen einen Weg zur Verbesserung der RV-Funktion darstellen könnte.

Insgesamt zeigt diese Studie, dass FoxO3 ein neuartiger Akteur beim RV-Umbau ist und als neues therapeutisches Ziel für die Behandlung von RV-Versagen dienen kann.

9. REFERENCES

1. Suresh K, Shimoda LA. Lung Circulation. *Compr Physiol* 2016; 6: 897-943.
2. Ryan JW. Processing of Endogenous Polypeptides by the Lungs. *Annual Review of Physiology* 1982; 44: 241-255.
3. Dell'Italia LJ. The right ventricle: anatomy, physiology, and clinical importance. *Curr Probl Cardiol* 1991; 16: 653-720.
4. Kawel-Boehm N, Maceira A, Valsangiacomo-Buechel ER, Vogel-Claussen J, Turkbey EB, Williams R, Plein S, Tee M, Eng J, Bluemke DA. Normal values for cardiovascular magnetic resonance in adults and children. *J Cardiovasc Magn Reson* 2015; 17: 29.
5. Haddad F, Doyle R, Murphy DJ, Hunt SA. Right ventricular function in cardiovascular disease, part II: pathophysiology, clinical importance, and management of right ventricular failure. *Circulation* 2008; 117: 1717-1731.
6. Konstam MA, Kiernan MS, Bernstein D, Bozkurt B, Jacob M, Kapur NK, Kociol RD, Lewis EF, Mehra MR, Pagani FD, Raval AN, Ward C. Evaluation and Management of Right-Sided Heart Failure: A Scientific Statement From the American Heart Association. *Circulation* 2018; 137: e578-e622.
7. Sanz J, Sánchez-Quintana D, Bossone E, Bogaard HJ, Naeije R. Anatomy, Function, and Dysfunction of the Right Ventricle: JACC State-of-the-Art Review. *J Am Coll Cardiol* 2019; 73: 1463-1482.
8. Hassoun PM. Pulmonary Arterial Hypertension. *New England Journal of Medicine* 2021; 385: 2361-2376.
9. McGoon M, Gutterman D, Steen V, Barst R, McCrory DC, Fortin TA, Loyd JE. Screening, early detection, and diagnosis of pulmonary arterial hypertension: ACCP evidence-based clinical practice guidelines. *Chest* 2004; 126: 14s-34s.
10. Zaffran S, Kelly RG, Meilhac SM, Buckingham ME, Brown NA. Right ventricular myocardium derives from the anterior heart field. *Circ Res* 2004; 95: 261-268.
11. Rudolph AM. Congenital cardiovascular malformations and the fetal circulation. *Arch Dis Child Fetal Neonatal Ed* 2010; 95: F132-136.
12. Mertens LL, Friedberg MK. Imaging the right ventricle--current state of the art. *Nat Rev Cardiol* 2010; 7: 551-563.
13. Rouleau JL, Paradis P, Shenasa H, Juneau C. Faster time to peak tension and velocity of shortening in right versus left ventricular trabeculae and papillary muscles of dogs. *Circ Res* 1986; 59: 556-561.
14. Chin KM, Kim NH, Rubin LJ. The right ventricle in pulmonary hypertension. *Coron Artery Dis* 2005; 16: 13-18.
15. Sengupta PP, Korinek J, Belohlavek M, Narula J, Vannan MA, Jahangir A, Khandheria BK. Left ventricular structure and function: basic science for cardiac imaging. *J Am Coll Cardiol* 2006; 48: 1988-2001.
16. Geva T, Powell AJ, Crawford EC, Chung T, Colan SD. Evaluation of regional differences in right ventricular systolic function by acoustic quantification echocardiography and cine magnetic resonance imaging. *Circulation* 1998; 98: 339-345.
17. Friedberg MK, Redington AN. Right Versus Left Ventricular Failure. *Circulation* 2014; 129: 1033-1044.
18. Vonk-Noordegraaf A, Haddad F, Chin KM, Forfia PR, Kawut SM, Lumens J, Naeije R, Newman J, Oudiz RJ, Provencher S, Torbicki A, Voelkel NF, Hassoun PM. Right heart adaptation to pulmonary arterial hypertension: physiology and pathobiology. *J Am Coll Cardiol* 2013; 62: D22-33.
19. Wiesmann F, Frydrychowicz A, Rautenberg J, Illinger R, Rommel E, Haase A, Neubauer S. Analysis of right ventricular function in healthy mice and a murine model of heart failure by in vivo MRI. *Am J Physiol Heart Circ Physiol* 2002; 283: H1065-1071.
20. Egemnazarov B, Crnkovic S, Nagy BM, Olschewski H, Kwapiszewska G. Right ventricular fibrosis and dysfunction: Actual concepts and common misconceptions. *Matrix Biol* 2018; 68-69: 507-521.

21. Sydykov A, Mamazhakypov A, Petrovic A, Kosanovic D, Sarybaev AS, Weissmann N, Ghofrani HA, Schermuly RT. Inflammatory Mediators Drive Adverse Right Ventricular Remodeling and Dysfunction and Serve as Potential Biomarkers. *Frontiers in Physiology* 2018; 9.
22. Frump AL, Bonnet S, de Jesus Perez VA, Lahm T. Emerging role of angiogenesis in adaptive and maladaptive right ventricular remodeling in pulmonary hypertension. *Am J Physiol Lung Cell Mol Physiol* 2018; 314: L443-l460.
23. Viswanathan G, Mamazhakypov A, Schermuly RT, Rajagopal S. The Role of G Protein-Coupled Receptors in the Right Ventricle in Pulmonary Hypertension. *Frontiers in Cardiovascular Medicine* 2018; 5.
24. Ryan JJ, Archer SL. Emerging concepts in the molecular basis of pulmonary arterial hypertension: part I: metabolic plasticity and mitochondrial dynamics in the pulmonary circulation and right ventricle in pulmonary arterial hypertension. *Circulation* 2015; 131: 1691-1702.
25. Piao L, Marsboom G, Archer SL. Mitochondrial metabolic adaptation in right ventricular hypertrophy and failure. *Journal of molecular medicine (Berlin, Germany)* 2010; 88: 1011-1020.
26. Shults NV, Melnyk O, Suzuki DI, Suzuki YJ. Redox Biology of Right-Sided Heart Failure. *Antioxidants (Basel)* 2018; 7.
27. Bristow MR, Zisman LS, Lowes BD, Abraham WT, Badesch DB, Groves BM, Voelkel NF, Lynch DM, Quaife RA. The pressure-overloaded right ventricle in pulmonary hypertension. *Chest* 1998; 114: 101s-106s.
28. Voelkel NF, Quaife RA, Leinwand LA, Barst RJ, McGoon MD, Meldrum DR, Dupuis J, Long CS, Rubin LJ, Smart FW, Suzuki YJ, Gladwin M, Denholm EM, Gail DB. Right ventricular function and failure: report of a National Heart, Lung, and Blood Institute working group on cellular and molecular mechanisms of right heart failure. *Circulation* 2006; 114: 1883-1891.
29. Esfandiary A, Kutsche HS, Schreckenberg R, Weber M, Pak O, Kojonazarov B, Sydykov A, Hirschhäuser C, Wolf A, Haag D, Hecker M, Fink L, Seeger W, Ghofrani HA, Schermuly RT, Weißmann N, Schulz R, Rohrbach S, Li L, Sommer N, Schlüter KD. Protection against pressure overload-induced right heart failure by uncoupling protein 2 silencing. *Cardiovasc Res* 2019; 115: 1217-1227.
30. Kocken JMM, da Costa Martins PA. Epigenetic Regulation of Pulmonary Arterial Hypertension-Induced Vascular and Right Ventricular Remodeling: New Opportunities? *International Journal of Molecular Sciences* 2020; 21: 8901.
31. Lee Tong I, Young Richard A. Transcriptional Regulation and Its Misregulation in Disease. *Cell* 2013; 152: 1237-1251.
32. Singh H, Khan AA, Dinner AR. Gene regulatory networks in the immune system. *Trends Immunol* 2014; 35: 211-218.
33. Geertz M, Shore D, Maerkl SJ. Massively parallel measurements of molecular interaction kinetics on a microfluidic platform. *Proceedings of the National Academy of Sciences* 2012; 109: 16540-16545.
34. Ptashne M. Principles of a switch. *Nat Chem Biol* 2011; 7: 484-487.
35. Mitsis T, Efthimiadou A, Bacopoulou F, Vlachakis D, Chrousos GP, Eliopoulos E. Transcription factors and evolution: An integral part of gene expression (Review). *World Acad Sci J* 2020; 2: 3-8.
36. Powell RV, Willett CR, Goertzen LR, Rashotte AM. Lineage specific conservation of cis-regulatory elements in Cytokinin Response Factors. *Scientific reports* 2019; 9: 13387-13387.
37. Rebeiz M, Tsiantis M. Enhancer evolution and the origins of morphological novelty. *Curr Opin Genet Dev* 2017; 45: 115-123.
38. Yesudhas D, Batool M, Anwar MA, Panneerselvam S, Choi S. Proteins Recognizing DNA: Structural Uniqueness and Versatility of DNA-Binding Domains in Stem Cell Transcription Factors. *Genes* 2017; 8: 192.

39. Cheatle Jarvela AM, Hinman VF. Evolution of transcription factor function as a mechanism for changing metazoan developmental gene regulatory networks. *EvoDevo* 2015; 6: 3.
40. Albalat R, Cañestro C. Evolution by gene loss. *Nature Reviews Genetics* 2016; 17: 379-391.
41. Rosanova A, Colliva A, Osella M, Caselle M. Modelling the evolution of transcription factor binding preferences in complex eukaryotes. *Scientific Reports* 2017; 7: 7596.
42. Bourgeois A, Lambert C, Habbout K, Ranchoux B, Paquet-Marceau S, Trinh I, Breuils-Bonnet S, Paradis R, Nadeau V, Paulin R, Provencher S, Bonnet S, Boucherat O. FOXM1 promotes pulmonary artery smooth muscle cell expansion in pulmonary arterial hypertension. *J Mol Med (Berl)* 2018; 96: 223-235.
43. Pullamsetti SS, Kojonazarov B, Storn S, Gall H, Salazar Y, Wolf J, Weigert A, El-Nikhely N, Ghofrani HA, Krombach GA, Fink L, Gattenlöhner S, Rapp UR, Schermuly RT, Grimminger F, Seeger W, Savai R. Lung cancer-associated pulmonary hypertension: Role of microenvironmental inflammation based on tumor cell-immune cell cross-talk. *Sci Transl Med* 2017; 9.
44. Ball MK, Waypa GB, Mungai PT, Nielsen JM, Czech L, Dudley VJ, Beussink L, Dettman RW, Berkelhamer SK, Steinhorn RH, Shah SJ, Schumacker PT. Regulation of hypoxia-induced pulmonary hypertension by vascular smooth muscle hypoxia-inducible factor-1α. *Am J Respir Crit Care Med* 2014; 189: 314-324.
45. Kapitsinou PP, Rajendran G, Astleford L, Michael M, Schonfeld MP, Fields T, Shay S, French JL, West J, Haase VH. The Endothelial Prolyl-4-Hydroxylase Domain 2/Hypoxia-Inducible Factor 2 Axis Regulates Pulmonary Artery Pressure in Mice. *Mol Cell Biol* 2016; 36: 1584-1594.
46. Calvier L, Chouvarine P, Legchenko E, Hoffmann N, Geldner J, Borchert P, Jonigk D, Mozes MM, Hansmann G. PPARγ Links BMP2 and TGFβ1 Pathways in Vascular Smooth Muscle Cells, Regulating Cell Proliferation and Glucose Metabolism. *Cell Metab* 2017; 25: 1118-1134.e1117.
47. Ruffenach G, Chabot S, Tanguay VF, Courboulin A, Boucherat O, Potus F, Meloche J, Pflieger A, Breuils-Bonnet S, Nadeau V, Paradis R, Tremblay E, Girerd B, Hautefort A, Montani D, Fadel E, Dorfmuller P, Humbert M, Perros F, Paulin R, Provencher S, Bonnet S. Role for Runt-related Transcription Factor 2 in Proliferative and Calcified Vascular Lesions in Pulmonary Arterial Hypertension. *Am J Respir Crit Care Med* 2016; 194: 1273-1285.
48. Savai R, Al-Tamari HM, Sedding D, Kojonazarov B, Muecke C, Teske R, Capecchi MR, Weissmann N, Grimminger F, Seeger W, Schermuly RT, Pullamsetti SS. Pro-proliferative and inflammatory signaling converge on FoxO1 transcription factor in pulmonary hypertension. *Nat Med* 2014; 20: 1289-1300.
49. Zhang H, Wang D, Li M, Plecitá-Hlavatá L, D'Alessandro A, Tauber J, Riddle S, Kumar S, Flockton A, McKeon BA, Frid MG, Reisz JA, Caruso P, El Kasmi KC, Ježek P, Morrell NW, Hu CJ, Stenmark KR. Metabolic and Proliferative State of Vascular Adventitial Fibroblasts in Pulmonary Hypertension Is Regulated Through a MicroRNA-124/PTBP1 (Polypyrimidine Tract Binding Protein 1)/Pyruvate Kinase Muscle Axis. *Circulation* 2017; 136: 2468-2485.
50. Li M, Riddle S, Zhang H, D'Alessandro A, Flockton A, Serkova NJ, Hansen KC, Moldovan R, McKeon BA, Frid M, Kumar S, Li H, Liu H, Caánovas A, Medrano JF, Thomas MG, Iloska D, Plecitá-Hlavatá L, Ježek P, Pullamsetti S, Fini MA, El Kasmi KC, Zhang Q, Stenmark KR. Metabolic Reprogramming Regulates the Proliferative and Inflammatory Phenotype of Adventitial Fibroblasts in Pulmonary Hypertension Through the Transcriptional Corepressor C-Terminal Binding Protein-1. *Circulation* 2016; 134: 1105-1121.
51. Kudryashova TV, Goncharov DA, Pena A, Kelly N, Vanderpool R, Baust J, Kobir A, Shufesky W, Mora AL, Morelli AE, Zhao J, Ihida-Stansbury K, Chang B, DeLisser H, Tuder RM, Kawut SM, Silljé HH, Shapiro S, Zhao Y, Goncharova EA. HIPPO-Integrin-linked Kinase Cross-Talk Controls Self-Sustaining Proliferation and Survival in Pulmonary Hypertension. *Am J Respir Crit Care Med* 2016; 194: 866-877.

52. Vattulainen-Collanus S, Akinrinade O, Li M, Koskenvuo M, Li CG, Rao SP, de Jesus Perez V, Yuan K, Sawada H, Koskenvuo JW, Alvira C, Rabinovitch M, Alastalo TP. Loss of PPARγ in endothelial cells leads to impaired angiogenesis. *J Cell Sci* 2016; 129: 693-705.
53. Bertero T, Oldham WM, Cottrill KA, Pisano S, Vanderpool RR, Yu Q, Zhao J, Tai Y, Tang Y, Zhang YY, Rehman S, Sugahara M, Qi Z, Gorcsan J, 3rd, Vargas SO, Saggar R, Saggar R, Wallace WD, Ross DJ, Haley KJ, Waxman AB, Parikh VN, De Marco T, Hsue PY, Morris A, Simon MA, Norris KA, Gaggioli C, Loscalzo J, Fessel J, Chan SY. Vascular stiffness mechanoactivates YAP/TAZ-dependent glutaminolysis to drive pulmonary hypertension. *J Clin Invest* 2016; 126: 3313-3335.
54. Zhao L, Oliver E, Maratou K, Atanur SS, Dubois OD, Cotroneo E, Chen CN, Wang L, Arce C, Chabosseau PL, Ponsa-Cobas J, Frid MG, Moyon B, Webster Z, Aldashev A, Ferrer J, Rutter GA, Stenmark KR, Aitman TJ, Wilkins MR. The zinc transporter ZIP12 regulates the pulmonary vascular response to chronic hypoxia. *Nature* 2015; 524: 356-360.
55. Humbert M, Guignabert C, Bonnet S, Dorfmüller P, Klinger JR, Nicolls MR, Olschewski AJ, Pullamsetti SS, Schermuly RT, Stenmark KR, Rabinovitch M. Pathology and pathobiology of pulmonary hypertension: state of the art and research perspectives. *Eur Respir J* 2019; 53.
56. Dansen TB, Burgering BMT. Unravelling the tumor-suppressive functions of FOXO proteins. *Trends in cell biology* 2008; 18 9: 421-429.
57. Zhang X, Tang N, Hadden TJ, Rishi AK. Akt, FoxO and regulation of apoptosis. *Biochim Biophys Acta* 2011; 1813: 1978-1986.
58. Tothova Z, Kollipara R, Huntly BJ, Lee BH, Castrillon DH, Cullen DE, McDowell EP, Lazo-Kallanian S, Williams IR, Sears C, Armstrong SA, Passegué E, DePinho RA, Gilliland DG. FoxOs are critical mediators of hematopoietic stem cell resistance to physiologic oxidative stress. *Cell* 2007; 128: 325-339.
59. Kaestner KH. The Hepatocyte Nuclear Factor 3 (HNF3 or FOXA) Family in Metabolism. *Trends in Endocrinology & Metabolism* 2000; 11: 281-285.
60. Lehmann OJ, Sowden JC, Carlsson P, Jordan T, Bhattacharya SS. Fox's in development and disease. *Trends Genet* 2003; 19: 339-344.
61. Anderson MJ, Viars CS, Czekay S, Cavenee WK, Arden KC. Cloning and characterization of three human forkhead genes that comprise an FKHR-like gene subfamily. *Genomics* 1998; 47: 187-199.
62. Calissi G, Lam EW, Link W. Therapeutic strategies targeting FOXO transcription factors. *Nat Rev Drug Discov* 2021; 20: 21-38.
63. Biggs WH, 3rd, Cavenee WK, Arden KC. Identification and characterization of members of the FKHR (FOX O) subclass of winged-helix transcription factors in the mouse. *Mamm Genome* 2001; 12: 416-425.
64. Jacobs FM, van der Heide LP, Wijchers PJ, Burbach JP, Hoekman MF, Smidt MP. FoxO6, a novel member of the FoxO class of transcription factors with distinct shuttling dynamics. *J Biol Chem* 2003; 278: 35959-35967.
65. Calnan DR, Brunet A. The FoxO code. *Oncogene* 2008; 27: 2276-2288.
66. Klotz LO, Sánchez-Ramos C, Prieto-Arroyo I, Urbánek P, Steinbrenner H, Monsalve M. Redox regulation of FoxO transcription factors. *Redox Biol* 2015; 6: 51-72.
67. Obsilova V, Vecer J, Herman P, Pabianova A, Sulc M, Teisinger J, Boura E, Obsil T. 14-3-3 Protein Interacts with Nuclear Localization Sequence of Forkhead Transcription Factor FoxO4. *Biochemistry* 2005; 44: 11608-11617.
68. Rena G, Woods YL, Prescott AR, Peggie M, Unterman TG, Williams MR, Cohen P. Two novel phosphorylation sites on FKHR that are critical for its nuclear exclusion. *The EMBO Journal* 2002; 21: 2263-2271.
69. Teleman AA, Chen Y-W, Cohen SM. Drosophila Melted Modulates FOXO and TOR Activity. *Developmental Cell* 2005; 9: 271-281.

70. Huang H, Regan KM, Wang F, Wang D, Smith DI, Deursen JMAv, Tindall DJ. Skp2 inhibits FOXO1 in tumor suppression through ubiquitin-mediated degradation. *Proceedings of the National Academy of Sciences* 2005; 102: 1649-1654.
71. Yuan Z, Becker EB, Merlo P, Yamada T, DiBacco S, Konishi Y, Schaefer EM, Bonni A. Activation of FOXO1 by Cdk1 in cycling cells and postmitotic neurons. *Science* 2008; 319: 1665-1668.
72. Mattila J, Kallijärvi J, Puig O. RNAi screening for kinases and phosphatases identifies FoxO regulators. *Proc Natl Acad Sci U S A* 2008; 105: 14873-14878.
73. Bertaggia E, Coletto L, Sandri M. Posttranslational modifications control FoxO3 activity during denervation. *Am J Physiol Cell Physiol* 2012; 302: C587-596.
74. Manning BD, Toker A. AKT/PKB Signaling: Navigating the Network. *Cell* 2017; 169: 381-405.
75. Motta MC, Divecha N, Lemieux M, Kamel C, Chen D, Gu W, Bultsma Y, McBurney M, Guarente L. Mammalian SIRT1 represses forkhead transcription factors. *Cell* 2004; 116: 551-563.
76. van der Horst A, Tertoolen LG, de Vries-Smits LM, Frye RA, Medema RH, Burgering BM. FOXO4 is acetylated upon peroxide stress and deacetylated by the longevity protein hSir2(SIRT1). *J Biol Chem* 2004; 279: 28873-28879.
77. Matsuzaki H, Daitoku H, Hatta M, Aoyama H, Yoshimochi K, Fukamizu A. Acetylation of Foxo1 alters its DNA-binding ability and sensitivity to phosphorylation. *Proc Natl Acad Sci U S A* 2005; 102: 11278-11283.
78. Aimjongjun S, Mahmud Z, Jiramongkol Y, Alasiri G, Yao S, Yagüe E, Janvilisri T, Lam EW. Lapatinib sensitivity in nasopharyngeal carcinoma is modulated by SIRT2-mediated FOXO3 deacetylation. *BMC Cancer* 2019; 19: 1106.
79. Sun W, Qiao W, Zhou B, Hu Z, Yan Q, Wu J, Wang R, Zhang Q, Miao D. Overexpression of Sirt1 in mesenchymal stem cells protects against bone loss in mice by FOXO3a deacetylation and oxidative stress inhibition. *Metabolism* 2018; 88: 61-71.
80. Mahmud Z, Gomes AR, Lee HJ, Aimjongjun S, Jiramongkol Y, Yao S, Zona S, Alasiri G, Gong G, Yagüe E, Lam EW. EP300 and SIRT1/6 Co-Regulate Lapatinib Sensitivity Via Modulating FOXO3-Acetylation and Activity in Breast Cancer. *Cancers (Basel)* 2019; 11.
81. Qiang L, Banks AS, Accili D. Uncoupling of acetylation from phosphorylation regulates FoxO1 function independent of its subcellular localization. *J Biol Chem* 2010; 285: 27396-27401.
82. Brown AK, Webb AE. Regulation of FOXO Factors in Mammalian Cells. *Curr Top Dev Biol* 2018; 127: 165-192.
83. Huang H, Tindall DJ. Regulation of FOXO protein stability via ubiquitination and proteasome degradation. *Biochimica et biophysica acta* 2011; 1813: 1961-1964.
84. Xie Q, Hao Y, Tao L, Peng S, Rao C, Chen H, You H, Dong M-q, Yuan Z. Lysine methylation of FOXO3 regulates oxidative stress-induced neuronal cell death. *EMBO reports* 2012; 13: 371-377.
85. Yamagata K, Daitoku H, Takahashi Y, Namiki K, Hisatake K, Kako K, Mukai H, Kasuya Y, Fukamizu A. Arginine Methylation of FOXO Transcription Factors Inhibits Their Phosphorylation by Akt. *Molecular Cell* 2008; 32: 221-231.
86. Wang F, Chan CH, Chen K, Guan X, Lin HK, Tong Q. Deacetylation of FOXO3 by SIRT1 or SIRT2 leads to Skp2-mediated FOXO3 ubiquitination and degradation. *Oncogene* 2012; 31: 1546-1557.
87. Potente M, Urbich C, Sasaki K-i, Hofmann WK, Heeschen C, Aicher A, Kollipara R, DePinho RA, Zeiher AM, Dimmeler S. Involvement of Foxo transcription factors in angiogenesis and postnatal neovascularization. *The Journal of Clinical Investigation* 2005; 115: 2382-2392.
88. Furukawa-Hibi Y, Kobayashi Y, Chen C, Motoyama N. FOXO transcription factors in cell-cycle regulation and the response to oxidative stress. *Antioxid Redox Signal* 2005; 7: 752-760.

89. Furukawa-Hibi Y, Yoshida-Araki K, Ohta T, Ikeda K, Motoyama N. FOXO forkhead transcription factors induce G(2)-M checkpoint in response to oxidative stress. *J Biol Chem* 2002; 277: 26729-26732.
90. Tran H, Brunet A, Grenier JM, Datta SR, Fornace AJ, DiStefano PS, Chiang LW, Greenberg ME. DNA Repair Pathway Stimulated by the Forkhead Transcription Factor FOXO3a Through the Gadd45 Protein. *Science* 2002; 296: 530-534.
91. Henderson ST, Johnson TE. daf-16 integrates developmental and environmental inputs to mediate aging in the nematode Caenorhabditis elegans. *Curr Biol* 2001; 11: 1975-1980.
92. Fu Z, Tindall DJ. FOXOs, cancer and regulation of apoptosis. *Oncogene* 2008; 27: 2312-2319.
93. Sandri M, Sandri C, Gilbert A, Skurk C, Calabria E, Picard A, Walsh K, Schiaffino S, Lecker SH, Goldberg AL. Foxo transcription factors induce the atrophy-related ubiquitin ligase atrogin-1 and cause skeletal muscle atrophy. *Cell* 2004; 117: 399-412.
94. Kerdiles YM, Beisner DR, Tinoco R, Dejean AS, Castrillon DH, DePinho RA, Hedrick SM. Foxo1 links homing and survival of naive T cells by regulating L-selectin, CCR7 and interleukin 7 receptor. *Nat Immunol* 2009; 10: 176-184.
95. Gross DN, Wan M, Birnbaum MJ. The role of FOXO in the regulation of metabolism. *Current Diabetes Reports* 2009; 9: 208-214.
96. Greer EL, Brunet A. FOXO transcription factors at the interface between longevity and tumor suppression. *Oncogene* 2005; 24: 7410-7425.
97. Coomans de Brachène A, Demoulin JB. FOXO transcription factors in cancer development and therapy. *Cell Mol Life Sci* 2016; 73: 1159-1172.
98. Link W, Fernandez-Marcos PJ. FOXO transcription factors at the interface of metabolism and cancer. *Int J Cancer* 2017; 141: 2379-2391.
99. Yang JY, Zong CS, Xia W, Yamaguchi H, Ding Q, Xie X, Lang JY, Lai CC, Chang CJ, Huang WC, Huang H, Kuo HP, Lee DF, Li LY, Lien HC, Cheng X, Chang KJ, Hsiao CD, Tsai FJ, Tsai CH, Sahin AA, Muller WJ, Mills GB, Yu D, Hortobagyi GN, Hung MC. ERK promotes tumorigenesis by inhibiting FOXO3a via MDM2-mediated degradation. *Nat Cell Biol* 2008; 10: 138-148.
100. Zeng Z, Samudio IJ, Zhang W, Estrov Z, Pelicano H, Harris D, Frolova O, Hail N, Jr., Chen W, Kornblau SM, Huang P, Lu Y, Mills GB, Andreeff M, Konopleva M. Simultaneous inhibition of PDK1/AKT and Fms-like tyrosine kinase 3 signaling by a small-molecule KP372-1 induces mitochondrial dysfunction and apoptosis in acute myelogenous leukemia. *Cancer Res* 2006; 66: 3737-3746.
101. Birkenkamp KU, Essafi A, van der Vos KE, da Costa M, Hui RCY, Holstege F, Koenderman L, Lam EWF, Coffer PJ. FOXO3a Induces Differentiation of Bcr-Abl-transformed Cells through Transcriptional Down-regulation of Id1 *. *Journal of Biological Chemistry* 2007; 282: 2211-2220.
102. Liang C, Chen W, Zhi X, Ma T, Xia X, Liu H, Zhang Q, Hu Q, Zhang Y, Bai X, Liang T. Serotonin promotes the proliferation of serum-deprived hepatocellular carcinoma cells via upregulation of FOXO3a. *Molecular Cancer* 2013; 12: 14.
103. Krenning G, Zeisberg EM, Kalluri R. The origin of fibroblasts and mechanism of cardiac fibrosis. *J Cell Physiol* 2010; 225: 631-637.
104. Ingber DE. Tensegrity and mechanotransduction. *J Bodyw Mov Ther* 2008; 12: 198-200.
105. Fang Y, Chang Z, Xu Z, Hu J, Zhou H, Yu S, Wan X. Osteoglycin silencing exerts inhibitory effects on myocardial fibrosis and epithelial/endothelial-mesenchymal transformation in a mouse model of myocarditis. *BioFactors (Oxford, England)* 2020; 46: 1018-1030.
106. Norambuena-Soto I, Núñez-Soto C, Sanhueza-Olivares F, Cancino-Arenas N, Mondaca-Ruff D, Vivar R, Díaz-Araya G, Mellado R, Chiong M. Transforming growth factor-beta and Forkhead box O transcription factors as cardiac fibroblast regulators. *Biosci Trends* 2017; 11: 154-162.
107. Wight TN, Potter-Perigo S. The extracellular matrix: an active or passive player in fibrosis? *Am J Physiol Gastrointest Liver Physiol* 2011; 301: G950-955.

108. Lin A, Piao HL, Zhuang L, Sarbassov dos D, Ma L, Gan B. FoxO transcription factors promote AKT Ser473 phosphorylation and renal tumor growth in response to pharmacologic inhibition of the PI3K-AKT pathway. *Cancer Res* 2014; 74: 1682-1693.
109. Nho RS, Peterson M, Hergert P, Henke CA. FoxO3a (Forkhead Box O3a) deficiency protects Idiopathic Pulmonary Fibrosis (IPF) fibroblasts from type I polymerized collagen matrix-induced apoptosis via caveolin-1 (cav-1) and Fas. *PLoS One* 2013; 8: e61017.
110. Im J, Hergert P, Nho RS. Reduced FoxO3a expression causes low autophagy in idiopathic pulmonary fibrosis fibroblasts on collagen matrices. *Am J Physiol Lung Cell Mol Physiol* 2015; 309: L552-561.
111. Li A, Wang J, Wu M, Zhang X, Zhang H. The inhibition of activated hepatic stellate cells proliferation by arctigenin through G0/G1 phase cell cycle arrest: Persistent p27Kip1 induction by interfering with PI3K/Akt/FOXO3a signaling pathway. *European Journal of Pharmacology* 2015; 747: 71-87.
112. Bui AL, Horwich TB, Fonarow GC. Epidemiology and risk profile of heart failure. *Nat Rev Cardiol* 2011; 8: 30-41.
113. Zhang X, Yalcin S, Lee DF, Yeh TY, Lee SM, Su J, Mungamuri SK, Rimmelé P, Kennedy M, Sellers R, Landthaler M, Tuschl T, Chi NW, Lemischka I, Keller G, Ghaffari S. FOXO1 is an essential regulator of pluripotency in human embryonic stem cells. *Nat Cell Biol* 2011; 13: 1092-1099.
114. Chan SY, Rubin LJ. Metabolic dysfunction in pulmonary hypertension: from basic science to clinical practice. *Eur Respir Rev* 2017; 26: 170094.
115. Battiprolu PK, Hojayev B, Jiang N, Wang ZV, Luo X, Iglewski M, Shelton JM, Gerard RD, Rothermel BA, Gillette TG, Lavandero S, Hill JA. Metabolic stress-induced activation of FoxO1 triggers diabetic cardiomyopathy in mice. *J Clin Invest* 2012; 122: 1109-1118.
116. Qi Y, Zhu Q, Zhang K, Thomas C, Wu Y, Kumar R, Baker KM, Xu Z, Chen S, Guo S. Activation of Foxo1 by Insulin Resistance Promotes Cardiac Dysfunction and β–Myosin Heavy Chain Gene Expression. *Circulation: Heart Failure* 2015; 8: 198-208.
117. Schips TG, Wietelmann A, Höhn K, Schimanski S, Walther P, Braun T, Wirth T, Maier HJ. FoxO3 induces reversible cardiac atrophy and autophagy in a transgenic mouse model. *Cardiovascular Research* 2011; 91: 587-597.
118. Vahtola E, Louhelainen M, Forstén H, Merasto S, Raivio J, Kaheinen P, Kytö V, Tikkanen I, Levijoki J, Mervaala E. Sirtuin1-p53, forkhead box O3a, p38 and post-infarct cardiac remodeling in the spontaneously diabetic Goto-Kakizaki rat. *Cardiovascular Diabetology* 2010; 9: 5.
119. Lu D, Liu J, Jiao J, Long B, Li Q, Tan W, Li P. Transcription factor Foxo3a prevents apoptosis by regulating calcium through the apoptosis repressor with caspase recruitment domain. *J Biol Chem* 2013; 288: 8491-8504.
120. Förstermann U, Sessa WC. Nitric oxide synthases: regulation and function. *Eur Heart J* 2012; 33: 829-837, 837a-837d.
121. Awad H, Nolette N, Hinton M, Dakshinamurti S. AMPK and FoxO1 regulate catalase expression in hypoxic pulmonary arterial smooth muscle. *Pediatr Pulmonol* 2014; 49: 885-897.
122. Kudryashova TV, Dabral S, Nayakanti S, Ray A, Goncharov DA, Avolio T, Shen Y, Rode A, Pena A, Jiang L, Lin D, Baust J, Bachman TN, Graumann J, Ruppert C, Guenther A, Schmoranzer M, Grobs Y, Eve Lemay S, Tremblay E, Breuils-Bonnet S, Boucherat O, Mora AL, DeLisser H, Zhao J, Zhao Y, Bonnet S, Seeger W, Pullamsetti SS, Goncharova EA. Noncanonical HIPPO/MST Signaling via BUB3 and FOXO Drives Pulmonary Vascular Cell Growth and Survival. *Circ Res* 2022; 130: 760-778.
123. Rabinovitch M, Guignabert C, Humbert M, Nicolls MR. Inflammation and immunity in the pathogenesis of pulmonary arterial hypertension. *Circ Res* 2014; 115: 165-175.
124. Hedrick SM, Michelini RH, Doedens AL, Goldrath AW, Stone EL. FOXO transcription factors throughout T cell biology. *Nature Reviews Immunology* 2012; 12: 649-661.

125. Pusztai L, Gianni L. Technology insight: Emerging techniques to predict response to preoperative chemotherapy in breast cancer. *Nat Clin Pract Oncol* 2004; 1: 44-50.
126. Ni YG, Berenji K, Wang N, Oh M, Sachan N, Dey A, Cheng J, Lu G, Morris DJ, Castrillon DH, Gerard RD, Rothermel BA, Hill JA. Foxo transcription factors blunt cardiac hypertrophy by inhibiting calcineurin signaling. *Circulation* 2006; 114: 1159-1168.
127. Bonnet S, Rochefort G, Sutendra G, Archer SL, Haromy A, Webster L, Hashimoto K, Bonnet SN, Michelakis ED. The nuclear factor of activated T cells in pulmonary arterial hypertension can be therapeutically targeted. *Proceedings of the National Academy of Sciences* 2007; 104: 11418-11423.
128. Piao L, Fang YH, Parikh K, Ryan JJ, Toth PT, Archer SL. Cardiac glutaminolysis: a maladaptive cancer metabolism pathway in the right ventricle in pulmonary hypertension. *J Mol Med (Berl)* 2013; 91: 1185-1197.
129. Paulin R, Michelakis ED. Addressing Complexity in Pulmonary Hypertension: The FoxO1 Case. *Circ Res* 2015; 116: 1732-1735.
130. Paulin R, Michelakis ED. The metabolic theory of pulmonary arterial hypertension. *Circ Res* 2014; 115: 148-164.
131. Wu WH, Bonnet S, Shimauchi T, Toro V, Grobs Y, Romanet C, Bourgeois A, Vitry G, Omura J, Tremblay E, Nadeau V, Orcholski M, Breuils-Bonnet S, Martineau S, Ferraro P, Potus F, Paulin R, Provencher S, Boucherat O. Potential for inhibition of checkpoint kinases 1/2 in pulmonary fibrosis and secondary pulmonary hypertension. *Thorax* 2022; 77: 247-258.
132. Al-Tamari HM, Dabral S, Schmall A, Sarvari P, Ruppert C, Paik J, DePinho RA, Grimminger F, Eickelberg O, Guenther A, Seeger W, Savai R, Pullamsetti SS. FoxO3 an important player in fibrogenesis and therapeutic target for idiopathic pulmonary fibrosis. *EMBO Mol Med* 2018; 10: 276-293.
133. Tarnavski O, McMullen JR, Schinke M, Nie Q, Kong S, Izumo S. Mouse cardiac surgery: comprehensive techniques for the generation of mouse models of human diseases and their application for genomic studies. *Physiol Genomics* 2004; 16: 349-360.
134. Erratum: Synthesis of Novel Pinocembrin Amino Acid Derivatives and Their Antiaging Effect on Caenorhabditis elegans via the Modulating DAF-16/FOXO [Corrigendum]. *Drug Des Devel Ther* 2021; 15: 4257-4258.
135. Hiba B, Richard N, Janier M, Croisille P. Cardiac and respiratory double self-gated cine MRI in the mouse at 7 T. *Magn Reson Med* 2006; 55: 506-513.
136. Larson AC, White RD, Laub G, McVeigh ER, Li D, Simonetti OP. Self-gated cardiac cine MRI. *Magn Reson Med* 2004; 51: 93-102.
137. Luitel H, Sydykov A, Schymura Y, Mamazhakypov A, Janssen W, Pradhan K, Wietelmann A, Kosanovic D, Dahal BK, Weissmann N, Seeger W, Grimminger F, Ghofrani HA, Schermuly RT. Pressure overload leads to an increased accumulation and activity of mast cells in the right ventricle. *Physiol Rep* 2017; 5.
138. Engler AJ, Carag-Krieger C, Johnson CP, Raab M, Tang H-Y, Speicher DW, Sanger JW, Sanger JM, Discher DE. Embryonic cardiomyocytes beat best on a matrix with heart-like elasticity: scar-like rigidity inhibits beating. *Journal of Cell Science* 2008; 121: 3794-3802.
139. Sutendra G, Dromparis P, Paulin R, Zervopoulos S, Haromy A, Nagendran J, Michelakis ED. A metabolic remodeling in right ventricular hypertrophy is associated with decreased angiogenesis and a transition from a compensated to a decompensated state in pulmonary hypertension. *J Mol Med (Berl)* 2013; 91: 1315-1327.
140. Park S-H, Chung YM, Ma J, Yang Q, Berek JS, Hu MCT. Pharmacological activation of FOXO3 suppresses triple-negative breast cancer in vitro and in vivo. *Oncotarget* 2016; 7: 42110-42125.
141. Kang S, Hong J, Lee JM, Moon HE, Jeon B, Choi J, Yoon NA, Paek SH, Roh EJ, Lee CJ, Kang SS. Trifluoperazine, a Well-Known Antipsychotic, Inhibits Glioblastoma Invasion by Binding to Calmodulin and Disinhibiting Calcium Release Channel IP3R. *Mol Cancer Ther* 2017; 16: 217-227.

142. Huang C, Lan W, Fraunhoffer N, Meilerman A, Iovanna J, Santofimia-Castaño P. Dissecting the Anticancer Mechanism of Trifluoperazine on Pancreatic Ductal Adenocarcinoma. *Cancers (Basel)* 2019; 11.
143. Grobs Y, Awada C, Lemay SE, Romanet C, Bourgeois A, Toro V, Nadeau V, Shimauchi K, Orcholski M, Breuils-Bonnet S, Tremblay E, Provencher S, Paulin R, Boucherat O, Bonnet S. Preclinical Investigation of Trifluoperazine as a Novel Therapeutic Agent for the Treatment of Pulmonary Arterial Hypertension. *Int J Mol Sci* 2021; 22.
144. Benza RL, Miller DP, Gomberg-Maitland M, Frantz RP, Foreman AJ, Coffey CS, Frost A, Barst RJ, Badesch DB, Elliott CG, Liou TG, McGoon MD. Predicting survival in pulmonary arterial hypertension: Insights from the registry to evaluate early and long-term pulmonary arterial hypertension disease management (REVEAL). *Circulation* 2010; 122: 164-172.
145. Thenappan T, Shah SJ, Rich S, Tian L, Archer SL, Gomberg-Maitland M. Survival in pulmonary arterial hypertension: a reappraisal of the NIH risk stratification equation. *European Respiratory Journal* 2010; 35: 1079.
146. Humbert M, Sitbon O, Yaïci A, Montani D, Callaghan DS, Jaïs X, Parent F, Savale L, Natali D, Günther S, Chaouat A, Chabot F, Cordier JF, Habib G, Gressin V, Jing ZC, Souza R, Simonneau G. Survival in incident and prevalent cohorts of patients with pulmonary arterial hypertension. *European Respiratory Journal* 2010; 36: 549.
147. Mazurek JA, Vaidya A, Mathai SC, Roberts JD, Forfia PR. Follow-up tricuspid annular plane systolic excursion predicts survival in pulmonary arterial hypertension. *Pulmonary Circulation* 2017; 7: 361-371.
148. van de Veerdonk MC, Kind T, Marcus JT, Mauritz G-J, Heymans MW, Bogaard H-J, Boonstra A, Marques KMJ, Westerhof N, Vonk-Noordegraaf A. Progressive Right Ventricular Dysfunction in Patients With Pulmonary Arterial Hypertension Responding to Therapy. *Journal of the American College of Cardiology* 2011; 58: 2511-2519.
149. di Salvo TG, Yang KC, Brittain E, Absi T, Maltais S, Hemnes A. Right ventricular myocardial biomarkers in human heart failure. *J Card Fail* 2015; 21: 398-411.
150. Prisco SZ, Thenappan T, Prins KW. Treatment Targets for Right Ventricular Dysfunction in Pulmonary Arterial Hypertension. *JACC: Basic to Translational Science* 2020; 5: 1244-1260.
151. Fang CX, Dong F, Thomas DP, Ma H, He L, Ren J. Hypertrophic cardiomyopathy in high-fat diet-induced obesity: role of suppression of forkhead transcription factor and atrophy gene transcription. *Am J Physiol Heart Circ Physiol* 2008; 295: H1206-H1215.
152. Nakamura M, Sadoshima J. Mechanisms of physiological and pathological cardiac hypertrophy. *Nat Rev Cardiol* 2018; 15: 387-407.
153. Liu Y, Chen X, Zhang H-G. Editorial: Cardiac Hypertrophy: From Compensation to Decompensation and Pharmacological Interventions. *Frontiers in Pharmacology* 2021; 12.
154. Heger J, Schulz R, Euler G. Molecular switches under TGFβ signalling during progression from cardiac hypertrophy to heart failure. *Br J Pharmacol* 2016; 173: 3-14.
155. He J, Luo Y, Song J, Tan T, Zhu H. Non-coding RNAs and Pathological Cardiac Hypertrophy. *Adv Exp Med Biol* 2020; 1229: 231-245.
156. Wang J, Liew OW, Richards AM, Chen Y-T. Overview of MicroRNAs in Cardiac Hypertrophy, Fibrosis, and Apoptosis. *International journal of molecular sciences* 2016; 17: 749.
157. Mushtaq I, Ishtiaq A, Ali T, Jan MI, Murtaza I. An Overview of Non-coding RNAs and Cardiovascular System. In: Xiao J, editor. Non-coding RNAs in Cardiovascular Diseases. Singapore: Springer Singapore; 2020. p. 3-45.
158. Zehendner CM, Valasarajan C, Werner A, Boeckel JN, Bischoff FC, John D, Weirick T, Glaser SF, Rossbach O, Jaé N, Demolli S, Khassafi F, Yuan K, de Jesus Perez VA, Michalik KM, Chen W, Seeger W, Guenther A, Wasnick RM, Uchida S, Zeiher AM, Dimmeler S, Pullamsetti SS. Long Noncoding RNA TYKRIL Plays a Role in Pulmonary Hypertension via the p53-mediated Regulation of PDGFRβ. *Am J Respir Crit Care Med* 2020; 202: 1445-1457.

159. Shimamoto S, Nakashima K, Nishikoba N, Kohrogi R, Ohtsuka A, Fujimura S, Ijiri D. Suppression of FoxO1 mRNA by beta2 -adrenoceptor-cAMP signaling through miR-374b-5p and miR-7a-1-3p in C2C12 myotubes. *FEBS Open Bio* 2022; 12: 627-637.
160. Galley JC, Hahn SA, Miller MP, Durgin BG, Jackson EK, Stocker SD, Straub AC. Angiotensin II augments renal vascular smooth muscle soluble GC expression via an AT1 receptor-forkhead box subclass O transcription factor signalling axis. *Br J Pharmacol* 2022; 179: 2490-2504.
161. Brown AK, Webb AE. Regulation of FOXO Factors in Mammalian Cells. *Current topics in developmental biology* 2018; 127: 165-192.
162. Philip-Couderc P, Tavares NI, Roatti A, Lerch R, Montessuit C, Baertschi AJ. Forkhead Transcription Factors Coordinate Expression of Myocardial KATP Channel Subunits and Energy Metabolism. *Circulation Research* 2008; 102: e20-e35.
163. Shimizu H, Langenbacher AD, Huang J, Wang K, Otto G, Geisler R, Wang Y, Chen J-N. The Calcineurin-FoxO-MuRF1 signaling pathway regulates myofibril integrity in cardiomyocytes. *eLife* 2017; 6: e27955.
164. van der Vos KE, Coffer PJ. The extending network of FOXO transcriptional target genes. *Antioxid Redox Signal* 2011; 14: 579-592.
165. Hinz B. Formation and function of the myofibroblast during tissue repair. *J Invest Dermatol* 2007; 127: 526-537.
166. Tomasek JJ, Gabbiani G, Hinz B, Chaponnier C, Brown RA. Myofibroblasts and mechano-regulation of connective tissue remodelling. *Nat Rev Mol Cell Biol* 2002; 3: 349-363.
167. van Putten S, Shafieyan Y, Hinz B. Mechanical control of cardiac myofibroblasts. *J Mol Cell Cardiol* 2016; 93: 133-142.
168. Herum KM, Choppe J, Kumar A, Engler AJ, McCulloch AD. Mechanical regulation of cardiac fibroblast profibrotic phenotypes. *Molecular biology of the cell* 2017; 28: 1871-1882.
169. Georges PC, Janmey PA. Cell type-specific response to growth on soft materials. *J Appl Physiol (1985)* 2005; 98: 1547-1553.
170. Discher DE, Janmey P, Wang YL. Tissue cells feel and respond to the stiffness of their substrate. *Science* 2005; 310: 1139-1143.
171. Solon J, Levental I, Sengupta K, Georges PC, Janmey PA. Fibroblast adaptation and stiffness matching to soft elastic substrates. *Biophys J* 2007; 93: 4453-4461.
172. Byun J, Del Re DP, Zhai P, Ikeda S, Shirakabe A, Mizushima W, Miyamoto S, Brown JH, Sadoshima J. Yes-associated protein (YAP) mediates adaptive cardiac hypertrophy in response to pressure overload. *Journal of Biological Chemistry* 2019; 294: 3603-3617.
173. Liu F, Lagares D, Choi KM, Stopfer L, Marinković A, Vrbanac V, Probst CK, Hiemer SE, Sisson TH, Horowitz JC, Rosas IO, Fredenburgh LE, Feghali-Bostwick C, Varelas X, Tager AM, Tschumperlin DJ. Mechanosignaling through YAP and TAZ drives fibroblast activation and fibrosis. *American Journal of Physiology-Lung Cellular and Molecular Physiology* 2015; 308: L344-L357.
174. Shao D, Zhai P, Del Re DP, Sciarretta S, Yabuta N, Nojima H, Lim D-S, Pan D, Sadoshima J. A functional interaction between Hippo-YAP signalling and FoxO1 mediates the oxidative stress response. *Nature Communications* 2014; 5: 3315.
175. Shih YR, Tseng KF, Lai HY, Lin CH, Lee OK. Matrix stiffness regulation of integrin-mediated mechanotransduction during osteogenic differentiation of human mesenchymal stem cells. *J Bone Miner Res* 2011; 26: 730-738.
176. Nho RS, Kahm J. β1-Integrin-Collagen Interaction Suppresses FoxO3a by the Coordination of Akt and PP2A*. *Journal of Biological Chemistry* 2010; 285: 14195-14209.
177. Liu Y, Beyer A, Aebersold R. On the Dependency of Cellular Protein Levels on mRNA Abundance. *Cell* 2016; 165: 535-550.
178. Cheng Z, Teo G, Krueger S, Rock TM, Koh HW, Choi H, Vogel C. Differential dynamics of the mammalian mRNA and protein expression response to misfolding stress. *Mol Syst Biol* 2016; 12: 855.

179. Buccitelli C, Selbach M. mRNAs, proteins and the emerging principles of gene expression control. *Nat Rev Genet* 2020; 21: 630-644.
180. Mamazhakypov A, Sartmyrzaeva M, Kushubakova N, Duishobaev M, Maripov A, Sydykov A, Sarybaev A. Right Ventricular Response to Acute Hypoxia Exposure: A Systematic Review. *Front Physiol* 2021; 12: 786954.
181. Smith KA, Waypa GB, Dudley VJ, Budinger GRS, Abdala-Valencia H, Bartom E, Schumacker PT. Role of Hypoxia-Inducible Factors in Regulating Right Ventricular Function and Remodeling during Chronic Hypoxia-induced Pulmonary Hypertension. *American journal of respiratory cell and molecular biology* 2020; 63: 652-664.
182. Smith KA, Waypa GB, Dudley VJ, Budinger GRS, Abdala-Valencia H, Bartom E, Schumacker PT. Role of Hypoxia-Inducible Factors in Regulating Right Ventricular Function and Remodeling during Chronic Hypoxia-induced Pulmonary Hypertension. *Am J Respir Cell Mol Biol* 2020; 63: 652-664.
183. Zhang B, Niu W, Dong H-Y, Liu M-L, Luo Y, Li Z-C. Hypoxia induces endothelial-mesenchymal transition in pulmonary vascular remodeling. *International journal of molecular medicine* 2018; 42: 270-278.
184. Hapke RY, Haake SM. Hypoxia-induced epithelial to mesenchymal transition in cancer. *Cancer Letters* 2020; 487: 10-20.
185. Bakker WJ, Harris IS, Mak TW. FOXO3a Is Activated in Response to Hypoxic Stress and Inhibits HIF1-Induced Apoptosis via Regulation of CITED2. *Molecular Cell* 2007; 28: 941-953.
186. Jensen KS, Binderup T, Jensen KT, Therkelsen I, Borup R, Nilsson E, Multhaupt H, Bouchard C, Quistorff B, Kjaer A, Landberg G, Staller P. FoxO3A promotes metabolic adaptation to hypoxia by antagonizing Myc function. *The EMBO journal* 2011; 30: 4554-4570.
187. Panne D, Maniatis T, Harrison SC. An atomic model of the interferon-beta enhanceosome. *Cell* 2007; 129: 1111-1123.
188. Liu SY, Sanchez DJ, Cheng G. New developments in the induction and antiviral effectors of type I interferon. *Curr Opin Immunol* 2011; 23: 57-64.
189. Tamura T, Yanai H, Savitsky D, Taniguchi T. The IRF family transcription factors in immunity and oncogenesis. *Annu Rev Immunol* 2008; 26: 535-584.
190. Yusuf I, Kharas MG, Chen J, Peralta RQ, Maruniak A, Sareen P, Yang VW, Kaestner KH, Fruman DA. KLF4 is a FOXO target gene that suppresses B cell proliferation. *International Immunology* 2008; 20: 671-681.
191. Zhang H, Zhu X, Chen J, Jiang Y, Zhang Q, Kong C, Xing J, Ding L, Diao Z, Zhen X, Sun H, Yan G. Krüppel-like factor 12 is a novel negative regulator of forkhead box O1 expression: a potential role in impaired decidualization. *Reproductive Biology and Endocrinology* 2015; 13: 80.
192. Wu X, Fan Z, Chen M, Chen Y, Rong D, Cui Z, Yuan Y, Zhuo L, Xu Y. Forkhead transcription factor FOXO3a mediates interferon-γ-induced MHC II transcription in macrophages. *Immunology* 2019; 158: 304-313.
193. Hwang I, Uchida H, Dai Z, Li F, Sanchez T, Locasale JW, Cantley LC, Zheng H, Paik J. Cellular stress signaling activates type-I IFN response through FOXO3-regulated lamin posttranslational modification. *Nature Communications* 2021; 12: 640.
194. Liu X, Cai X, Zhang D, Xu C, Xiao W. Zebrafish foxo3b Negatively Regulates Antiviral Response through Suppressing the Transactivity of irf3 and irf7. *J Immunol* 2016; 197: 4736-4749.
195. Bowers SLK, Meng Q, Molkentin JD. Fibroblasts orchestrate cellular crosstalk in the heart through the ECM. *Nature Cardiovascular Research* 2022; 1: 312-321.
196. Prabhu SD, Frangogiannis NG. The Biological Basis for Cardiac Repair After Myocardial Infarction: From Inflammation to Fibrosis. *Circ Res* 2016; 119: 91-112.
197. Zhang Y, Wang X, Zhang X, Wang J, Ma Y, Zhang L, Cao X. RNA-binding protein YTHDF3 suppresses interferon-dependent antiviral responses by promoting FOXO3 translation. *Proc Natl Acad Sci U S A* 2019; 116: 976-981.

198. van Grevenynghe J, Cubas RA, DaFonseca S, Metcalf T, Tremblay CL, Trautmann L, Sekaly RP, Schatzle J, Haddad EK. Foxo3a: an integrator of immune dysfunction during HIV infection. *Cytokine Growth Factor Rev* 2012; 23: 215-221.
199. Seiler F, Hellberg J, Lepper PM, Kamyschnikow A, Herr C, Bischoff M, Langer F, Schafers HJ, Lammert F, Menger MD, Bals R, Beisswenger C. FOXO transcription factors regulate innate immune mechanisms in respiratory epithelial cells. *J Immunol* 2013; 190: 1603-1613.
200. Loebel M, Holzhauser L, Hartwig JA, Shukla PC, Savvatis K, Jenke A, Gast M, Escher F, Becker SC, Bauer S, Stroux A, Beling A, Kespohl M, Pinkert S, Fechner H, Kuehl U, Lassner D, Poller W, Schultheiss HP, Zeller T, Blankenberg S, Papageorgiou AP, Heymans S, Landmesser U, Scheibenbogen C, Skurk C. The forkhead transcription factor Foxo3 negatively regulates natural killer cell function and viral clearance in myocarditis. *Eur Heart J* 2018; 39: 876-887.
201. Gimenes-Junior J, Owuar N, Vari HR, Li W, Xander N, Kotnala S, Sajjan US. FOXO3a regulates rhinovirus-induced innate immune responses in airway epithelial cells. *Sci Rep* 2019; 9: 18180.
202. Thomas TP, Grisanti LA. The Dynamic Interplay Between Cardiac Inflammation and Fibrosis. *Frontiers in physiology* 2020; 11: 529075-529075.
203. Qu H, Zhang Y, Zhang W, Zhu Y, Xu R. Knockout of Cardiac Troponin I-Interacting Kinase leads to cardiac dysfunction and remodeling. *Clin Exp Pharmacol Physiol* 2022.
204. Canty JM, Jr. Myocardial injury, troponin release, and cardiomyocyte death in brief ischemia, failure, and ventricular remodeling. *Am J Physiol Heart Circ Physiol* 2022; 323: H1-H15.
205. Hoffman M, Palioura D, Kyriazis ID, Cimini M, Badolia R, Rajan S, Gao E, Nikolaidis N, Schulze PC, Goldberg IJ, Kishore R, Yang VW, Bannister TD, Bialkowska AB, Selzman CH, Drakos SG, Drosatos K. Cardiomyocyte Kruppel-Like Factor 5 Promotes De Novo Ceramide Biosynthesis and Contributes to Eccentric Remodeling in Ischemic Cardiomyopathy. *Circulation* 2021; 143: 1139-1156.
206. Zhao H, Yang H, Geng C, Chen Y, Pang J, Shu T, Zhao M, Tang Y, Li Z, Li B, Hou C, Song X, Wu A, Guo X, Chen S, Liu B, Yan C, Wang J. Role of IgE-FcepsilonR1 in Pathological Cardiac Remodeling and Dysfunction. *Circulation* 2021; 143: 1014-1030.
207. Vigil-Garcia M, Demkes CJ, Eding JEC, Versteeg D, de Ruiter H, Perini I, Kooijman L, Gladka MM, Asselbergs FW, Vink A, Harakalova M, Bossu A, van Veen TAB, Boogerd CJ, van Rooij E. Gene expression profiling of hypertrophic cardiomyocytes identifies new players in pathological remodelling. *Cardiovasc Res* 2021; 117: 1532-1545.
208. Ye L, Wang S, Xiao Y, Jiang C, Huang Y, Chen H, Zhang H, Zhang H, Liu J, Xu Z, Hong H. Pressure Overload Greatly Promotes Neonatal Right Ventricular Cardiomyocyte Proliferation: A New Model for the Study of Heart Regeneration. *J Am Heart Assoc* 2020; 9: e015574.
209. El Azzouzi H, Vilaca AP, Feyen DAM, Gommans WM, de Weger RA, Doevendans PAF, Sluijter JPG. Cardiomyocyte Specific Deletion of ADAR1 Causes Severe Cardiac Dysfunction and Increased Lethality. *Front Cardiovasc Med* 2020; 7: 30.
210. Graham HK, Horn M, Trafford AW. Extracellular matrix profiles in the progression to heart failure. *Acta Physiologica* 2008; 194: 3-21.
211. Maron BJ, Wolfson JK, Epstein SE, Roberts WC. Intramural ("small vessel") coronary artery disease in hypertrophic cardiomyopathy. *Journal of the American College of Cardiology* 1986; 8: 545-557.
212. Schwartzkopff B, Mundhenke M, Strauer BE. Alterations of the Architecture of Subendocardial Arterioles in Patients With Hypertrophic Cardiomyopathy and Impaired Coronary Vasodilator Reserve: A Possible Cause for Myocardial Ischemia 11This study was supported by Grant SFB 242: Koronare Herzkrankheit: Prävention und Therapie akuter Komplikationen from the Deutsche Forschungsgemeinschaft, Bonn, Germany. *Journal of the American College of Cardiology* 1998; 31: 1089-1096.
213. Paik JH. FOXOs in the maintenance of vascular homoeostasis. *Biochem Soc Trans* 2006; 34: 731-734.

214. Potente M, Urbich C, Sasaki K, Hofmann WK, Heeschen C, Aicher A, Kollipara R, DePinho RA, Zeiher AM, Dimmeler S. Involvement of Foxo transcription factors in angiogenesis and postnatal neovascularization. *J Clin Invest* 2005; 115: 2382-2392.
215. Furuyama T, Kitayama K, Shimoda Y, Ogawa M, Sone K, Yoshida-Araki K, Hisatsune H, Nishikawa S, Nakayama K, Nakayama K, Ikeda K, Motoyama N, Mori N. Abnormal angiogenesis in Foxo1 (Fkhr)-deficient mice. *J Biol Chem* 2004; 279: 34741-34749.
216. Patel MN, Halling-Brown MD, Tym JE, Workman P, Al-Lazikani B. Objective assessment of cancer genes for drug discovery. *Nat Rev Drug Discov* 2013; 12: 35-50.
217. Gomes AR, Zhao F, Lam EW. Role and regulation of the forkhead transcription factors FOXO3a and FOXM1 in carcinogenesis and drug resistance. *Chin J Cancer* 2013; 32: 365-370.
218. Benayoun BA, Caburet S, Veitia RA. Forkhead transcription factors: key players in health and disease. *Trends Genet* 2011; 27: 224-232.
219. Myatt SS, Lam EW. The emerging roles of forkhead box (Fox) proteins in cancer. *Nat Rev Cancer* 2007; 7: 847-859.
220. Feng W, Wang J, Yan X, Zhai C, Shi W, Wang Q, Zhang Q, Li M. Paclitaxel alleviates monocrotaline-induced pulmonary arterial hypertension via inhibition of FoxO1-mediated autophagy. *Naunyn Schmiedebergs Arch Pharmacol* 2019; 392: 605-613.
221. Sunters A, Madureira PA, Pomeranz KM, Aubert M, Brosens JJ, Cook SJ, Burgering BM, Coombes RC, Lam EW. Paclitaxel-induced nuclear translocation of FOXO3a in breast cancer cells is mediated by c-Jun NH2-terminal kinase and Akt. *Cancer Res* 2006; 66: 212-220.
222. Chung YM, Khan PP, Wang H, Tsai WB, Qiao Y, Yu B, Larrick JW, Hu MC. Sensitizing tumors to anti-PD-1 therapy by promoting NK and CD8+ T cells via pharmacological activation of FOXO3. *J Immunother Cancer* 2021; 9.
223. Otani H, Engelman RM, Rousou JA, Breyer RH, Clement R, Prasad R, Klar J, Das DK. Improvement of myocardial function by trifluoperazine, a calmodulin antagonist, after acute coronary artery occlusion and coronary revascularization. *J Thorac Cardiovasc Surg* 1989; 97: 267-274.
224. Gomez-Arroyo JG, Farkas L, Alhussaini AA, Farkas D, Kraskauskas D, Voelkel NF, Bogaard HJ. The monocrotaline model of pulmonary hypertension in perspective. *Am J Physiol Lung Cell Mol Physiol* 2012; 302: L363-369.
225. Ciuclan L, Bonneau O, Hussey M, Duggan N, Holmes AM, Good R, Stringer R, Jones P, Morrell NW, Jarai G, Walker C, Westwick J, Thomas M. A novel murine model of severe pulmonary arterial hypertension. *Am J Respir Crit Care Med* 2011; 184: 1171-1182.
226. Vanderpool RR, Puri R, Osorio A, Wickstrom K, Desai AA, Black SM, Garcia JGN, Yuan JX-J, Rischard FP. Surfing the right ventricular pressure waveform: methods to assess global, systolic and diastolic RV function from a clinical right heart catheterization. *Pulmonary Circulation* 2020; 10: 2045894019850993.
227. Lee D, Goldberg AL. SIRT1 protein, by blocking the activities of transcription factors FoxO1 and FoxO3, inhibits muscle atrophy and promotes muscle growth. *J Biol Chem* 2013; 288: 30515-30526.

ERKLÄRUNG ZUR DISSERTATION

“Hiermit erkläre ich, dass ich die vorliegende Arbeit selbständig und ohne unzulässige Hilfe oder Benutzung anderer als der angegebenen Hilfsmittel angefertigt habe. Alle Textstellen, die wörtlich oder sinngemäß aus veröffentlichten oder nichtveröffentlichten Schriften entnommen sind, und alle Angaben, die auf mündlichen Auskünften beruhen, sind als solche kenntlich gemacht. Bei den von mir durchgeführten und in der Dissertation erwähnten Untersuchungen habe ich die Grundsätze guter wissenschaftlicher Praxis, wie sie in der „Satzung der Justus-Liebig-Universität Gießen zur Sicherung guter wissenschaftlicher Praxis“ niedergelegt sind, eingehalten sowie ethische, datenschutzrechtliche und tierschutzrechtliche Grundsätze befolgt. Ich versichere, dass Dritte von mir weder unmittelbar noch mittelbar geldwerte Leistungen für Arbeiten erhalten haben, die im Zusammenhang mit dem Inhalt der vorgelegten Dissertation stehen, und dass die vorgelegte Arbeit weder im Inland noch im Ausland in gleicher oder ähnlicher Form einer anderen Prüfungsbehörde zum Zweck einer Promotion oder eines anderen Prüfungsverfahrens vorgelegt wurde. Alles aus anderen Quellen und von anderen Personen übernommene Material, das in der Arbeit verwendet wurde oder auf das direkt Bezug genommen wird, wurde als solches kenntlich gemacht. Insbesondere wurden alle Personen genannt, die direkt und indirekt an der Entstehung der vorliegenden Arbeit beteiligt waren. Mit der Überprüfung meiner Arbeit durch eine Plagiatserkennungssoftware bzw. ein internetbasiertes Softwareprogramm erkläre ich mich einverstanden.“

_____ _____

Ort/Datum Unterschrift

ACKNOWLEDGEMENTS

Above all, I express my sincere gratitude to my supervisor **Prof. Dr. Soni Savai Pullamsetti,** for the opportunity to work in her lab and conduct my doctoral work under her guidance. I would like to thank her for her constructive ideas, discussions, and support throughout the doctoral program. I am thankful to her for providing me with the opportunities to present my research work at various international conferences, thus enhancing my confidence and soft skills.

I would like to thank **Prof. Dr. Werner Seeger** for allowing me to pursue my Ph.D. at Max Planck Institute for Heart and Lung Research and for creating a great platform and thought-provoking scientific discussions.

I would like to express my thanks to **Prof. Dr. Rajkumar Savai** for providing all the scientific and moral support throughout my thesis

I would like to specially thank **Prof. Dr. Sebastien Bonnet** for sharing human RV tissue samples and performing in vivo experiments in the rat.

I would like to thank **Dr. Argen Mamazhakypov** for performing PAB surgery on mice and **Dr. Baktybek Kojonazarov** for Echo analysis.
I sincerely thank **Dr. Astrid Wietelmann** and **Ursula Hofmann** for helping with the MRI image acquisition.
I would like to thank **Dr. Stefan Guenther** for his excellent support with RNA sequencing experiment in processing the samples and analyzing the data.
Thanks to **Dr. Giovanni Maroli** for helping me with analyzing the RNA sequencing data as well as sharing his valuable inputs to the project.

I would like to thank **Uta Eule** for performing hemodynamic measurements, **Natascha Wilker** and **Jana Rostkovius** for organ isolation and other technical assistance.

Special thanks to **Dr. Swati Dabral** for teaching me various techniques during my initial days in the lab. I thank **Dr. Prakash Chelladurai** and **Dr. Chanil Valasarajan** for creating memorable moments during my years of work. I would also like to thank all my other wonderful colleagues for offering experimental tips, for the friendly working atmosphere they created and all those enjoyable moments outside of work.

Finally, I am forever grateful to my **Father, Mother** and **brother** for their unconditional love and support, without which none of this would have been possible. I sincerely and wholeheartedly thank my wife **Krishna Priya** for her endless love, patience, moral support and assistance in every possible way and for being my pillar and confidant throughout the years.